Functional 1D mesochannels for Electrochemical Sensors

Himanshu Maheshwari

UNIVERSITÉ DE LORRAINE

DOCTORAL THESIS

BY

HIMANSHU MAHESHWARI

Functional 1D mesochannels for Electrochemical Sensors

Supervisor:

Dr. Grégoire HERZOG — Researcher - CNRS

Reviewers:

Dr. Elisabeth LOJOU — Research Director - CNRS

Dr. James ROHAN — Research Group leader - Tyndall National Institute

Examiners:

Dr. Elise ROTUREAU — Researcher - CNRS

Invited:

Dr. Neus VILÀ — Lecturer - University of Lorraine

Dr. Nicolas STEIN — Lecturer - University of Lorraine

A thesis submitted in fulfillment of the requirements for the degree of Doctor of Chemistry

Doctoral School C2MP

Laboratoire de Chimie Physique et Microbiologie pour les Matériaux et l'Environnement (LCPME)

Unité Mixte de Recherche CNRS/Université de Lorraine UMR 7564

December 17, 2020

UNIVERSITÉ DE LORRAINE

THÈSE DOCTORALE

PAR

HIMANSHU MAHESHWARI

Mésocanaux 1D fonctionnels pour les capteurs électrochimiques

Directeur:

Dr. Grégoire HERZOG — Chargé de Recherche - CNRS

Rapporteurs:

Dr. Elisabeth LOJOU — Directrice de recherche - CNRS

Dr. James ROHAN — Research Group leader - Tyndall National Institute

Examinateurs:

Dr. Elise ROTUREAU — Chargée de Recherche - CNRS

Invités:

Dr. Neus VILÀ — Maître de Conférences - Université de Lorraine

Dr. Nicolas STEIN — Maitre de conférences - Université de Lorraine

Une thèse soumise pour obtenir le diplôme de
Doctorat en Chimie

Ecole Doctorale C2MP

Laboratoire de Chimie Physique et Microbiologie pour les Matériaux et l'Environnement (LCPME)
Unité Mixte de Recherche CNRS/Université de Lorraine UMR 7564

December 17, 2020

UNIVERSITÉ DE LORRAINE

Abstract

Laboratoire de Chimie Physique et Microbiologie pour les Matériaux et l'Environnement (LCPME)

Doctor of Chemistry

Functional 1D mesochannels for Electrochemical Sensors

by Himanshu MAHESHWARI

In this thesis, we discuss vertically oriented mesoporous silica and their characteristic properties, synthesis procedures and applications. It is of particular interest as it provides direct access to underlying substrate through the pores and is suitable for a variety of applications such as molecular sieving, electrode protection, enhanced detection of cations through electrochemistry and electrochemiluminescence, deposition of isolated metallic and polymeric nanowires, DNA biosensor, etc.

We then discuss the electrochemically mediated oxidation of natural aminothiols (cysteine, glutathione and homocysteine) by a ferrocene derivative following an EC' mechanism and the rate kinetics at a bare indium-tin oxide (ITO) electrode.

Further, mesoporous silica thin films exhibiting vertical nanochannels were grown by electrochemically assisted self-assembly method onto ITO electrode. When using the silica film deposited electrodes and ferrocenedimethanol ($\mathrm{Fc(MeOH)_2}$) as mediator in solution, both cysteine and glutathione can be oxidized by $\mathrm{Fc(MeOH)_2^+}$ generated at the electrode surface, following an EC' mechanism. Electron transfer rates were three times faster with cysteine than glutathione, suggesting that selectivity for cysteine could be achieved using mesoporous films. This was exploited for the reagent-free selective detection of cysteine over glutathione by using a ferrocene-functionalized mesoporous silica film on ITO electrode, based on a combination of charge transfer kinetic and mass transport limitations through the oriented nanochannels. This has been demonstrated by cyclic voltammetry and amperometry in a flow injection analysis mode. Experimentally, the lowest concentration of cysteine detected was 3 µM in flow injection analysis mode.

Further, microelectrodes made of ITO and carbon were fabricated and modified with mesoporous silica. Carbon microelectrodes were further functionalized with ferrocene and characterized electrochemically.

Overall, silica modified electrodes show a good potential in electroanalytical applications for a variety of reagents through their size and charge selective properties.

UNIVERSITÉ DE LORRAINE

Résumé

Laboratoire de Chimie Physique et Microbiologie pour les Matériaux et l'Environnement (LCPME)

Doctorant en Chimie

Mésocanaux 1D fonctionnels pour les capteurs électrochimiques

par Himanshu MAHESHWARI

Dans cette thèse, nous discutons de silice à mésoporosité verticale et ses méthodes de synthèses, ses propriétés caractéristiques et ses applications potentielles. Il s'agit d'un matériau particulièrement intéressant car il offre un accès direct au substrat sur lequel il est déposé au travers de mésopores et offre une grande variété d'applications telles que : la filtration à l'échelle moléculaire, la protection des surfaces d'électrodes, la détection améliorée de cations par électrochimie et électrochimiluminescence, le dépôt de nanofils isolés métalliques ou polymériques, les biocapteurs ADN, etc.

Nous discutons ensuite de l'oxydation à médiation électrochimique des aminothiols naturels (cystéine, glutathion et homocystéine) par un dérivé du ferrocène selon un mécanisme EC', et de la cinétique du transfert d'électron sur une électrode nue d'oxyde d'étain dopé à l'indium (ITO).

Ensuite, des films minces de silice mésoporeuse présentant des nanocanaux verticaux ont été déposés par une méthode d'auto-assemblage assistée électrochimiquement sur une électrode d'ITO. En utilisant les électrodes déposées sur le film de silice et le ferrocenediméthanol ($\mathrm{Fc(MeOH)_2}$) comme médiateur en solution, il est possible d'oxyder les deux, la cystéine et le glutathion, par $\mathrm{Fc(MeOH)_2^+}$ générés à la surface de l'électrode, par un mécanisme EC'. Les vitesses de transfert d'électrons étaient trois fois plus rapides avec la cystéine qu'avec le glutathion. Ce phénomène a été exploité pour la méthode de détection sélective et sans réactif de la cystéine par rapport au glutathion en utilisant un film de silice mésoporeuse fonctionnalisé avec du ferrocène sur une électrode d'ITO, grâce à une combinaison des limitations de la cinétique de transfert de charge et du transport de masse à l'intérieur des nanocanaux orientés. Ceci a été démontré par des méthodes de

voltampérométrie cyclique et d'ampérométrie dans un mode d'analyse par injection en flux. Expérimentalement, la plus basse concentration de cystéine détectée était de 3 µM en mode d'analyse par injection en flux.

De plus, des microélectrodes d'ITO et de carbone ont été fabriquées et déposées avec de la silice mésoporeuse. Les microélectrodes de carbone ont été fonctionnalisées avec du ferrocène et caractérisées électrochimiquement.

Les électrodes modifiées à la silice présentent un bon potentiel dans les applications électroanalytiques pour une variété de réactifs par leur taille et leurs propriétés sélectives de charge.

Dedicated to the three most prominent figures of my life. Their boundless faith and love for me, made me the person I am. All that I am, or hope to be, I owe to them.

Late Sh. Anand Prakash MAHESHWARI (grandfather)
Late Mr. Rajiv MAHESHWARI (father)
Mrs. Meena MAHESHWARI (mother)

Acknowledgements

First and foremost, I would like to thank Dr. Grégoire HERZOG & Dr. Neus VILÀ for accepting me as their doctoral student. In a true sense, this thesis wouldn't be possible without their continuous support, patience, guidance, knowledge and immense experience. Dr. Grégoire HERZOG has not only guided me patiently at all the times regarding experimental and theoretical aspects fo the work, but has always been present since my first day in France for any professional and personal help. I can never thank him enough. Dr. Neus VILÀ has guided me through her immense knowledge & experience, while also pushed me to bring out my best efforts. Both of them have shown me how a true researcher looks like.

I would also like to specially thank Dr. Alain WALCARIUS for accepting me in his group and for his suggestions and critical opinions over the years that helped me bring this work to completion. My sincere thanks to Dr. Liang LIU for the many friendly advices, and for his help with microelectrode fabrications. I also thank Dr. Mathieu ETIENNE, Dr. Christelle DESPAS, Dr. Marc HEBRANT, Dr. Manuel DASSOT and the other permanent group member for their suggestions and the numerous fruitful discussions. I specially thank the cheerful M. Gerard PAQUOT for helping me with the various cell designs he made over the years and keeping the lab atmosphere light. Along with that, I also thank M. Jean-Paul MOULIN, Mme. Claire GENOIS, Mme. Marie TERCIER, Mme. Christelle CHARBAUT & M. Patrich BOMBBARDIER for their help with the non-academic tasks in the lab. It had been a real pleasure to work with the brilliant people at LCPME.

My Colleagues and friends in the lab had been a great source of fun, encouragement and support during this thesis. I would like to specially thank Joanna, Taisiia, Jianren, Wahid, Ning, Deomila, Guofeng, Qiao, Mariela, Magdalena, Laura, Christelle, Vincent, Samantha, Tauqir, Samuel, José and Bachira among many others. I cannot forget the interesting talks, the coffee and lunch breaks, and the parties we had.

I would like to thank the jury members, Dr. James ROHAN, Dr. Elisabeth LOJOU, Dr. Elise ROTUREAU and Dr. Nicolas STEIN for taking out their valuable time to go through my thesis. It had been a real pleasure to defend my thesis in front of these reputed researchers. I would also like to thank the members of my thesis monitoring committeem Dr. Pierre GROS and Dr. Thomas DONEUX for their time and helpful suggestions.

I would like to mention the most important people in my life, my mother, Mrs. Meena MAHESHWARI, my sister, Priyanka and my brother, Mayank, who have been at my support through all life's ups and downs. I would also like to remember my late father, Mr. Rajiv MAHESHWARI and my late grandparents for making me the person I am today. I would also thank my extended family and all my cousins for their continued support. I cannot thank enough Mme. Neelam ROUT, who has supported, pushed me, kept me organized and been by my side throughout this journey. M. Ishtiaq Ahmad for being my brother and the good-hearted genuine person.

A big thanks also goes to my friends for keeping me sane during this time. First and foremost, my oldest friends, Shiv, Deepak and Nitish for being the most awesome friends. Aakriti, Anupam, Rajhans, Shubhangi, Neeraj, Vaibhav, and my other Amity friends that always remind me of the crazy and the fun time at the University. I thank my amazing first french friend, Stéphanie Noël, with whom hours of conversations on vitually any topics are possible for me. My small group of close friends in France, viz. Anantrao, Sayali, Divyesh, Surbhi, Rituraj and Ashmita who have been at my side for all the travels, parties and the most fun moments here. I would love to thank Mamie Colette Guillemain, Françoise, Laura, Abd-el-halim, Dominique, Jaithra, Mani and Srikar for the familial love and care. I also thank Sunit, Anupama, Tulika, Slava, Mehran, Mainak and Shantanu, among many others who affected my life throughout this journey. Without these friends, the last 3 years wouldn't have been so eventful and memorable.

I would also thank all my past teachers and all the well wishers, who have influenced my life and taught me about it. And above all God, who directs our lives.

Finally, I would like to thank French PIA project "Lorraine Université d'Excellence" (Reference N° ANR-15-IDEX-04-LUE) for supporting this work.

"Science knows no country, because knowledge belongs to humanity, and is the torch which illuminates the world. Science is the highest personification of the nation because that nation will remain the first which carries the furthest the works of thought and intelligence."

Louis Pasteur

"Get up and work. And STOP wasting time."

Rajeev Maheshwari, my father

Contents

List of Figures

List of Tables

List of Abbreviations

APTES	3-**a**mino**p**ropyl**trie**thoxy**s**ilane
AzPTES	3-**az**ido**p**ropyl**trie**thoxy**s**ilane
Bis-tris	2,2-**Bis**(hydroxyethyl)-(imino**tris**)- (hydroxymethyl)-methane
CCD	**C**harge-**c**oupled **d**evice
CE	**C**ounter **E**lectrode
CMOS	**C**omplementary **m**etal–**o**xide–**s**emiconductor
COF	**C**ovalent **O**rganic **F**ramework
CV	**C**yclic **V**oltammetry
DCE	**D**i**c**hloro**e**thane
DNA	**D**eoxyribo**n**ucleic **a**cid
EASA	**E**lectrochemically **A**ssisted **S**elf-**A**ssembly
EC′	**E**lectrochemical **C**atalytic regeneration of electroactive species in a following homogenous reaction
EIS	**E**lectrochemical **I**mpedance **S**pectroscopy
EISA	**E**vaporation **I**nduced **S**elf-**A**ssembly
EtOH	**Et**han**ol**
FCC	**F**ace **C**entered **C**ubic
FTO	**F**luorine-doped **t**in **o**xide
GiSAXS	**G**razing-**I**ncidence **S**mall-**A**ngle **X**-ray **S**cattering
GIWAXS	**G**razing-**I**ncidence **W**ide-**A**ngle **X**-ray **S**cattering
GIXD	**G**razing **I**ncidence **X**-ray **D**iffraction
HMS	**H**exagonal **M**esoporous **S**ilica
ITIES	**I**nterface between **t**wo **i**mmiscible **e**lectrolyte **s**olutions
ITO	**I**ndium **T**in **O**xide
KIT	**K**orea **I**nstitute of **T**echnology
LB	**L**angmuir-**B**lodgett
LOD	**L**imit **o**f **d**etection
MCM	**M**obil **C**omposition of **M**atter

MOF	**M**etal **O**rganic **F**ramework
MSTF	**M**esoporous **S**ilica **T**hin **F**ilm
MSU	**M**ichigan **S**tate **U**niversity
MTS	**M**icelle **t**emplate **S**ilica(te)s
NMR	**N**uclear **M**agnetic **R**esonance
PBS	**P**hosphate **B**uffered **S**aline
PEO	**P**oly**e**thylene **O**xide
RE	**R**eference **E**lectrode
SAM	**S**elf-**a**ssembled **m**onolayer
SBA	**S**anta **B**arbara **A**morphous
SEM	**S**canning **E**lectron **M**icroscopy
SHE	**S**tandard **h**ydrogen **e**lectrode
TEM	**T**ransmission **E**lectron **M**icroscopy
TEOS	**T**etra**e**th**o**xy**s**ilane
UME	**U**ltra**m**icro**e**lectrode
ZME	**Z**eolite **M**odified **E**lectrode
ZSM	**Z**eolite **S**ocony **M**obil

Physical Constants

Faraday's Constant	F	$= 96\,485.33\,\mathrm{C\,mol^{-1}}$
Avogadro's Number	N_A	$= 6.022 \times 10^{23}\,\mathrm{M^{-1}}$
Charge on a Proton/Electron	e	$= 1.602\,26 \times 10^{-19}\,\mathrm{C}$
Atomic Mass Constant	a.m.u.	$= 1.66 \times 10^{-27}\,\mathrm{kg}$
Molar Gas Constant	R	$= 8.314\,\mathrm{J\,mol^{-1}\,K^{-1}}$
Specific heat capacity of liquid water	c	$= 4.18\,\mathrm{kJ\,kg^{-1}\,{}^{\circ}C^{-1}}$

List of Symbols

M	Molarity	M ($\mathrm{mol\,L^{-1}}$)
I	Current	A ($\mathrm{C\,s^{-1}}$)
j	current density	$\mathrm{A\,cm^{-2}}$
E	Potential of an electrode versus a refernce	V ($\mathrm{kg\,m^2\,A^{-1}\,s^{-3}}$)
ν	Scan Rate	$\mathrm{V\,s^{-1}}$
P	Power	W ($\mathrm{J\,s^{-1}}$)
A	Area	$\mathrm{cm^2}$
a	tip radius for microelectrode	cm
D	Diffusion coefficient	$\mathrm{cm^2\,s^{-1}}$
δ_j	Diffusion layer thickness for a species j	m
C	Capacitance	F
T	Absolute temperature	K
t	time	s
V	volume	$\mathrm{cm^3}$
R	Resistance	Ω
n	stoichiometric number of electrons involved in an electrode reaction	–
k	rate constant for a homogenous reaction	depends on order
k_{obs}	observable rate constant for the electrochemical reaction	depends on order
k_e	rate constant for a electron transfer between catalyst and the analyte	depends on order
λ	(a) Kinetic parameter (electrochemistry) (b) Wavelength (Physics)	– m
γ	Excess ratio	–
π	Pi	3.1416
$\triangle E$	difference in the peak potential at forward and reverse scan in voltammetry	V
E^0	standard electrode potential for a redox couple	V

$E_{1/2}$	half-wave potential in voltammetry ()	V
E_i	initial potential	V
E_i	junction potential	V
i_{ss}	steady-state current	A
pI	isoelectric point	–

Chapter 1

Introduction

Chapter Plan

Mesoporous materials have been in existence for a long time now. A lot of studies have been done in the past concerning their potential applications in sensing, selective permeation, energy storage, catalysis, etc. [1–26]. In this thesis, we present an approach on how mesoporous materials can be modified to obtain selective catalysis behaviour by controlling the diffusion phenomena and a better understanding of the catalysis phenomenon at mesoporous silica material. Further, we will explain the deposition of mesoporous silica thin layer on a single needle-shaped microelectrode for exploiting the advantages of microelectrodes in combination with mesoporous silica.

In this current chapter, we present a general introduction to porous materials like zeolites, metal organic frameworks, covalent organic frameworks and mesoporous silica. Further, we discuss the various methods of preparation of mesoporous silica and their current applications with a focus on vertically oriented mesoporous silica.

1.1 Mesoporous and microporous materials

The term "nanoporous material" is very commonly used nowadays and represents a relatively broad category of porous materials with pore size below 100 nm. However, these nanoporous materials can be categorized in three different categories which are microporous materials (<2 nm), mesoporous materials (2 to 50 nm) and macroporous materials (>50 nm) [27, 28]. Mesoporous and microporous materials have been one of the most important research topics in recent times due to their large internal surface area, small pore size, and the numerous applications such as adsorption, sensing, separation, catalysis, drug delivery, ion - exchange agents, role as nanoreactors, energy storage, etc. [1–4]. Subsequently, the amount of research focused on the subject of micro- and meso-porous materials has increased significantly. The commonly known porous materials are zeolites, metal organic frameworks, covalent organic frameworks and mesoporous silica which we will discuss in the following sections.

1.1.1 Zeolites

Zeolites are naturally occurring aluminosilicate materials and have been known for over 260 years. The term "Zeolite" was coined by the mineralogist Cronstedt in 1756 from the Greek words, ζέω (zéō) meaning "to boil" and λίθος (lithos) meaning "stone" for minerals which seem to boil when exposed to heat as they expelled large amounts of water adsorbed inside the cavities and the channels of

its structure [29]. A few common zeolite structures with pore sizes from 0.45 to 0.74 nm can be found in figure 1.1.

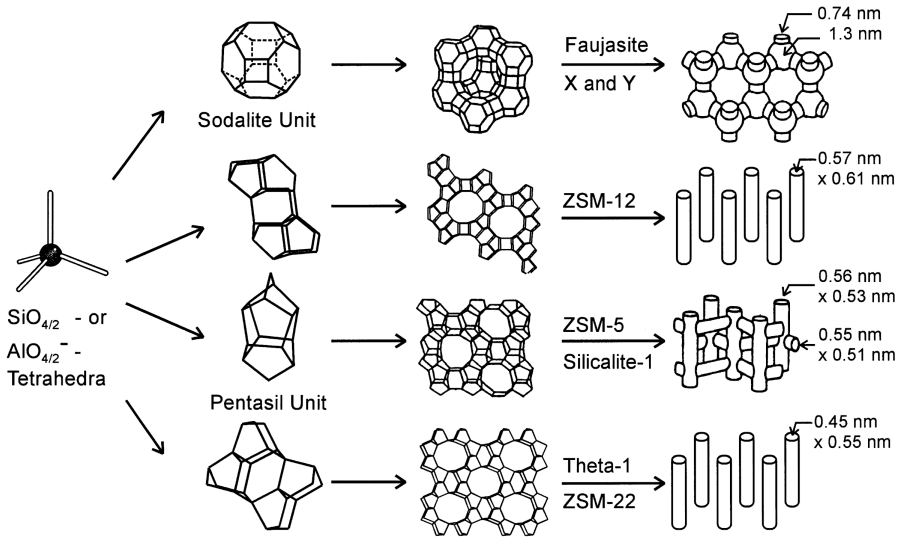

FIGURE 1.1: Structures of different Zeolites. From top to bottom: Faujacite (or Zeolite X, Y), ZSM-12, ZSM-5 and silicalite-1. Figure Reproduced with permission from [5].

Zeolites have a well-defined tetrahedral structure, are highly stable, have low-cost and usually display high ion-exchange properties (with frequently studied metals like calcium, magnesium, copper, cobalt, etc.) [5–9]. They are very commonly used as heterogeneous catalysts due to their high surface area (upto $1000\,m^2\,g^{-1}$) and adsorption of materials [5, 30–32]. The fluid catalytic cracking (FCC) of heavy distillates by faujasites (Zeolites X and Y) is one of the most important chemical processes commercially used throughout the globe [30, 33–36]. The use of zeolites for FCC process was first reported by Mobil inventors, C.J. Plank and E.J. Rosinski in 1964 [37] and the high catalytic activity at zeolites resulted in an improvement of efficiency at production of gasoline by 7%, equalling to tremendous economic benefit for petroleum industries* and less waste of raw materials [33]. This technology is continuously being developed with both the hardware and catalyst technologies being pushed to their current limits [38].
Apart from FCC processes, various other catalytic applications include octane number enhancement of light gasoline by isomerization [39], synthesis of ethylbenzene from benzene and ethene using the Mobil-Badger process [40], synthesis of various molecules like $p-$xylene, $p-$ethyltoulene, diethylbenzene, ethylbenzene, etc. [41] and disproportionation of toluene into benzene and xylenes [42].

*The economic impact was so huge alone in U.S., that it resulted in them getting inducted to the National inventors Hall of Fame in 1979

The catalytic potential of zeolites is still considered to be very high for a variety of applications [5, 35, 43, 44].

Zeolite structures have well-defined cages and a highly porous structures. The unbalanced charge due to presence of aluminium atom in the structure can be charge balanced with group IA and IIA elements such as sodium, potassium, magnesium and calcium [8, 15, 38]. This charge balancing ions can then later be exchanged for others in solution, opening tremendous research and industrial possibilities for zeolites [45]. The Si/Al ratio can also vary the structure of the zeolite, affecting the chemical and thermal stability and consequently would result in the applications of the structure [46]. Low Si/Al ratio results in a higher structural Al content leading to a larger number of charge compensating cations in the structure. Such zeolites find applications as efficient ion exchangers (Zeolite A, X). An increase in Si/Al ratio would result in increase in thermal stability of the material (MCM-22, ZSM-5) upto pure silica structures (silica zeolites). Different Zeolite structures have uni-, bi- and tri-dimensional channels, with interconnections in different ways leading to a much higher porous structure with a much large internal surface area. The pore size as mentioned earlier is in microporous range (less than 2 nm), imparting size selectivity in terms of ingress of cations or molecules into the intra-crystalline voids [46].

Zeolites are now commonly used as modifying layers on an electrode surface and the resultant composite is often known as Zeolite modified electrode (ZME). [5, 8] Various properties of ZME set them apart from the conventional electrodes. The ZMEs combine the advantages of an ion exchange voltammetry with the size selective sieving properties of a zeolite while also combining the interesting properties of zeolites like high thermal stability, ion exchange properties, size selectivity, etc. with the highly sensitive modern electrochemical techniques making it a viable material for high efficiency sensors [8, 10–12]. Due to the same reasons, it is also a highly interesting material to be used for electrocatalysis systems as well.

Different ZME synthesis procedures have lately been studied by different groups. The common processes include dispersion of zeolite particles into a composite conducting matrix [11, 47–50], formation of polymer-zeolite particles followed by thin films formation on solid electrode surfaces [51–57], pressure-driven mechanical immobilization of zeolite particles [18, 58], or formation of zeolite-polymer membranes by dispersion of zeolite particles into a non-conductive organic resin [59].

As an example, Zeolite Y particles after iron (III) exchange have earlier been deposited on a graphite modified electrode with an inert polymer as a binder and

have successfully been applied to the detection of ascorbic acid [52] and uric acid [52, 57]. The exchanges with iron (III) were followed by a simple immersion of grounded zeolite in a 0.01 M solution of $FeCl_3$ for 24 to 48 h. Another study with Zeolite Y particles was reported by Mallouk et al. with a zeolite particle diameter of ∼1 µm and a small amount of polystyrene as binder in THF to cast a film on SnO_2 electrode with a thickness of 60 µm. This resulted in only the first few micrometers of zeolite on the electrode surface which is active for electrochemical reactions followed by the layer of polystyrene. The zeolite layer was modified with known cationic redox probes like $Ru(bpy)_3^{2+}$ and $Co(CpCH_3)_2^+$ by soaking the electrode in the respective solutions before being used for electrochemical studies [56]. Substantial work has been done earlier to the development of voltammetric biosensors based on ZMEs, such as glucose ([60]), phenols [61], dopamine or epinephrine [62], etc. A lot of reviews and monographs have been devoted in the past focusing on the development of Zeolites, their various properties and their applications [8, 10–21].

Since a large variety of zeolite materials are described in literature (largely in patent literature), it becomes difficult for researchers to understand if the reported material contains new structures or represents variants of already known structures. Structure commission of International Zeolite Association (IZA) overlooks the approval of new structures and assigning of a three letter code to the zeolite materials.

1.1.2 Metal Organic Frameworks (MOFs)

One of the most famous microporous nanostructures are Metal-organic Frameworks, which have been developed after studies on the naturally-occurring Zeolite structures. MOFs are a class of highly porous crystalline materials which consist of metal ions and organic ligands simply bonded together by coordination bonds. The choice of metal and linker significantly affects the structure and properties of MOF. The organic and inorganic parts form an integral part of the network and form continuous bonds in at-least one-dimension to give the complete crystalline structure.
MOF structures are very diverse in terms of their chemical composition as well as their geometrical structure [63]. At present ∼90 000 MOF structures have already been synthesized and ∼500 000 MOF structures are predicted with pore sizes ranging from 0.24 to 7 nm [64–66].
The main attention MOFs seek actually comes from their large and uniform porosity [67], implicating a huge potential in fields like gas storage [68], catalysis [69, 70], adsorptive separation [71, 72], membrane separation [73], etc.
MOF structures have been synthesized with a wide range of metals and involve a diverse range of organic ligands. A lot of work has been attributed to transition metals including Zinc, along with p-block elements like aluminum, gallium, tin, magnesium, etc. Some work can also be found involving rare earth elements which have been of keen interest for their optical properties [74].
In terms of the organic ligands, carboxylic acids have been proved to be very versatile. Different forms of carboxylic acids (mono-, bi- and tri-) have been used for a lot of different MOF structures. Along with carboxylic acids, phosphonic acids and phenolic acids also appear in a wide range of hybrid structures [63, 75]. Apart from the above ligands involving oxygen bonds, there are other ligands such as pyridyls and imidazoles, as well as other mixed ligands, which form $M-O$, $M-N$ or $M-S$ bonds [75].

MOFs are synthesized like their natural counterparts, zeolites, except that the procedure for zeolites employs a contemporary template growth approach, in which, the growth is controlled using a template and the template is later removed to get a geometrically aligned structure, while MOFs on the other hand are constructed mostly by using preformed ligands and metal ions, and thus, tailoring the same can also control the structure of MOF completely.

The synthesis of MOFs is basically dominated by molecular scale assembly of coordination bonded metal ions and organic ligands. The initial reaction between metal ions and organic ligands leads to the formation of MOF nuclei at

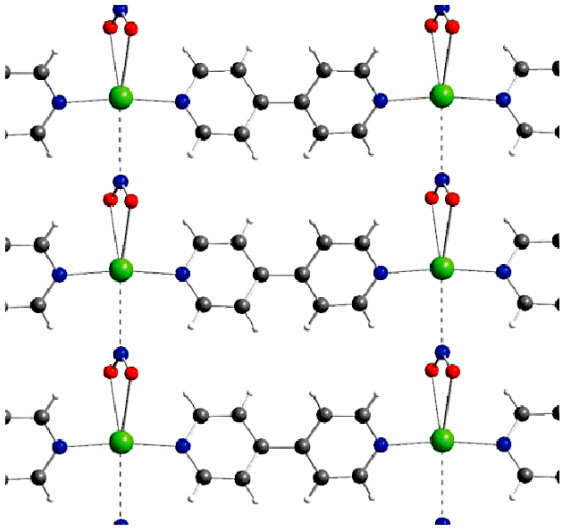

FIGURE 1.2: 1D MOF structure of Silver bonded with $4,4' - \text{bipyridyl}$ and $\text{bi} - \text{dentate nitrite}$ anions [75]. Figure reproduced with permission from [76].

first, which is then followed by crystal growth processes by a continuous coordination bond formation at the surface of the nuclei [69].

A vast range of MOFs, also known as porous coordination polymers (PCP), have been synthesized over the recent years with different dimensionalities, i.e., 1-D, 2-D and 3-D. These dimensionalities arise from the continuity of the basic MOF unit structure in a particular direction(s). Examples of 1-D chain system MOFs would include $\text{Ag} - \text{N}$ bonding system through a linear $4,4' - \text{bipyridyl}$ group [75]. Due to the linearity in the silver linkage, the chain also becomes linear as well (figure 1.2).

2-D systems can be explained using a very simple example of nickel ions connected via square planar coordination bonds with imidazolate anions to form a simple layered structure [76]. An example of 2D structure employing a rare earth metal is Terbium (Tb^{3+}) coordinately bonded with $\text{thiophenylisophthalic acid}$ to get a product which also shows an enhanced green luminescence [77]. Eu^{3+} also forms a complex with isophthalic acid to give a 2D MOF (Figure 1.3) [74].

3D MOF structures have been synthesized by many groups. One good example would be that by Carlucci et al., who reported open-framework structures based upon metals like silver and ligands such as pyrazine (figure 1.4) [78]. Many other relevant works in 3D MOF structures have been done by Yaghi, O'Keeffe and co-workers; Susumu Kitagawa et al.; Férey and coworkers; etc. wherein they bridged Zn_4O groups using $\text{benzene} - 1,4 - \text{dicarboxylicacid}$ to get a framework

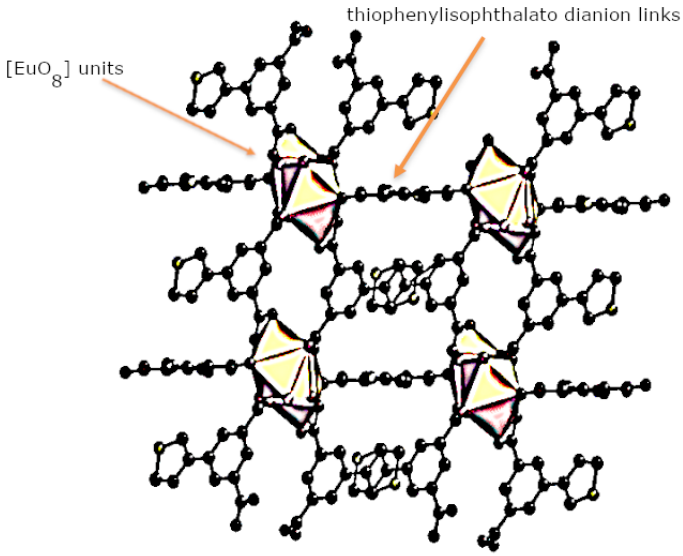

FIGURE 1.3: 2D MOF structure of Europium isophthalic acid complex [74].

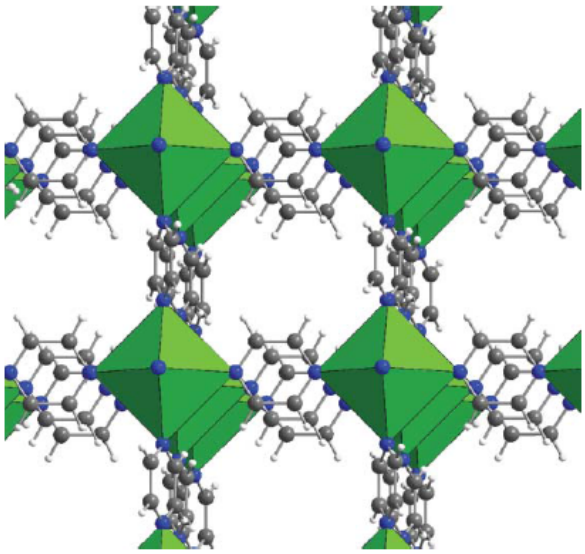

FIGURE 1.4: 3D MOF structure of Silver pyrazine hexafluoroantimonate. Figure reproduced with permission from [76].

with extremely low density and a high porosity. This framework is also known as MOF-5 [79].

There are very significant applications of MOF structures:

- Sensing Applications: A typical example would be the luminescent property observed in case of MOF which include Lanthanide or some other aromatic flurophore in the structure. When such a MOF comes into contact with a specific analyte an optical signal is produced which can be used to detect the analyte in these cases [80–82]. The advantage with using MOF lies in the high surface area of these structures. Due to the high surface area (highest being $7000\,m^2\,g^{-1}$ (BET) [83, 84]), we obtain a higher number of reaction sites improving the sensitivity of system.
- Molecular separation is a much sought out phenomena of MOF. MOF structures are used to get both adsorptive separation [71, 72] as well as permeation separation [73] (using 2D MOF membranes). But, efficient and large scale separation processes would require defect-free, highly selective (for adsorptive separation) and localized thin porous structure (thin membranes for permeation separation).
- Proton and electric conduction of MOF structures have been reported, making them viable candidates for use for proton exchange membranes, batteries and fuel cells [85–87].

The main difficulty in synthesizing MOF superstructures with the desired dimensionality lies in developing suitable methods to localize such coordination reactions within a desired space. From recent investigations of MOF crystallization processes, along with the application of synthetic protocols of solid state materials and modern micro-fabrication technology to MOF synthesis, the shaping of MOFs in the micrometer or sub-micrometer scales has been realized. The high precision of spatial localization of the reactions do form localized structures but most of these processes are very difficult and require extensive instrumentation only with a relatively low output. A drawback for the MOF based material lies in the insulating nature of most of the existing MOFs as it hampers their adaption as electrode materials and as electrocatalysts [88]. In addition to this, the stability of MOF-based materials remains a critical issue [88].

1.1.3 Covalent Organic Frameworks (COFs)

Covalent organic frameworks (COFs) are crystalline porous organic polymers which were introduced by Yaghi et al. in 2005 by reversible processes such as condensation of two-dimensional (2D) and three dimensional (3D) organic building precursors [89–92]. COF structures contain light elements (such as H, B, C, N, O) and are interconnected by strong covalent bonds via reticular chemistry displaying a network structure. Many such COFs can further undergo reaction to accommodate metallic functionalities to exhibit catalytic properties. An example of such a structure is COF-LZU1 (figure 1.5), made using $1,3,5-\mathrm{triformylbenzene}$ and $1,4-\mathrm{diaminobenzene}$ [93]. COF-LZU1 has an eclipsed layered sheet structure with a pore size of 1.8 nm (figure 1.5a) and can incorporate metal ions such as Pd in it's structure through a simple reaction at room temperature. The incorporation of Pd allows the COF-LZU1 to catalyze the Suzuki-Miyaura coupling reaction with a high yield of 96 to 98 % along with high stability and easy recyclability, as is demonstrated elsewhere [93].

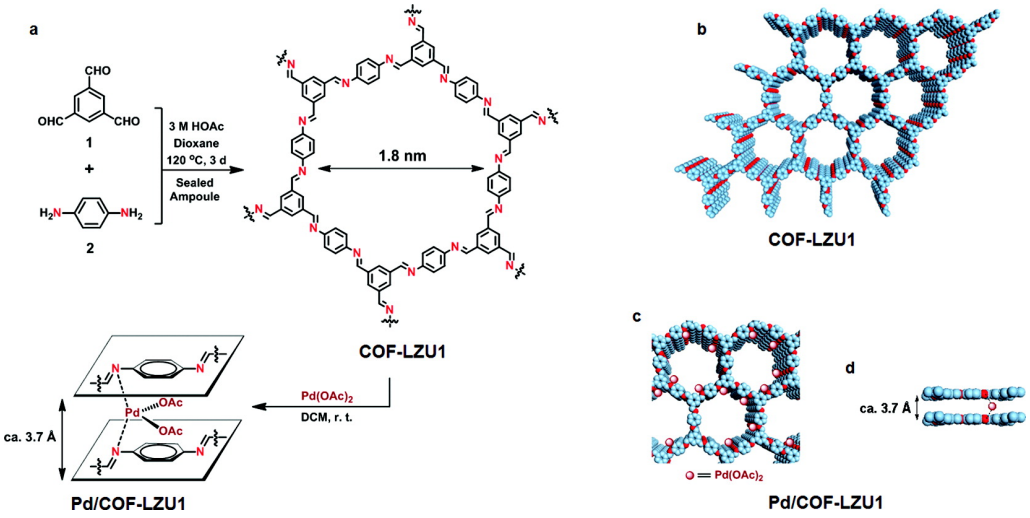

FIGURE 1.5: Schematic of (a-b) synthesis and (c-d) geometrical porous structure of COF-LZU1 and Pd/COF-LZU1. Reproduced with permission from [93]

A variety of methods have been proposed for COF synthesis in the recent years involving various processes like solvothermal synthesis, ionothermal, sonochemical, mechanochemical, light promoted synthesis and microwave synthesis [89, 94–105]. Some reversible reactions leading to the successful generation of COF building units are given in figure 1.6. From these reactions, a variety of building units have been successfully used to construct COF materials as can be seen in figure 1.8 [100]. Similar to MOF structures, COFs can be synthesized with

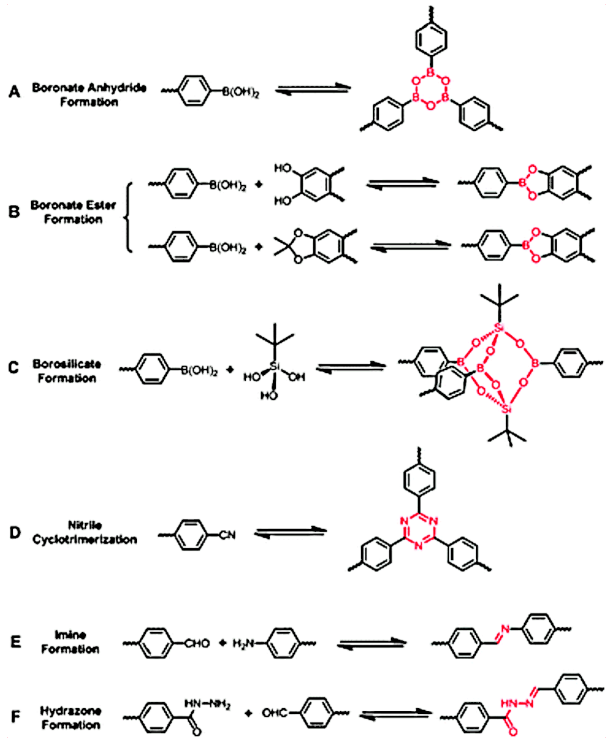

FIGURE 1.6: Reversible reactions leading to successful development of molecular units for COF materials. The bonds formed are highlighted in red. Figure reproduced with permission from [100]

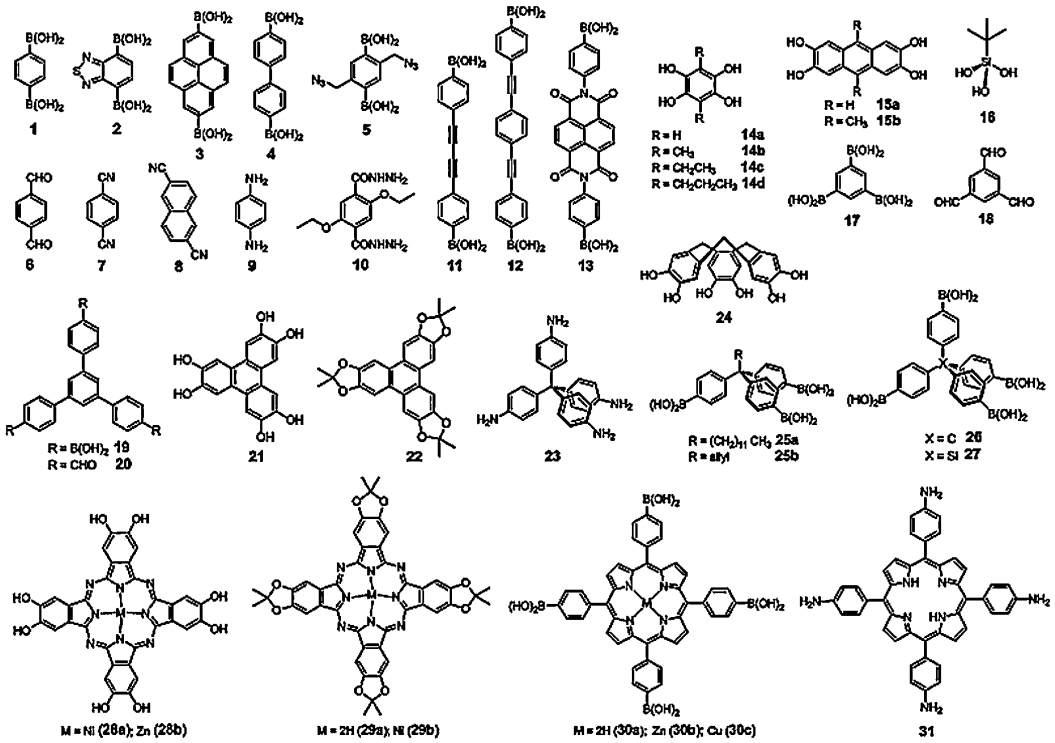

FIGURE 1.7: Building Units successfully utilised for synthesis of COFs. Figure reproduced with permission from [100]

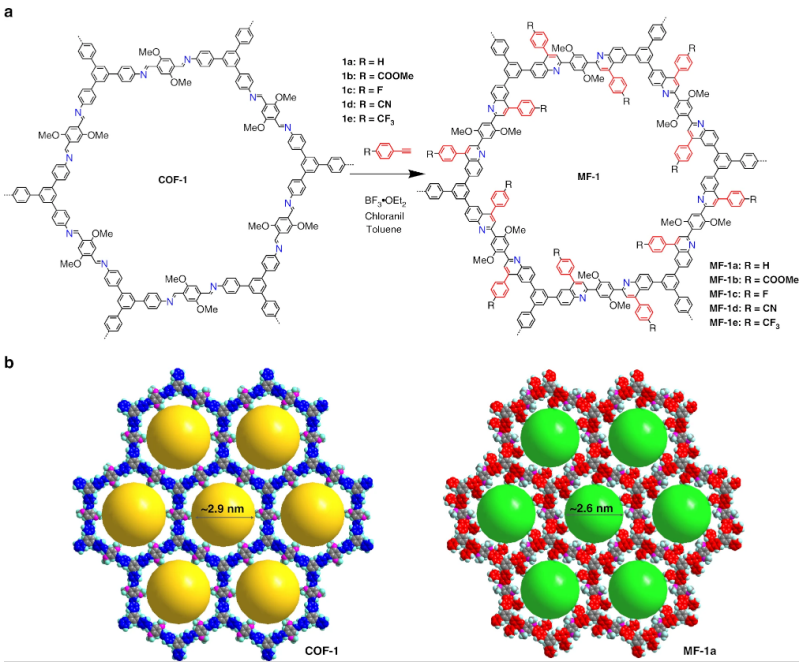

FIGURE 1.8: Post-synthesis modification of COF-1 via aza-DA reaction (a) scheme showing transformation of single lattice unit (b) simulated modeled structure showing illustration of extended frameworks of COF-1 and MF-1a. Yellow and green spheres represent the respective cavity inside the structures. Figure reproduced with permission from [112]

different structural regularities in 1D, 2D and 3D depending upon the building units used [89, 106, 107]. The COF structures display self-healing abilities and thermodynamically controlled dynamic covalent chemistry resulting in a long-ranged ordered crystalline structure. COFs usually have a lower density than MOFs and display excellent stability in variety of solvents and under varying pH and oxidative/reductive conditions. Due to the stable structure, COF structures can withstand harsh conditions without affecting the ordered structure and crystallinity. An absence of metals and strong covalent bonds instead of coordinate bonds give it a more stable structure in comparison to MOFs.

Apart from this, the $\pi - \pi$ stacking and hydrogen bonding further improves the overall strength of the skeletal and pore structure of the COFs and protects them from solvation and hydrolysis. In comparison to zeolites and porous silica based materials, COFs offer higher porosity, and more tunable pore sizes. The high porosity increases the diffusion through them promoting higher sensitivity and selectivity for enhanced analytical and catalytic applications [89, 100, 108–111]. A lot of research is currently devoted to COF materials to enhance their stability

and make them more robust. An example can be the demonstration of transformation of a imine-linked COF (COF-1) via a simple organic reaction that can lead to change in unit structure and pore size, enhancing their stability and leading to conductive bonds, as shown in figure 1.8 [112]. The structure tunability of the imine-linked COFs and the substrate diversity of the aza-Diels-Alder cycloaddition can lead to a large variety of functional moieties introduced to modify the COF structures.

COFs have demonstrated applications in a variety of fields such as gas adsorption [113–115], separation [116], chemical sensing [117–119], catalysis [93, 120, 121], optoelectronics [122–124], and energy storage [125]. A few reviews have been published in recent years detailing the various advancements in the fields of COF [100, 101, 108, 126–130].

1.1.4 Mesoporous Silica

Ordered mesoporous silica was first synthesized in 1992 by a research team from '*Mobil Oil Company*' with the generation of a new family of materials called 'M41S' [131, 132]. These materials were prepared using a template based growth approach and resulted in ordered pore distribution and homogeneous structure with sizes ranging from 2 to 10 nm. It was shown to consist of different shapes and materials like $\mathrm{MCM}^{\dagger}-41$ (hexagonal), $\mathrm{MCM}-48$ (cubic), and $\mathrm{MCM}-50$ (lamellar) (figure 1.9) [131–133]. They are also called under a generic name "micelle-templated silica(te)s (MTS)", and had given rise to well-defined diffraction pattern due to their crystalline structure [131, 132, 134].
In fact, in 1990, Yanagisawa et al., had described a synthesis methodology for mesoporous silica with a uniform pore size, however, the pores at these materials were generally irregularly spaced and the size distribution was large [135]. Thus, the M41S materials are generally considered to be the first of the series of ordered mesoporous structures.

Among the materials reported by Kresge et al., $\mathrm{MCM}-41$ is very interesting as it allows for generation of customizable pores between 1.5 nm to 20 nm, a wall thickness of 1 nm to 1.5 nm and a surface area of approximately 1200 $m^2\,g^{-1}$ [136].

Various different silica based mesoporous materials have followed suit since M41S,

[†]Mobil composition of matter type

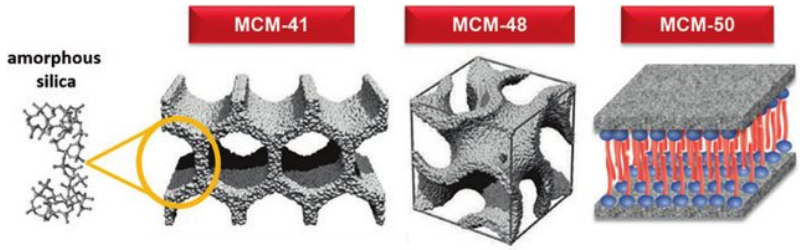

FIGURE 1.9: Members of M41S family. MCM-41, MCM-48 and MCM-50. Figure reproduced with permission from [46].

for example, SBA[‡], HMS[§], MSU[¶], KIT[||], etc.
$SBA-15$ has a hexagonal mesoporous structure with a controllable pore size from 5 nm to 30 nm with micropores connecting these mesoporous channels and a wall thickness of 3 nm to 6 nm [137]. HMS is prepared using neutral amine as a template and it possesses a slightly disordered hexagonal structure with thicker walls. It has a superior thermal stability when calcinated in air, and a smaller crystal structure [138]. $MSU-1$ is synthesized using polyethylene oxide (PEO) as the template molecule and also has a disordered channel structure. This material has a larger wall thickness and a smaller particle size with considerable mesoporosity due to pores which are formed between the small particles [139].

At the surface of the mesoporous silica materials there are silanol groups that can be utilized for enzyme immobilization by hydrogen bonding between hydroxyl groups and carbonyl or amino groups on enzyme molecules. The surfactant is crucial in the synthesis since it decides the size of the pores formed at the silica, and a wide variety of different surfactants can be used for this function. The main surfactant used in mesoporous synthesis is non-ionic block copolymers

1.2 Preparation and application of mesoporous silica

Mesoporous materials consist of inorganic metal oxides, like silica or alumina, and have pore sizes in the range of 2 to 50 nm. For the scope of this thesis, we focus on mesoporous silica and describe a few common routes to synthesize it on a given substrate.

[‡]Santa Barbara Amorphous
[§]Hexagonal mesoporous silica
[¶]Michigan State University
[||]Korea Institute of Technology

1.2.1 Sol-gel process

The sol-gel process is an established method to produce materials with desirable properties. Materials with applications in surface protection, optical and electrocatalytic applications have been reported to be developed earlier using this method. The sol-gel method employs the "bottom-up" approach for formation of a network structure by employing molecular building blocks which are self assembled to give the required structure.
The sol-gel method of deposition is a 2-step process consisting of hydrolysis of a silica precursor followed by a subsequent condensation of the silanol groups ($\equiv Si-OH$) on the required substrate [140, 141]. A Sol is a stable suspension of colloidal particles with size ranging from 0.001 to 1 µm in a suitable liquid solvent. A gel is a porous three dimensional continuous solid network. The typical precursors of a sol-gel process for silica are alkoxysilanes ($Si(OR)_4$) with different alkoxy groups such as methoxy (tetramethoxysilane / TMOS) and ethoxy (tetraethoxysilane / TEOS). The hydrolysis and condensation reaction are given by equations 1.1 - 1.3 and are highly dependent on the pH of the solution as can be seen from figure 1.10. The varying degree of hydrolysis are described by the factor n upto a maximum value of 4. A higher value of n, describes a higher cross linking of silica, results in a much denser network.

Hydrolysis of Silica precursor

$$Si(OR)_4 \quad + \quad n\,H_2O \quad \longrightarrow \quad Si(OR)_{4-n}(OH)_n \quad + \quad n\,ROH \tag{1.1}$$

Condensation of Hydrolysed Silica

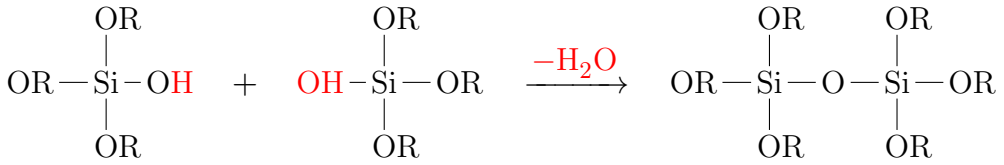

(1.2)

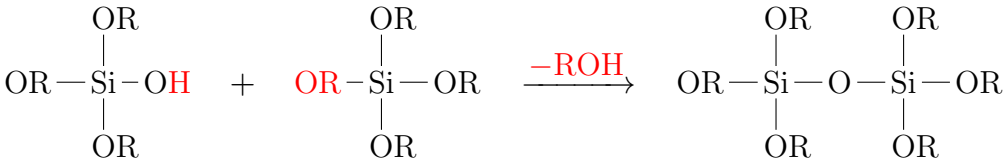

(1.3)

The condensation process results in the formation of siloxane groups ($Si-O-Si$) with the subsequent alcohol and water as a by-product. The evaporation of the solvent and the alcohol leads to a solid silica network. The silica sol-gel processes are pH dependent and different pH value favours the hydrolysis or condensation

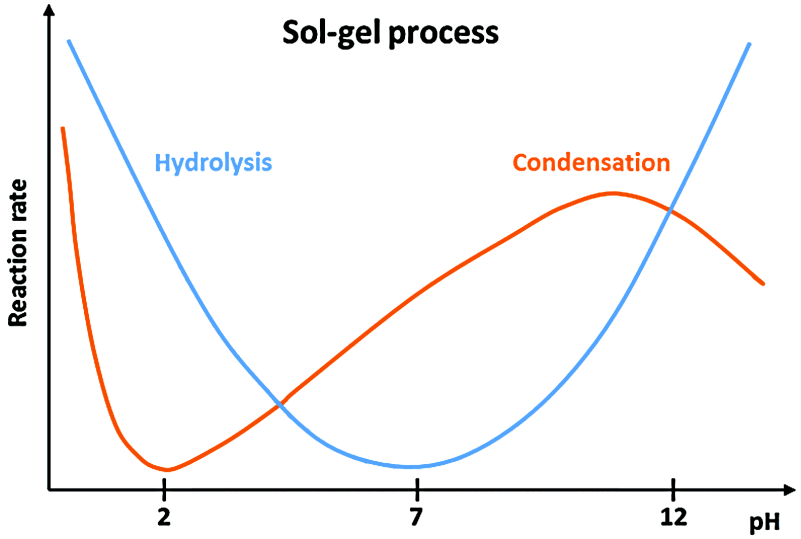

FIGURE 1.10: Reaction rates of tetraethylorthosilicate (blue curve) hydrolysis and (orange curve) condensation as a function of pH. Figure reproduced with permission from [142]

of the silica as can be observed from the figure 1.10.

The earliest proposed method of mesoporous silica synthesis includes liquid crystal template method where a surfactant liquid crystals serve as organic templates for the formation of the mesoporous structure as given in figure 1.11 [131, 132]. The surfactant molecule used in the procedure were quaternary ammonium cationic surfactant compounds with the general formula $C_nH_{2n+1}(CH_3)_3NX$, where X=Cl or Br and n = 8, 9, 10, 12, 14 or 16. The template removal was done through calcination at 540 °C for 1 h in N_2 flow followed by 6 h in flowing air. A schematic of the process is given in figure 1.11.
This method describes the general methodology of the mesoporous silica synthesis and postulated the concept of "template" in the synthesis of mesoporous silica. The surfactant molecules forming regularly aligned assemblies were used as a soft template for the deposition of the metal oxide and was followed by the template removal. The removal of the template can be followed through different appropriate methods like calcination, solvent evaporation, dissolution of the template in a suitable solution, etc. The electrode modification processes improve the analytical properties at the electrode such as faster electron transfer, enhanced electrochemical response, selective permeation and sieving properties, stability, reproducibility, etc. These properties further impart higher sensitivity and selectivity properties to an electrode or electrode protection from fouling, corrosion, etc. all of which aid expected electroanalytical processes. A few reviews have been reported summarizing the advances in the field [2–4, 22–26].

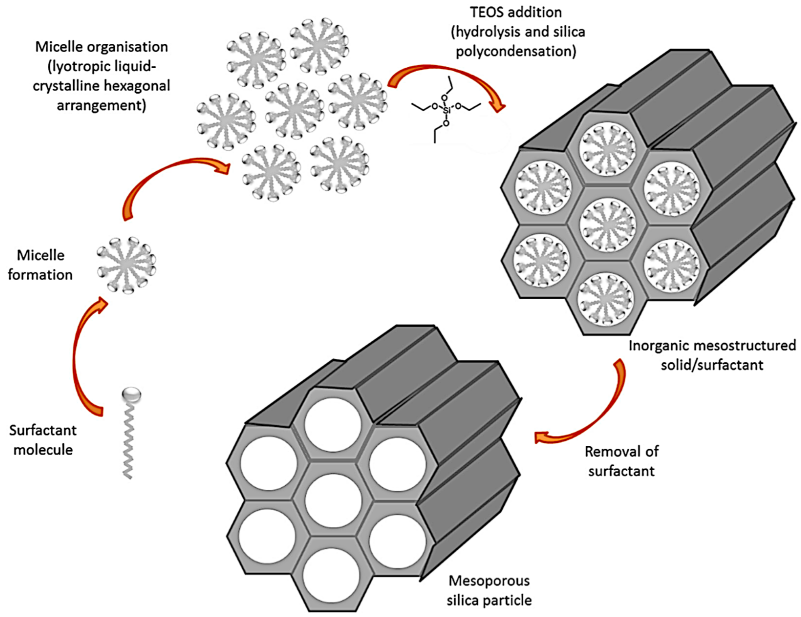

FIGURE 1.11: Schematic of the synthesis of mesoporous silica through liquid crystal template method. Figure reproduced with permission from [143].

The different electrode modification processes commonly used are dip coating, spin coating, electrochemical deposition, polymerization, etc. and the common modifiers for the electrode to impart mesostructuration include organic ligands, micro-/nano-structures, ion-exchangers, clays, zeolites and silica based materials [22–24].

There are various routes of modifying an electrode with silica thin films. Stöber growth approach has been studied in the past to develop mesoporous silica thin films of ∼155 nm and a pore size of ∼2.3 nm [144]. Evaporation-induced self-assembly (EISA) method, which is based on dip coating of mesoporous silica coupled with controlled evaporation of the solvent, has also been shown to deposit mesoporous silica thin films with pore sizes ∼2 nm on substrates in some reported articles [22, 145, 146]. Chemisorption process which refers to adsorption of self-assembled monolayers (SAMs) on an electrode is also very commonly used for many electrodes. A typical example of an adsorption process is attachment of a sulphur-containing molecular species on gold or mercury surface due to strong metal-sulphur interactions [147, 148]. Langmuir-Blodgett films which are commonly used in biological applications, also rely on surface adsorption of molecules to form monolayers. Langmuir-Blodgett films of mesoporous silica coated gold nanorods have been reported in an earlier study [149]. Monolayers of SBA-15 particles have also been reported to be deposited on electrodes using langmoir-blodgett method [150]. Covalent bonding of a modifier can also

be achieved at an electrode through a suitable chemical reaction of the modifier at the electrode. A common example of covalent bonding of modifiers is electrografting process of organosilanes which results in a strong interaction with the electrode [151–153]. These electrografted molecules are also used as linking agents to have a stronger adhesion to silica or a suitable modifier for deposition of a thin film for a particular interest [154]. Another common route is to deposit a composite of a suitable modified material like carbon-paste on an electrode through physical or chemical processes. Carbon paste matrix can be used to include a variety of inorganic or organic/organometallic materials to develop a composite electrode [155]. There are also various studies on deposition of conductive or non-conductive polymer films on an electrode through various attachment processes. These polymeric films can have chemical modifiers in place or are commonly functionalized to obtain required properties [156, 157]. Nanocasting process involving the deposition of a preformed mesoporous template material has been shown to be useful method of introducing mesostructuration at an electrode [158].

1.2.2 Vertically oriented Mesoporous silica

Mesoporous silica thin films deposited from a variety of reported methods are not spatially aligned or align parallel to the substrate making it difficult to use them for a variety of purposes where the diffusion at the electrode is required but it is not directly accessible. To overcome this challenge, vertically oriented mesoporous silica have been reported using methods like "nanometer-scale epitaxy" [159] or "electrochemically assisted self assembly method (EASA)" [160, 161]. EASA method as reported by Walcarius et al. describes a single step electrodeposition method for silica deposition at a suitable electrode. The nanometer-scale epitaxial growth approach reported by Tolbert et al. describes an approach involving a pre-treatment of the substrate for a template formation, followed by growth of ordered mesoporous silica [159]. A disadvantage of the epitaxial growth approach is that it requires an exact lattice matching of the substrate pattern with the mesoporous deposit and a lattice mismatch affects the pore structure of the silica deposit as well. It was shown that the vertically oriented pores were missing in the silica deposit at a mismatch of 33%. Multiple deposition steps and the limitation in the procedure due to lattice mismatching make this process more complicated than the EASA method.

Some different approaches to obtain vertically oriented mesoporous silica include Stöber-solution growth approach [144, 162] A comparison of pore order, film

thickness and pore size of vertically oriented mesoporous silica grown by EASA and Stöber-solution method on titanium nitride substrate was recently reported [163]. A recent study also reported that oil-induced co-assembly process in which the addition of an oil (i.e. decane) to the sol increase the pore size (up to 5.7 nm) and induces vertically oriented mesoporous silica [164]. But the time required for deposition was 6 h which is much higher than that required for EASA method.

EASA approach was reported by Walcarius et al. in 2007 and has been used for deposition of vertically aligned mesoporous silica on different electrodes like indium tin oxide (ITO), fluorine doped Tin Oxide (FTO), gold, glassy carbon, platinum, copper, etc. [154, 160, 161, 165–167]. With the electrochemically assisted self assembly (EASA) approach the deposition process is much faster, simple and repeatable. It does not require any pre-treatment of the sample and the synthesized films have a long range order, with customizable pore size from 2 to 3 nm [25, 160, 161, 168].

In EASA approach, a suitable reductive potential is applied to an electrode which is immersed in a pre-hydrolysed solution of the silica precursor (TEOS) and the surfactant molecule (eg. $\mathrm{cetyltrimethyl\ ammoniumbromide(CTAB)}$). At this reductive potential, two different processes take place. Firstly, we observe a deposition of the cationic surfactant $\mathrm{CTA^+}$ at the electrode. Secondly, reduction of $\mathrm{H^+}$ and $\mathrm{H_2O}$ causes a generation of hydroxide at the electrode surface increasing the local pH at the electrode interface inducing the self-assembled polycondensation of the sol resulting in the formation of surfactant-templated mesoporous silica thin films on the electrode surface. The pore size obtained by this method has shown to vary from 2 to 3 nm depending on the carbon chain length of the surfactant used while maintaining the mesostructure of the silica thin film [169]. The pore density of the film was calculated to be approximately 75 000 μm^{-2} [160]. The steps for deposition of mesoporous silica are further discussed in detail later in section 2.4.1.

1.2.3 Current Applications and prospects

Vertically-aligned hexagonally packed mesoporous silica films deposited on an electrode provide an excellent configuration to investigate the charge and mass transport phenomena in individual mesopore channels. Such films generated through EASA process have long ranged order and have already been shown to display fast mass transport of solution-phase redox probes through the silica film and have successfully been employed for sensing applications [26, 170–172].

An interesting scheme given by Walcarius in a recent review shows some configurations of mesoporous silica and a few analytical applications as depicted in figure 1.12 [3]. Different applications of vertically oriented mesoporous silica are presented such as electrode protection from bio-fouling [173], molecular sieving [169], cationic accumulation [170], electrochemiluminescence signal enhancement [172], enhanced electrochemical detection at mesoporous silica based electrodes modified with organic groups [174], nanowires [175], DNA-grafting [176] or after transfer of the silica film to nano-ITIES** [177].

There have been studies on deposition of conductive materials in mesoporous silica for a high density planar array of metallic or polymeric nanowires. These composites show potential in furthering the uses of mesoporous silica for semiconductor industry applications, super-capacitors, redox-active silica based organic-inorganic hybrids, etc. [178–181]. Vertically oriented nanowires of gold, silver and copper have been deposited using mesoporous silica as a template [182–185]. Deposition of polymers like polyaniline, $\mathrm{poly}(3,4-\mathrm{ethylenedioxythiophene})$, polythiophene and polypyrrole has also been studied in some earlier reports [186–193]. For polyaniline deposition in mesoporous silica, it was reported that the growth of polyaniline can be controlled through the experimental conditions by tuning the electrodeposition parameters [186]. Ordered mesoporous polymers of divinylbenzene and ethyleneglycoldimethacrylate were prepared from colloidal silica spheres as well [194]. A recent review from Laskowski et al. discusses the advances of mesoporous silica in electronics-oriented applications [180].
In an earlier study, an enhancement of ∼107-fold in the electrochemiluminescence signal has been reported at mesoporous silica modified ITO electrode in comparison to bare ITO using $\mathrm{tris}(2,20-\mathrm{bipyridyl})\ \mathrm{ruthenium(II)}\ (\mathrm{Ru(bpy)_3^{2+}})$ probe resulting from the electrostatic interactions and has been used for detection of TPrA, nicotine and atropine (figure 1.12C)[172]. This result displays the potential of mesoporous silica with techniques other than electrochemistry as well. A recent study also showed the effectiveness of drug-encapsulated lipid-coated biodegradable mesoporous silica nanoparticles (dHMLB) towards regulation of tumour environment. The study demonstrated significant inhibition of tumour growth and metastasis, and exhibited favourable biodegradability and safety [195]. The negative charge at silica at neutral pH allows for an adsorption of cationic species like ruthenium trisbipyridine $(\mathrm{Ru(bpy)_3^{2+}})$, methylene blue, paraquat and diquat in the mesopores of the silica thin films [167].

Apart from these applications, the possibility to functionalize these silica deposits

**nanometric interfaces between two immiscible electrolyte solutions

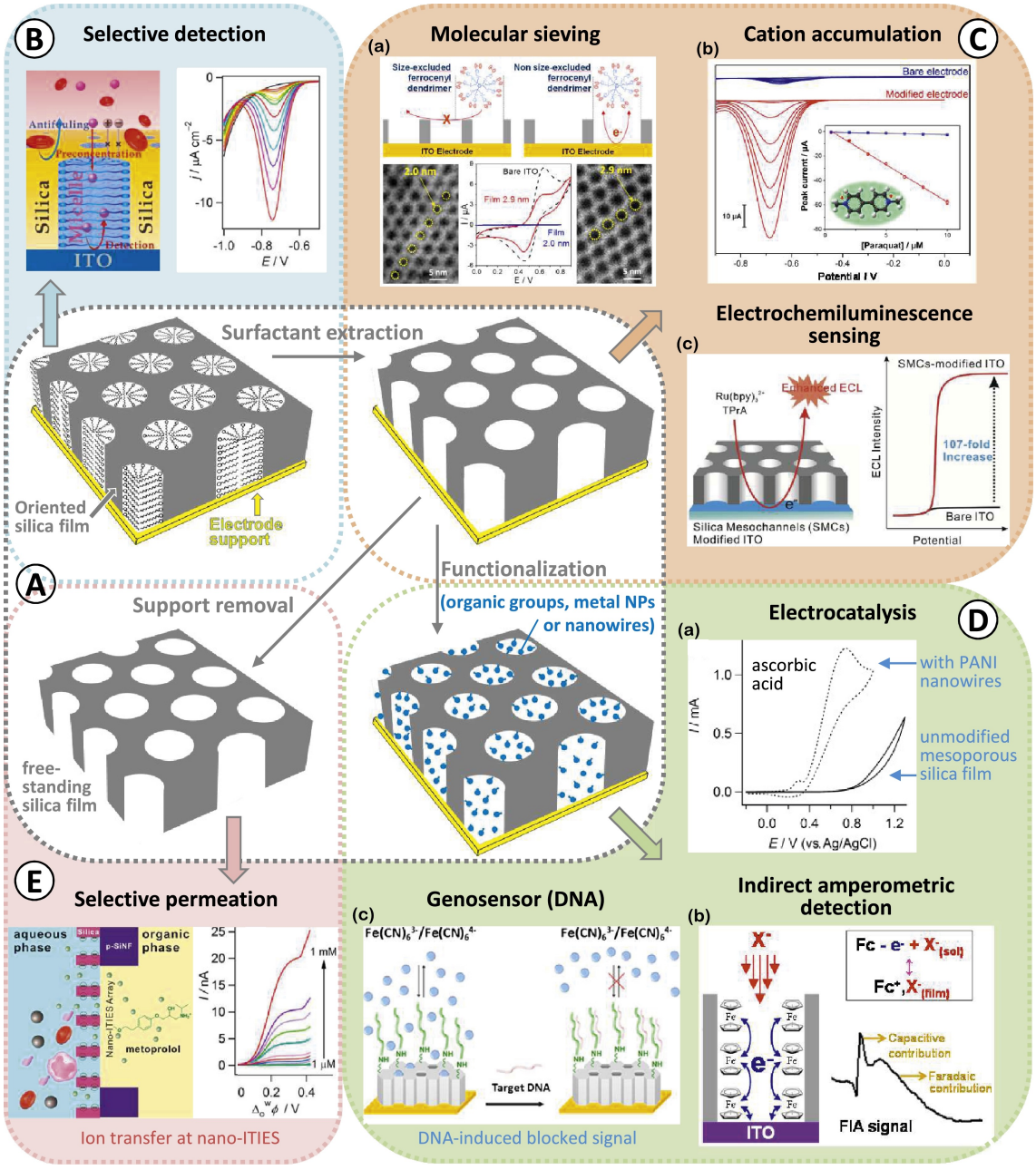

FIGURE 1.12: Scheme representing (A) different configurations, and (B-E) different electroanalytical properties at the vertically-oriented mesoporous silica coated electrode. Figure reproduced with permission from [3]

with other molecules can impart a variety of properties to these films. Various strategies have been reported in the past to functionalize the surface or the mesochannel walls of mesoporous silica deposits. Various silane molecules are employed for these purposes with terminal groups like $-NH_2$, $-SH$, $-N_3$, $-CH_3$ etc. and are introduced inside the silica structure by addition of the respective organosilanes to the precursor solution for the co-condensation process [161, 165, 166, 196–200]. However, an optimum concentration is required to be maintained to preserve the ordered and porous structure of the silica and to avoid blockage of the mesochannels. In a reported article, azido and thiol group precursors were co-deposited in a mesoporous silica thin film using $3-\mathrm{azidopropyltrimethoxysilane}$ (AzPTMS) and $\mathrm{mercaptopropyltrimethoxysilane}$ (MPTMS) simultaneously in a silica thin film [197]. These functional groups were functionalized with $\mathrm{ethynylcobaltocenium/vinylferrocene}$ and $\mathrm{propargyl\ alcohol/allyl\ cyanide}$ to demonstrate the feasibility of such a bifunctional modification.

In the following chapters, we discuss the oxidation of thiols (cysteine, glutathione and homocysteine) at electrodes modified with mesoporous silica thin films and further investigate the various characteristics concerning this oxidation reaction. The different reaction rates and sizes of molecules have an impact on the oxidation reaction and the understanding has been exploited to obtain a system with selective oxidation of cysteine over glutathione.

Chapter 2

Experimental Section

Chapter Plan

2.1 Chemicals and Reagents

The specifications for all the chemicals used in the different experimental procedures can be found in Table 2.1 as follows:

TABLE 2.1: Chemicals and reagents used in the experiments

Chemical Name	**Molecular formula**	**Molecular Mass ($g\,mol^{-1}$)**	**Purity**	**Supplier**
Mesoporous Silica Deposition				
Tetraethoxysilane (TEOS)	$C_8H_{20}O_4Si$	208.33	98 %	Alfa Aesar
Cetyltrimethylammonium bromide (CTAB)	$C_{19}H_{42}BrN$	364.45	99 %	Acros
Ethanol	C_2H_6O	46.07	95 to 96 %	Merck
Water	H_2O	18.02	N/A	Millipore system
Hydrochloric acid	HCl	36.46	36.5 - 38 %	Merck
3-azidopropyltriethoxysilane	$C_9H_{21}O_3SiN_3$	247.37	(Synthesized in lab)	
Redox Probes				
Potassium hexacyanoferrate (III)	$K_3Fe(CN)_6$	329.24	$\geq$ 99.0%	Merck
1,1'-ferrocene dimethanol	$C_{12}H_{14}FeO_2$	246.08	97 %	Merck
Ferrocene methanol	$C_{11}H_{10}FeO$	216.06	97 %	Merck
Hexaammineruthenium(III) chloride	$Ru(NH_3)_6Cl_3$	309.61	98 %	Merck
Electrolytes and Buffer				
2,2-bis(hydroxymethyl)-2,2',2''-nitrotriethanol	$C_8H_{19}NO_5$	209.24	98 %	Acros
Sodium Chloride	$NaCl$	58.44	100 %	Prolabo

Continued on next page· · ·

Table 2.1 – Continued from previous page

Chemical Name	**Molecular formula**	**Molecular Mass ($g\,mol^{-1}$)**	**Purity**	**Supplier**
Potassium Chloride	KCl	74.55	100 %	Prolabo
Lithium Chloride	$LiCl$	42.39	99 %	Fluka
Sodium Nitrate	$NaNO_3$	84.99	99.5 %	Prolabo
Sodium dihydrogen phosphate	NaH_2PO_4	119.98	$\geq$ 99.0 %	Prolabo
Di-sodium hydrogen phosphate	Na_2HPO_4	141.96	$\geq$ 99.0 %	Fluka
Phosphate buffer Tablet pH 7.4	PBS	329.27	$\geq$ 99.0 %	Merck
Huisgen Cycloaddition Reaction				
Sodium azide	NaN_3	65.01	99 %	Merck
(3-chloropropyl)trimethoxysilane	$C_9H_{21}ClO_3Si$	240.80	$\geq$ 95 %	Merck
Tetrabutylammonium bromide	$BrC_{16}H_{36}N$	322.37	pure	Fluka
Copper Acetate	$C_4H_6CuO_4.H_2O$	199.65	100 %	UCB
Ethnyl ferrocene	$C_{12}H_{10}Fe$	210.05	97 %	Aldrich
Ascorbic acid	$C_6H_8O_6$	176.12	99.7 %	Merck
Sodium diethyldithiocarbamate trihydrate	$C_5H_{10}NNaS_2.3H_2O$	225.31	ACS reagent	Merck
Acetonitrile	C_2H_3N	41.05	99.9 %	Merck
Microelectrode Fabrication				
Carbon fibre	C	12	N/A	Goodfellow
Gold Wire	Au	196.97	99.99 %	ChemPur GmbH
Nitric Acid	HNO_3	63.01	65 %	Merck
Indium (III) Nitrate	$In(NO_3)_3$	300.83	99.99 %	Alfa Aesar

Continued on next page· · ·

Table 2.1 – Continued from previous page

Chemical Name	**Molecular formula**	**Molecular Mass ($g\,mol^{-1}$)**	**Purity**	**Supplier**
Tin (II) chloride	$SnCl_2$	189.62	98 %	Prolabo
Acetylacetone	$C_5H_8O_2$	100.12	99 %	Merck
Hydrogen peroxide	H_2O_2	34.01	30 %	Merck
Tetramethylammonium hydroxide	$C_4H_{13}NO$	91.15	25 %	Merck
Sodium hydroxide	$NaOH$	39.99	1 M	Prolabo
Analytes				
L - Cysteine	$C_3H_6NO_2S$	121.16	$\geq$ 97 %	Merck
L - Glutathione (Reduced)	$C_{10}H_{17}N_3O_6S$	307.32	$\geq$ 98 %	Acros
L-Methionine	$C_5H_{11}NO_2S$	149.21	$\geq$ 98 %	Merck
DL-Homocysteine	$C_4H_9NO_2S$	135.18	$\geq$ 95 %	Merck

The reagents for mesoporous silica deposition were used for the electrochemically assisted self-assembly (EASA) on $Indium - doped\ Tin\ Oxide$ (ITO) plates (surface resistivity 8- 12 Ω cm, *Delta Technologies*).
The various redox probes and analytes were used in aqueous medium in the experiments (unless otherwise specified).

2.2 Electrochemical Setup and apparatus

2.2.1 Potentiostats

A potentiostat is electronic hardware which can control and measure the potential and/or current at electrodes in an electrochemical cell. In an electrochemical reaction in a cell, a potentiostat generally acts as the power source to create the potential difference between the electrodes and measures the current generated as the output.
In our experiments, EASA and cyclic voltammetry experiments were carried out on a PGSTAT 100 potentiostat (Autolab, Netherlands). Chronoamperometry performed in the flow cell was measured using a PGSTAT 302N potentiostat (Autolab, Netherlands).

FIGURE 2.1: Picture of the PGSTAT 302N potentiostat

2.2.2 3-electrode electrochemical cell

A 3-electrode electrochemical cell was set-up according to the schematic given in figure 2.2. The working electrode is placed at the bottom part of the cell and is directly in contact with the electrolyte. The working electrode is properly bound under the set up, which is tightened using screws. The surface area of the exposed working electrode is 0.188 cm^2. The reference electrode and counter electrode are both inserted in the electrolyte medium as depicted in the schematic. This 3-electrode setup is used for all of the electrochemical experiments in chapter 3 and

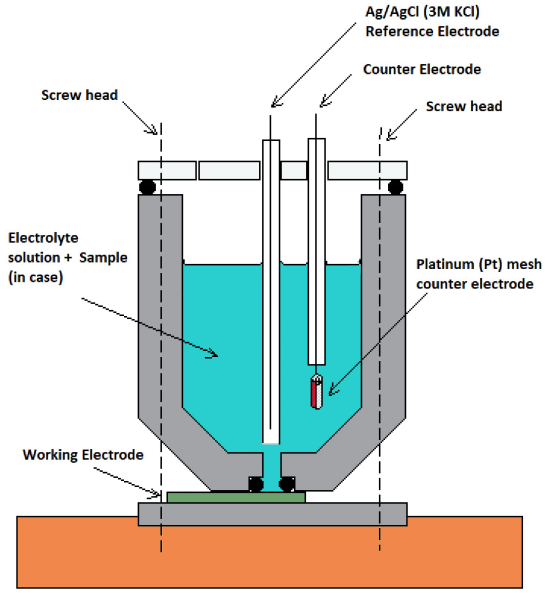

FIGURE 2.2: Schematic of the 3-electrode cell used

chapter 4 involving cyclic voltammetry and chrono methods (unless otherwise stated).

Working Electrode The working electrode is the electrode on which the chemical reaction of interest takes place. This working electrode may consist of a variety of materials ranging from metals like, gold, silver, platinum, etc. to carbon based materials or different composite materials. The working electrode varies from one experiment to other and effects the surface reactions, or can provide a different potential window for the experiment. The working electrode is chosen carefully according to the experimental requirements. It needs to be very clean with a well defined surface area (useful for analysis of the results). Working electrodes like glassy carbon, platinum, gold, etc. can also be polished through various mechanical methods to prepare for experiments.

For our experiments in Chapter 3, we have chosen Indium tin oxide plates (surface resistivity 8- 12 $\Omega\,cm^2$, *Delta Technologies*) as the working electrode. In Chapter 4, we choose the ITO deposited with mesoporous silica thin film as working electrode. In Chapter **??**, we have fabricated and used microelectrodes of carbon and ITO as working electrodes.

Reference electrode A Reference electrode has a stable and well known potential and is commonly used in an electrochemical setup to allow a control over

the potential of the working electrode. The composition of a reference electrode (RE) must remain constant over a long time duration [201]. An ideal reference electrode undergoes a completely reversible cycle following Nernst equation.

The reference electrodes used in the experiments in this thesis are Ag/AgCl in 3 M KCl and Ag/AgCl in 1 M KCl. During the silica electro-deposition step, a silver wire (pure) is used as a pseudo reference.

$$AgCl + e^{-} \rightleftharpoons Ag + Cl^{-} \tag{2.1}$$

The potential of the reference electrode remains constant depending upon the ability of the electrode to keep the chloride concentration constant at all times during the experiment. Potassium chloride is commonly used for the inner electrolyte solution of the reference electrode because it does not generally interfere with the pH, and the mobility of the potassium and chloride ions is nearly equal. Thus, it minimizes liquid-junction potentials [202]. The saturated potassium chloride is commonly used, but lower concentrations such as 1 M potassium chloride can also be used. When the electrode is placed in a different potassium chloride solution, it develops a different potential vs. the standard hydrogen electrode.

3 M KCl, E° = 0.210 V vs. SHE
1 M KCl, E° = 0.205 V vs. SHE

All potentials mentioned at any figure or text in this thesis are in reference to Ag/AgCl reference electrode in 3 M KCl solution (unless mentioned otherwise).

Counter Electrode The counter electrode (or auxiliary electrode) is used to complete the circuit for the electrochemical cell so that the current can flow through the working electrode. The current is recorded between working electrode and counter electrode as the number of electrons flowing through them. The material of counter electrode is generally chosen as a highly conductive and non-interfering material with a large surface area to allow a good and steady current flow. The possibility to pass high amount of current through the counter electrode allows us to make sure that the kinetics of the reaction occurring at the working electrode are not inhibited by the counter electrode.

The counter electrode used for most of the experiments in this thesis is a mesh of pure platinum attached to the end of a platinum wire (unless otherwise stated).
In experiments involving deposition of silica, a larger mesh made of stainless steel is used as the counter electrode to provide a large surface area.

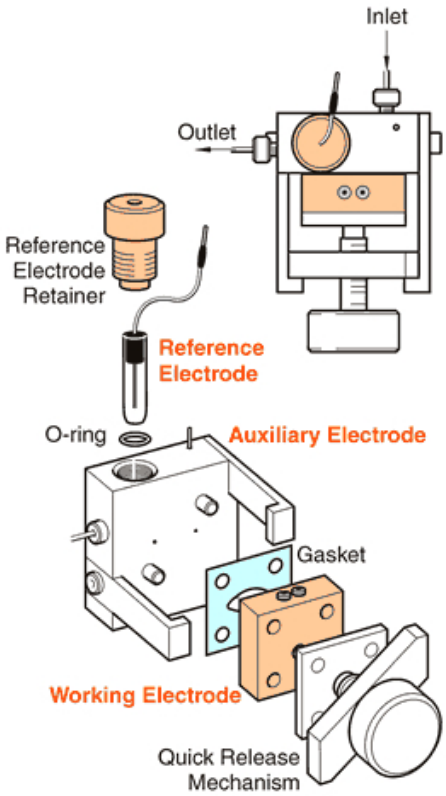

FIGURE 2.3: Schematic of the Flow cell which is used for flow injection electrochemical detection experiments. The figure is reproduced from the official BASI® website[†]

2.2.3 Flow injection setup

The flow injection setup was purchased from BASi®[*]. The schematic of the cell is given in figure 2.3 and the flow injection setup is given in figure 2.4.
This flow cell allowed flow of a solution over the electrode and a possibility to inject another solution in the loop by switching the path of the solution flow (figure 2.4). This type of system has been shown earlier to improve the sensitivity of the system for electro-analytical applications [203–207].
The geometrical area of the exposed electrode was measured as 0.407 cm^2 and the volume of the solution in the cell at the electrode surface is 0.022 mL flowing at the rate of 1 mL min^{-1}. The volume of analyte injections is 150 µL.

2.2.4 Redox Probes

Different types of commonly used redox probes like hexaammine ruthenium(III), ferrocene dimethanol, ferrocene methanol, potassium hexacyanoferrate(III), etc. were

[*] https://www.basinc.com/products/ec/flowcells
[†] https://www.basinc.com/assets/img/products/ec/flow3.gif

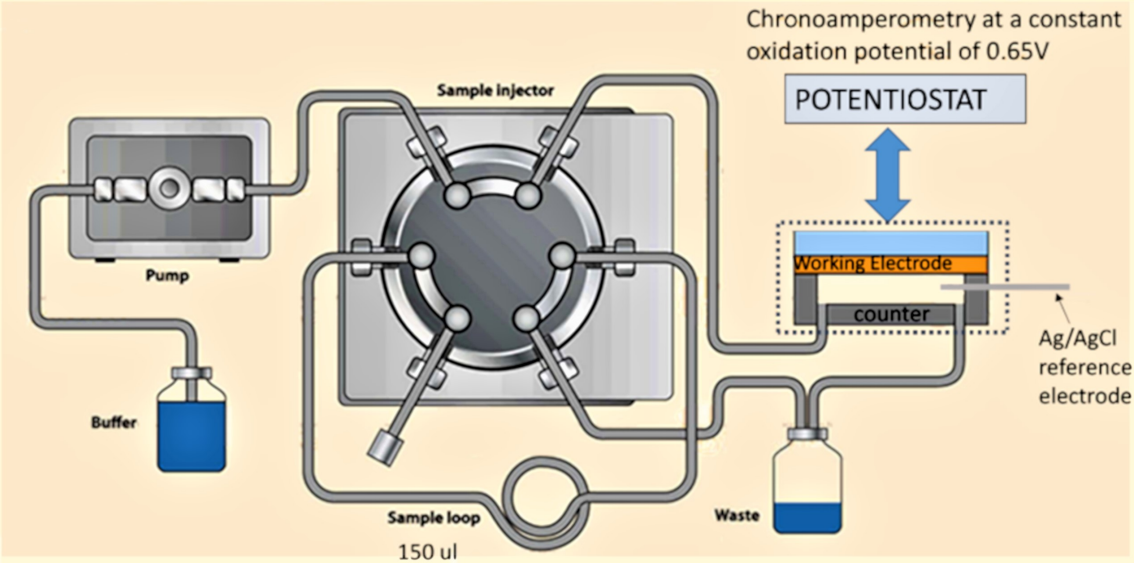

FIGURE 2.4: Schematic of the Flow cell setup for flow injection electrochemical detection experiments

used for the various experiments. These redox probes (or redox couples) are generally very stable molecules, have been intensively studied and exhibit a known reversible electrochemical behaviour. They exhibit a known standard electrode potential (E^0) which is easily defined by Nernst equation (equation 2.2).

For a reversible species given by,

$$A + e^- \rightleftharpoons B$$

the nernst equation is defined as,

$$E = E^0 + \frac{RT}{nF} \ln \frac{[A]}{[B]} \tag{2.2}$$

2.3 Characterization techniques

2.3.1 Microscopy techniques

In the microscopy experiments covered in this thesis, two broad types of microscopy techniques have been used namely optical microscopy and electron microscopy. For the scope of this thesis, we have limited ourselves to a simple compound optical microscope and 2 subtypes of electron microscopy namely scanning electron microscopy (SEM) and transmission electron microscopy (TEM) (explained in section 2.3.1.2).

The TEM used is a "Philips CM20" microscope at an acceleration voltage of 200 kV. The SEM is a "Jeol JSM-IT500HR" with an accelerating voltage of 25 kV. The optical microscope was purchased from Nikon, Japan and had a magnification from 5x - 100x.

2.3.1.1 Optical Microscopy

The optical microscope is a type of microscope that uses visible light and a combination of lenses to generate magnified images of small objects. Optical microscopes are very common in fields of research, medicine, electronic manufacturing, etc. and have been used since a long time for magnification of objects.

In a typical set-up, the object is placed on a stage and is viewed through one or two eyepieces on the microscope. This image from the optical microscope can be captured by a camera to generate a *micrograph*. Originally, photographic films were used, but they are now replaced with Complementary metal-oxide-semiconductor (CMOS) or charge-coupled device (CCD) cameras. Purely, digital microscopes are also available now which don't require eye-pieces but directly show digital image on a screen.

In an optical microscope , there are a variety of ways to light the sample. It is possible to light objects from both below or above, which is useful for lighting transparent objects. Solid objects can be lit with light coming through (bright field) or around the objective lens (dark field). Crystal orientation can sometimes be observed using polarized light sources [208]. Different magnification can be achieved using various optical lenses which are generally located on a movable turret so as to interchange the lenses for the required magnification. Since, the resolving power for the visible light is limited (due to high wavelength) the maximum magnification power of optical microscopes is typically limited to around 1000x. The presence of two lens system in a compound microscope provides a magnification which is the product of magnification of the eyepiece and the objective lens. It is also a common practice to use oil on the optical lens to improve the magnification.

2.3.1.2 Electron Microscopy

Electron microscopy is a highly valued tool which is used to obtain high-resolution images for a large variety of applications, including materials sciences, biomedical research, etc. In contrast to optical microscopes, electron microscopes are able

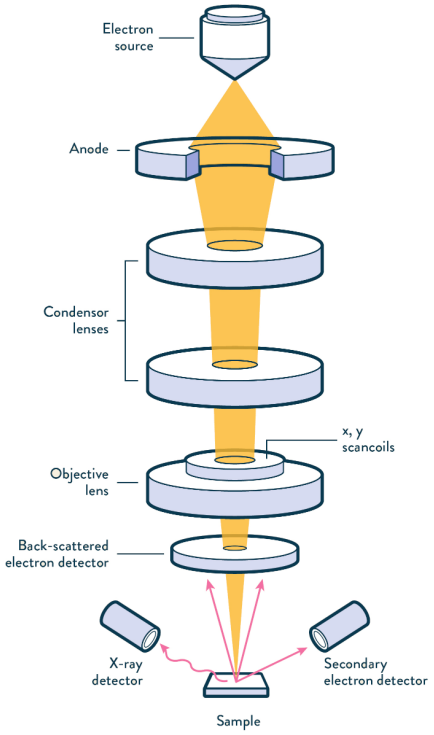

FIGURE 2.5: Schematic of a Scanning Electron Microscope [209]

to capture images at much higher resolution. Since, the source in an electron microscope is focused electron beam, which has a much lower wavelength, we are able to micrograph an object to much higher magnification in comparison to an optical microscope.

Scanning Electron Microscopy A scanning electron microscope (SEM) is one of the widely used electron microscope. In this type of electron microscope, images of a sample are produced by scanning of the surface using a focused beam of electrons (a schematic is given in Figure 2.5). The resulting interaction between these electrons and the sample produces various signals that can be detected using a variety of detectors. This signal reveals information about the sample including the surface topography, chemical composition of the sample, crystalline structure and orientation of the materials. The electron beam is scanned in a raster scan pattern over an area which can approximately range from 1 cm to 5 µm, and the position of the beam is used along with the intensity of the detected signal to produce a 2-dimensional image that displays the spatial variations in the result. Various signals are produced in SEM like secondary electrons, backscattered electrons, diffracted backscattered electrons, photons, visible light, and heat. The different detection modes commonly used are Secondary electrons (emitted by atoms excited by the electron beam) which are useful at showing morphology

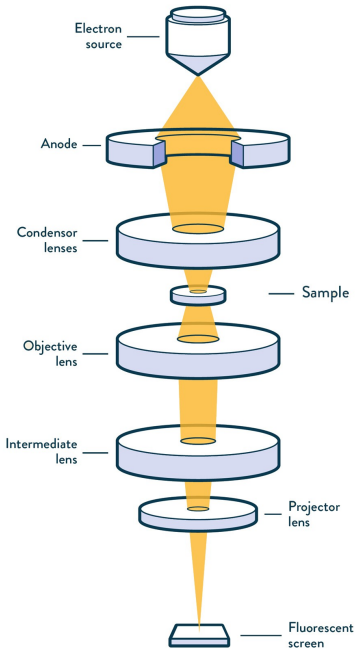

FIGURE 2.6: Schematic of a Transmission Electron Microscope [209]

of a sample, and backscattered electrons (elastic scattering of electrons at sample surface) which are useful for illustrating contrasts in compositions at multiphase samples. SEM can generally achieve resolution between 1 nm to 20 nm depending on the instrument.

Transmission Electron Microscopy Transmission electron microscopy (TEM[‡]) is a type of electron microscopy technique in which a beam of electrons is transmitted through a specimen to form an image (a schematic is given in Figure 2.6). The specimen is most often an ultrathin section less than 100 nm thick or a suspension on a grid. An image is formed from the interaction of the electrons with the sample as the beam is transmitted through the specimen. The image is then magnified and focused onto an imaging device, such as a fluorescent screen, a layer of photographic film, or a sensor such as a scintillator attached to a charge-coupled device.

Transmission electron microscopes are capable of imaging at a significantly higher resolution than light microscopes, owing to the smaller *de Broglie* wavelength of electrons. This enables the instrument to capture fine detail—even as small as a single column of atoms, which is thousands of times smaller than a resolvable

[‡]It can also stand for the instrument, a transmission electron microscope

object seen in a light microscope. Transmission electron microscopy is a major analytical method in the physical, chemical and biological sciences. TEMs find application in cancer research, virology, and materials science as well as pollution, nanotechnology and semiconductor research, but also in other fields such as paleontology and palynology.

2.3.2 Spectroscopy techniques

2.3.2.1 Grazing-Incidence Small-Angle X-ray Scattering (GISAXS)

The GISAXS method was introduced by Joanna Levine and Jerry Cohen in 1989 [210]. This method has been very useful to study the surface of nanosized thin films and is commonly used as a scattering technique. It is commonly used for characterization of mesoporous thin films, metal deposits on oxide surfaces, surface-deposited nanoparticles, and soft matter systems (polymer/block copolymer thin films and surface-attached biological materials) [211] [212]. With GISAXS techniques it is possible to analyze density correlations and the shape of a surface deposited nanostructured objects (figure 2.7) or adjacently buried interfaces. The GISAXS method can be regarded as a technique which combines together the features of a small-angle X-ray scattering technique and diffuse X-ray reflectivity.

The scattering angles at a GISAXS is very small (typically up to 5°). Grazing-incidence wide-angle X-ray scattering (GIWAXS) is available for wide scattering angles measurements. It uses the same basic principles of analysis and evaluation as GISAXS. Grazing-incidence X-ray diffraction (GIXD) is another similar technique to GISAXS which can characterize thin-film structures with crystalline features. In this technique, the Bragg reflections are analysed at much higher scattering angles.

GISAXS experiments were carried out on "SAXSess mc^2" instrument (Anton Paar) with GISAXS equiped "VarioStageXY". This instrument is attached to a ID 3003 laboratory X-ray generator (General Electric) equipped with a sealed X-ray tube (PANalytical, λ Cu, $K\alpha = 0.1542\,\text{nm}$) operating at 40 kV and 50 mA[§]. Scattering of X-ray beam was registered by a CCD detector (Princeton Instruments, 2084×2084 pixels array with $24 \times 24\,\mu\text{m}^2$ pixel size) at 299 mm distance from the sample.
Using Winspec32 software (Princeton Instruments), the 2D image was integrated into one-dimensional scattering intensities $I(q)$ as a function of the magnitude of

[§]M. Lionel Richaudeau is thanked for his help with the GISAXS measurements.

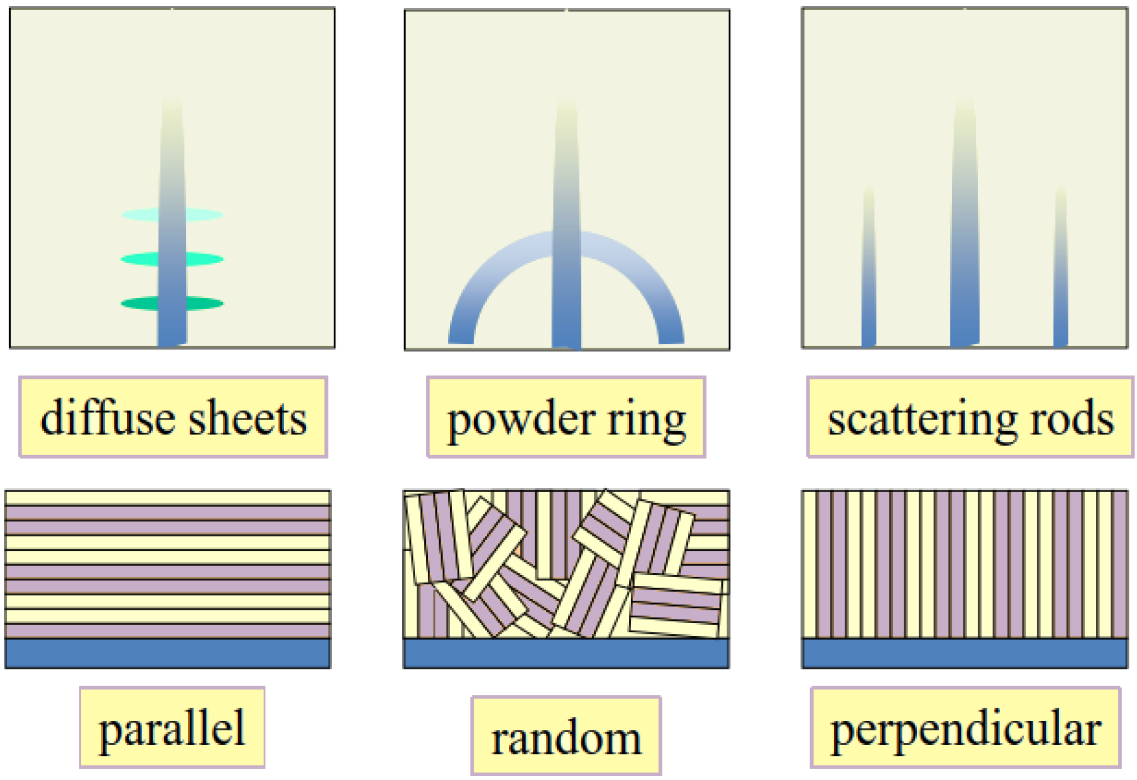

FIGURE 2.7: GISAXS signatures of parallel, random, and perpendicular lamellae [211]

FIGURE 2.8: The picture of the GiSAXS instument used

the scattering vector q_z which is defined by,

$$q_z = \frac{4\pi}{\lambda} \cdot \sin\theta \tag{2.3}$$

From Bragg's law, we obtain the equation 2.4 [213].

$$\lambda = 2d \cdot \sin\theta \tag{2.4}$$

Now, substituting this equation 2.4 in equation 2.3, we get

$$q_z = \frac{4\pi}{2d \cdot \sin\theta} \cdot \sin\theta$$
$$\therefore \quad q_z = \frac{4\pi}{2d}$$

which gives us,

$$d = \frac{2\pi}{q_z} \tag{2.5}$$

here θ is the specular reflectance angle. A picture of the working instrument can be seen in figure 2.8.

2.3.2.2 Infrared Spectroscopy

Infrared spectroscopy deals with infrared region of the electromagnetic spectrum. Photon energies associated with the infrared range (from 1700 meV to 1.24 meV) are not powerful enough to excite the electrons within the atoms, but can cause vibrational or rotational changes in the bonds of covalently bonded atoms and groups. The covalent bonds in molecules are not rigid sticks or rods but can be

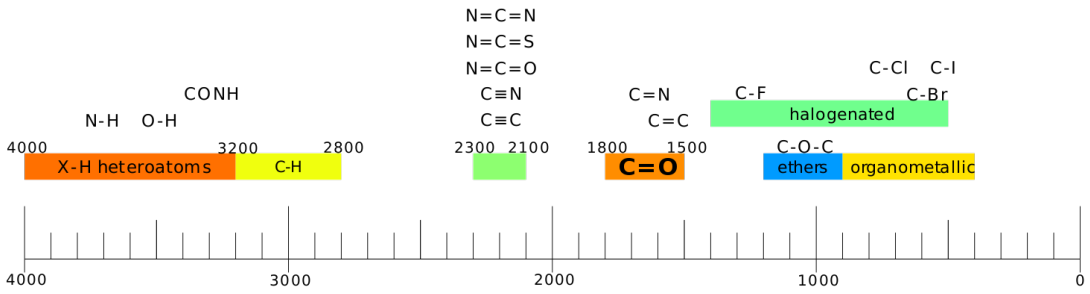

FIGURE 2.9: List of main IR spectroscopy bands. Wavenumbers listed in cm^{-1} (reproduced from wikimedia.org[¶])

stretched, bent, rotated, vibrated, etc. Molecules and compounds absorb infrared radiation corresponding to the energies of these bond changes and are specific to the component atoms [214]. This allows researchers to obtain an absorption or emission spectra of the infrared data and associate it with the molecular structure of a material. Infrared Spectroscopy has been done on a Nicolet 8700 apparatus equipped with a diffuse reflectance accessory (Smart Collector).

2.4 Electrode Preparation

The mesoporous silica films were prepared by electrochemically assisted self-assembly method according to the procedure described in figure 2.10 [160]. The sol is prepared using a silica precursor such as TEOS, along with a CTAB as a surfactant. Since, CTAB contains a polar head and a long organic tail, and the concentration is higher than the critical micelle concentration (0.9 mM for aqueous solutions [215]), it forms a micelle structure in aqueous medium meanwhile forming covalent bonds with TEOS at the polar ends. The application of a reductive potential at the working electrode induces the arrangement of cationic surfactant in hemispherical micelle around which silica is formed. The condensation of the silica was then favoured by the rise of pH in the vicinity of the electrode due to the reduction of protons and water at the electrode surface. Once the electrochemical reaction was over, the films were removed promptly from the solution and rinsed thoroughly with water in order to stop the condensation reaction that continues even when the reductive potential is not applied anymore.

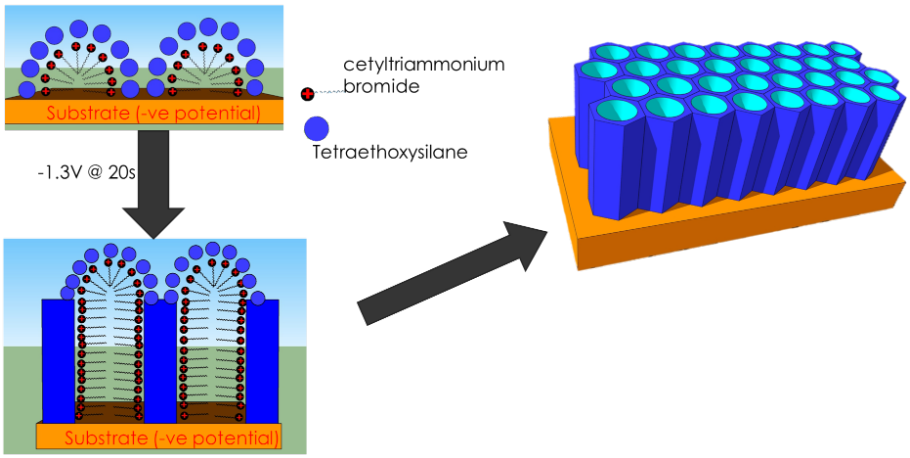

FIGURE 2.10: Schematic representation of the electrochemically assisted self assembly of mesoporous silica on an electrode

¶https://commons.wikimedia.org/wiki/File:IR-spectroscopy-sample.svg

2.4.1 Electrodeposition mechanism of silica thin films

The electrodeposition of silica thin film is done using a PGSTAT100 or a PGSTAT302N potentiostat (Autolab, Netherlands). The process is defined as follows:

1. A sol was prepared with 100 - 200 mM TEOS, 32 - 64 mM CTAB (the ratio [CTAB]:[TEOS] has been kept constant at 0.32) with 0.1 M $NaNO_3$ as electrolyte in a solvent mixture of ethanol and water in a 1: 1 v/v ratio. The sol is not stored, and freshly prepared at requirement.
2. The pH of the sol was adjusted to 3 by addition of ∼40 µL of 1 M HCl.
3. The sol was left to hydrolyse for 2.5 h before the electro-deposition process.
4. A potential of −1.3 V was applied for 20 s (using an ITO plate as working electrode, a silver wire as a pseudo-reference electrode and a stainless steel mesh as a counter electrode).
5. After the film formation, the electrodes were kept at 130 °C for 16 h to ensure good cross-linking of the silica network.
6. Surfactant template was removed by immersion of the electrode in 0.1 M HCl (in ethanol) for 15 minutes.

For electro-deposition of silica thin films with azide terminating groups, AzPTES is used along with TEOS in ratios of [AzPTES]:[TEOS] ranging from 0.10 - 0.40 [165]. Apart from this, the rest of the procedure remains same.
Mesoporous silica films were further characterized by electrochemistry, grazing-incidence small-angle scattering (GISAXS), and transmission electron microscopy (TEM) as described later in section 4.2.

2.4.2 Co-condensation of TEOS with AzPTES[||] for deposition of modified MSTF with azide functional groups

2.4.2.1 Synthesis of AzPTES molecule

The synthesis of AzPTES was done according to previously reported procedure [165]. We verified the nature of the obtained product by characterization with nuclear magnetic resonance ($H^1 - NMR$) spectroscopy (figure 2.11).
δ_H= 0.61 (t, 2H, $-SiCH_2$-), 1.17 (d,9H, $-SiCH_2CH_3$), 1.64 (m, 2H, $-CCH_2C-$), 3.20 (t, 2H, $N_3CH_2CH_2$), 3.76 (q, 6H, $-SiCH_2CH_3$) ppm.

[||] 3 − azidopropyltriethoxysilane

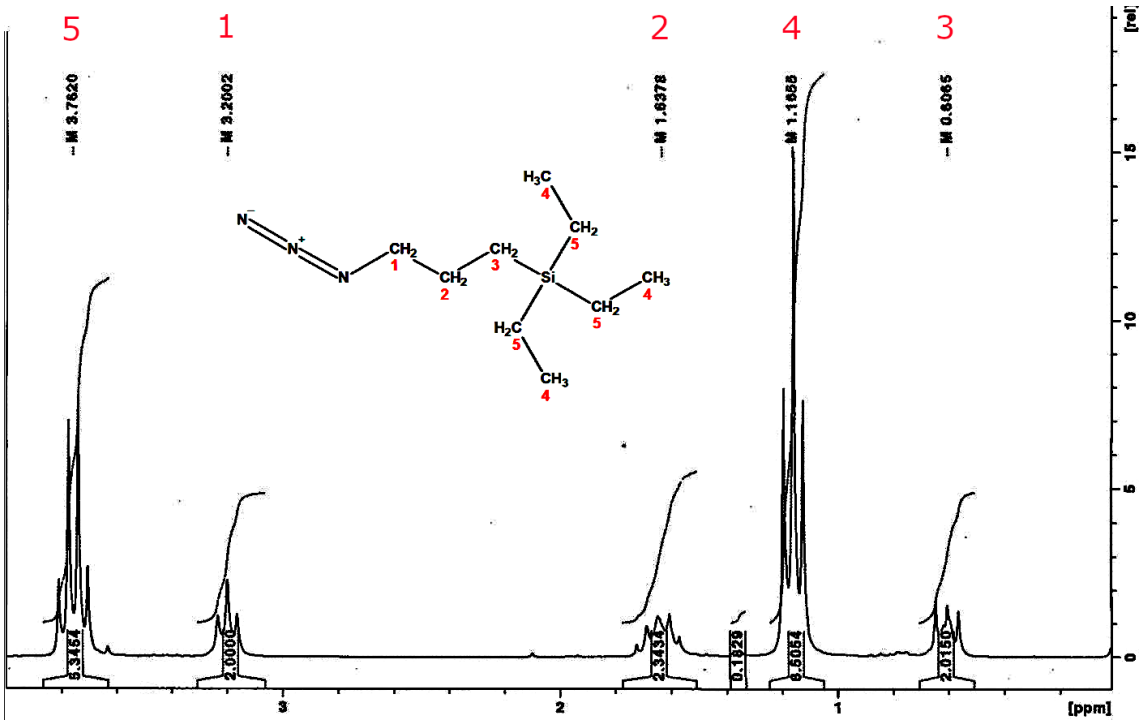

FIGURE 2.11: NMR spectra of the $3-$azidopropyltriethoxysilane molecule. Numbers in red represent the designation of the peaks in the structure

The protocol of preparation can be divided into few steps:

1. 50 mL of acetonitrile was placed in round bottom flask. N_2 is passed through the solvent for 10 min.
2. After 10 min, 1.08 g (16.6 mM) of sodium azide (NaN_3), 0.644 g (2 mM) of tetrabutylammonium bromide (TBA^+Br^-) and 2 g (8.3 mM) of $3-$chloropropyltriethoxysilane were add to the solvent inside the round bottom flaks while stirring vigorously.
3. Reaction mixture was then stirred at 80 °C for 18 h under reflux.
4. After this time, the solvent was removed with a rotary evaporator (figure 2.12). The resulting mixture was diluted in cyclohexane and filtered under gravity with a paper filter.
5. Cyclohexane was removed under reduced pressure with rotary evaporator. Azido functionalized silica precursor was collected and analyzed with NMR (Figure 2.11).

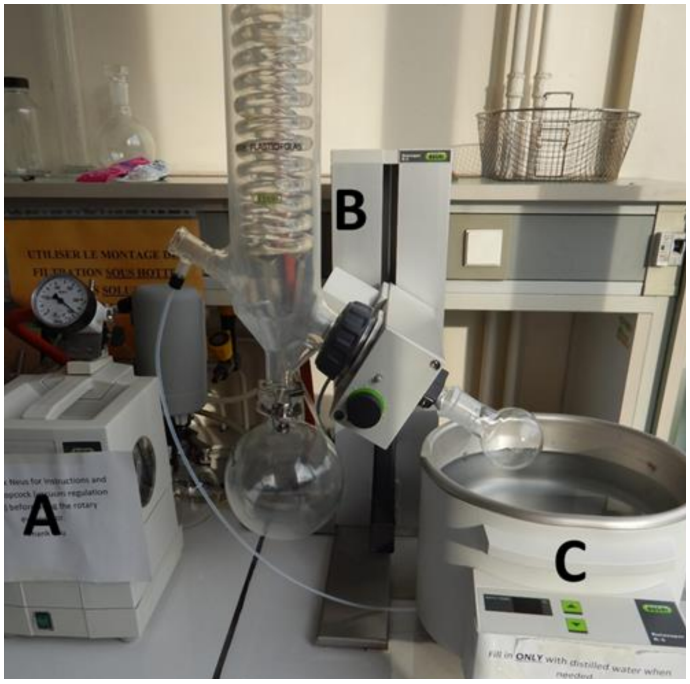

FIGURE 2.12: Image of a rotary evaporator

2.4.3 Functionalization of azide modified mesoporous silica thin films with ferrocene

Functionalization of silica thin films with ferrocene is done using silica thin films co-deposited with AzPTES. This allows us to click the azide groups with an ethynyl-group bearing compound like ethynyl ferrocene, ethynyl cobaltocene, etc. via *azide-alkyne Huisgen cycloaddition reaction* [216]. For the scope of this thesis, we have limited ourselves to ethnyl ferrocene.

1. Silica films are deposited on an ITO substrate with a sol prepared with [TEOS]=140 mM and [AzPTES]=60 mM keeping the concentration of CTAB as 64 mM (ratio of 0.32 for the overall silica concentration).

2. The CTAB template at these films is extracted in 0.1 M HCl in EtOH for 15 min.

3. The electrode is then kept in a solution of 2.38 mM ethynyl ferrocene (10 mg) with 0.83 mM of copper acetate (3 mg) (catalyst) in 60% DMF and 40% H_2O (total volume used is 20 mL) for 18 h. In order to reduce the Cu(II) into Cu(I), we use 2.13 mM of ascorbic acid (7.5 mg) in the solution as well.

4. The electrodes are then thoroughly rinsed with water, ethanol and acetonitrile (10 min in each solvent) to remove unreacted species.

5. The films were then kept in 50 mM sodium diethyldithiocarbamate solution in ethanol for 30 min to remove any traces of copper(which was used as the catalyst).

6. The films are subsequently left for 30 min in the dark for drying.

2.4.3.1 Infrared Spectroscopy to follow the click reaction

Infrared spectroscopy was done using a Nicolet 8700 apparatus equipped with a diffuse reflectance accessory (Smart Collector). It was used to characterise the mesoporous silica films at the different stages of the functionalization procedure (Figure 2.13). After co-condensation of the azide silane with TEOS, a strong band at 2095 cm^{-1} attributed to the azide group is visible. This band remained present after extraction of the template but was greatly reduced after the click chemistry reaction. The efficient removal of the template was also verified by the strong decrease of the CH_2 and CH_3 stretching around 2900 cm^{-1} after template extraction.

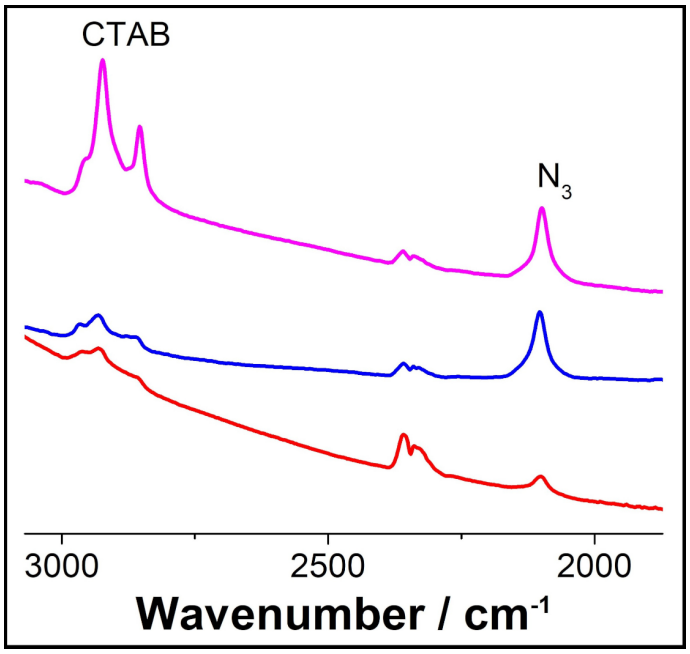

FIGURE 2.13: Infrared spectroscopy of the mesoporous silica thin film after electrochemically assisted self-assembly of the azide silane and TEOS (pink curve) after template extraction (blue curve) and covalent immobilisation of the ferrocene groups (red curve).

Chapter 3

Thiol oxidation at a Bare Indium tin oxide (ITO) Electrode

Chapter Plan

3.1 Introduction

3.1.1 Analytes – Thiol groups

Thiol molecules, such as cysteine (figure 3.1) and glutathione (figure 3.2), play a very important role as antioxidants in physiological fluids. The 4 major types of sulphur containing compounds of biological relevance are given as following:

3.1.1.1 Cysteine

Cysteine is a sulphur-containing α-amino acid (figure 3.1) and is one of the 20 amino acids commonly found in natural proteins. It is categorized as a semi-essential amino acid and is of analytical interest as it plays a very important role in living systems due to its role in the antioxidant sequence in a living cell [217, 218]. It is one of the two amino acids which contain a thiol group (other than homocysteine) and is a precursor to the synthesis of glutathione. Cysteine concentration in whole blood is generally in the sub-millimolar range [219]. As its concentration variation has been correlated with a variety of disease, the monitoring of cysteine in physiological fluids could be used as a diagnostic of the evolution of several pathologies and clinical conditions [220–225]. High levels of these thiols (cysteine and glutathione) in blood have been associated to cancer or diabetes [221, 224, 225], while high thiol concentrations were also observed in patients suffering from Alzheimer and Parkinson disease [220, 222].

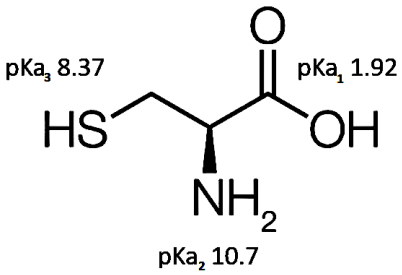

FIGURE 3.1: Structure of the amino acid – Cysteine and its pKa values

The couple L-cysteine/L-cystine (the oxidized form or $[\mathrm{R}-(\mathrm{R}*,\mathrm{R}*)]-3,3'-\mathrm{dithiobis}(2-\mathrm{aminopropanoic\ acid})$) is also generally used as a model to understand disulphide bond and chemistry of thiols (independent and in proteins), and their role in living systems and biological media. Several studies have previously been reported on various electrodes like $\mathrm{mercury}$ [226–230], $\mathrm{platinum}$ [231–233], gold [232, 234], carbon [234, 235], $\mathrm{boron}-\mathrm{doped\ diamond}$ [228].

3.1.1.2 Glutathione

Glutathione is a tripeptide (L-γ-glutamyl $-$ L $-$ cysteinyl $-$ glycine, GSH) with an amide bond between the amine group of a cysteine residue and the side-chain γ-carboxylic group of glutamic acid (figure 3.2). It is one of the most abundant peptides in mammalian and plant cells with cellular concentrations as high as 10 mM and accounting for close to 90% of the total nonprotein sulfur present in the organism [236–238]. Glutathione plays vital role in living organisms by functioning as an antioxidant against reactive oxygen species with the help of the active thiol group in the cysteine residue [239]. Under oxidative stress, glutathione can be chemically or enzymatically converted into glutathione disulfide (GSSG). Glutathione can, again, be regenerated from GSSG by the enzyme action of the molecule glutathione reductase [240]. Naturally, glutathione exists in both reduced (GSH) and oxidized (GSSG) states in intercellular media with the thiol-disulfide pair acting as a redox buffer [241]. Solution pH can also modulate the state of charge of biomolecules by shifting the equilibrium between the protonated and deprotonated states of ionizable groups, which, in turn, has been shown to change the half-cell potentials dramatically [242]. The role of an antioxidant to glutathione has been assigned by nature with care. The cysteine residue ensures that the dissociation constant of the thiol group (pKa = 8.66) allows the molecule to participate as part of the GSSG/2GSH redox pair at physiologically neutral pH = 7.

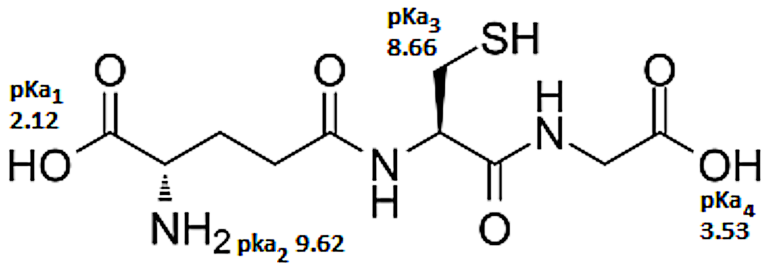

FIGURE 3.2: Structure of the tripeptide – Glutathione and its pKa values

3.1.1.3 Homocysteine

Homocysteine is a sulphur-containing, non-proteinogenic amino acid* which is synthesized from methionine in biological systems. Homocysteine is very similar

*those amino acids that are not naturally encoded or found in the genetic code of any organism

to cysteine differing only by an additional methyl group in the side chain (figure 3.3). It is mainly present in body in disulphide-bound form with plasma proteins (mainly albumin), and forms dimer with another homocysteine molecule or with other thiols, while only about 1% of the total homocysteine in the body circulates as free thiol [243]. In an organism, homocysteine either gets re-methylated to methionine, enters cysteine biosynthetic pathway or is released into the extracellular medium (causing increase of concentration in extracellular fluids like urine and plasma).
Hyperhomocysteinemia is a disease resulting from high level of homocysteine in the blood and is linked to increased risk of cardiovascular disease, atherosclerosis and thrombosis [243–245].

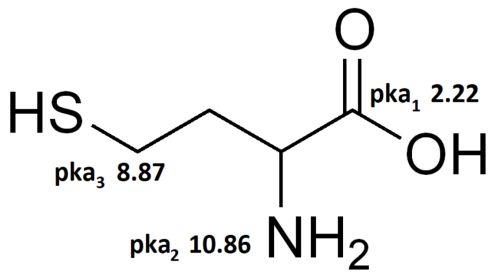

FIGURE 3.3: Structure of the amino acid – Homocysteine and its pKa values

3.1.1.4 Methionine

Methionine is one of the nine essential amino acids in humans and is primarily obtained from dietary sources. It is not an aminothiol but it is the primary source of sulphur in human diet and is the precursor to different important aminothiols like homocysteine, cysteine, glutathione, and other sulphur containing important molecules like taurine and $S-$ Adenosyl methionine $(SAM-e)$, among major sulphur containing proteins present in the body. It is also involved in regulation of many metabolic processes, immunological processes, and antioxidant capacity of organisms. Being an important molecule, its deficiency causes a range of proven health problems ranging from nucleic acid damage to different types of cancer, cardiovascular and neurodegenerative diseases [246–252].

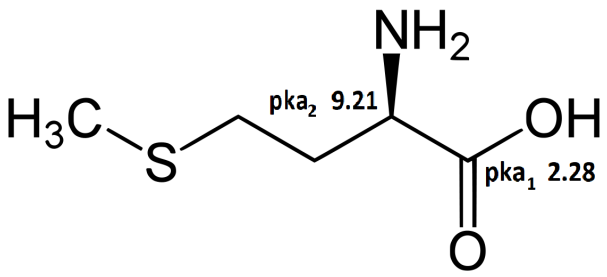

FIGURE 3.4: Structure of the amino acid – Methionine and its pKa values

Thiol Group	Molecular weight ($g\,mol^{-1}$)	Molecular formula	pKa_1	pKa_2	pKa_3	pKa_4	pI[a]
Cysteine	121.16	$C_3H_7NO_2S$	1.92	10.7	8.37	–	5.14
Homocysteine	135.18	$C_4H_9NO_2S$	2.22	10.86	8.87	–	5.54
Methionine	149.21	$C_5H_{11}NO_2S$	2.28	9.21	–	–	5.74
Glutathione	307.31	$C_{10}H_{17}N_3O_6S$	2.12	9.62	8.66	3.53	2.82

TABLE 3.1: Common thiol groups in natural proteins [253]

[a] isoelectric point: the pH at which the molecule has a net neutral charge

3.1.2 Oxidation of Thiols

3.1.2.1 Direct oxidation of Cysteine at bare ITO Electrode

Many attempts to determine the standard electrode potential of cysteine have been reported in the past. Through different processes like thermal data, potentiometric measurements at mercury electrode or equilibrium constant calculation for reaction of RSH/RSSR [†] couple with other redox couples, different groups have reported values varying from $-0.595\,\mathrm{V}$ to $-0.125\,\mathrm{V}$ vs. Ag/AgCl [254–261]. However, a large overpotential at different electrodes can be seen in experimental conditions. From figure 3.5, it can be seen that an overpotential of more than 1 V can be seen for both bare indium tin oxide (ITO) (figure 3.5a) and bare glassy carbon (figure 3.5b) electrode. Similar results have been reported in earlier studies for platinum and gold electrodes as well [261]. This high overpotential is attributed to poor electron transfer between the cysteine molecule and the bare electrodes.

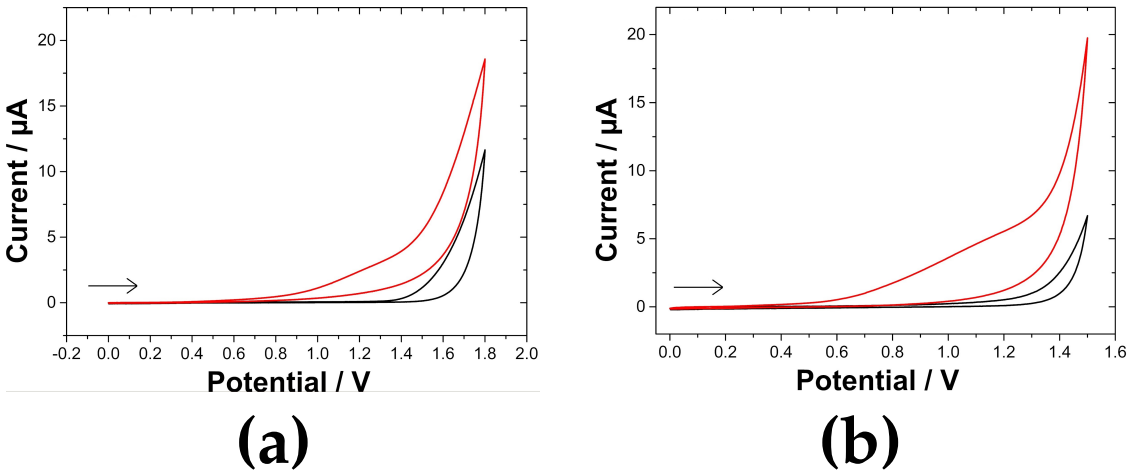

FIGURE 3.5: Cyclic voltammogram at (a) Bare ITO (b) Bare Glassy Carbon electrode with 0 mM (black curve) and 0.5 mM (red curve) cysteine. Electrolyte is 0.1 M Phosphate buffered Saline at pH 6.5; $\nu = 10\,\mathrm{mV\,s^{-1}}$. The black arrow indicate the direction of the first CV scan

Attempt at oxidation of thiols at such high potentials can lead to the oxidation of other molecules present in the solution and to the passivation of the electrode surface by reaction products, which limit the possibility of analytical applications [262]. Boron-doped diamond and FTO electrodes have been used for the direct oxidation of cysteine and thiol compounds at lower overpotentials [228,

[†]RSH : free thiol-substituted molecule; RSSR : coupled molecules with disulphide group

263].However, the use of alkaline or acidic conditions limits their analytical applications in natural systems [228, 263]. In order to improve the oxidation of cysteine at bare electrodes, a lot of research focuses on use of a mediator/catalyst, which consequently allows the decrease of this overpotential. The overpotentials are partially overcome by the addition to the solution of a variety of redox mediators which allow for an easier oxidation of the thiol molecule. Some of these redox mediators include: nitrosophenyl , catechol, quinone, ferrocene derivatives and cyclotricatechylene [264–268]. The electrode surface has also been modified to provide electrocatalytic properties in order to lower the thiol oxidation potential. The various strategies included the immobilisation of redox-active polymers such as Prussian blue, poly(3,4-ethylenedioxythiophene), poly(eugenol), caffeic acid-based polymer [269–273]. Redox mediators were also trapped inside polymer matrix or sol-gel material for electrocatalytic thiol detection [274–276].
The overall electrochemical cysteine oxidation process that leads to the formation of a disulfide bond is described in the reaction 3.1 [261].

$$2CySH \longrightarrow CySSCy + 2H^+ + 2e^- \tag{3.1}$$

As explained earlier, this reaction directly at the common electrodes suffers due to the charge transfer limitations and the presence of a mediator allows for an alternate route for this reaction lowering the energy requirements. Catalytic mechanisms like EC' mechanism have been demonstrated successfully in the past for similar reactions as well [277–279].

3.1.3 EC' Mechanism and kinetic zone diagram

EC' mechanism describes a catalytic reaction following the electrochemical oxidation of a redox probe [280]. In this mechanism, the redox probe (A), for instance, is oxidized at the electrode surface (equation 3.2) and then subsequently transferred an electron to the analyte (P) and is recovered at the electrode surface (equation 3.3) allowing an increase of the oxidation current.

$$A \rightleftharpoons A^+ + e^- \tag{3.2}$$

$$A^+ + P \rightarrow A \ + Q \tag{3.3}$$

Here, the oxidized form of the analyte is represented as Q. The two different parameters concerning the EC' mechanism are given as kinetic factor, λ, and excess factor, γ. The values of the λ and γ can be calculated by the equations 3.4 and 3.5

respectively [280–282].

$$\lambda = \left(\frac{RT}{F}\right)\left(\frac{k_e C_A^0}{\nu}\right) \tag{3.4}$$

$$\gamma = \frac{C_P^0}{C_A^0} \tag{3.5}$$

where,

λ	calculated value	kinetic factor,
γ	experimental condition	ratio of the bulk concentrations of the analyte and the catalyst,
R	$8.314\,\mathrm{J\,mol^{-1}\,K^{-1}}$	molar gas constant,
T	298 K	temperature,
F	$96\,485.33\,\mathrm{C\,mol^{-1}}$	faraday's constant,
k_e	reaction dependent, calculated	rate of transfer of electron between the catalyst and the analyte molecule,
ν	experimental condition	scan rate used for the voltammetry,
C_A°	experimental condition	bulk catalyst concentration,
C_P°	experimental condition	bulk analyte concentration

The EC' mechanism describes the electrochemical reaction for mediated oxidation of the analyte, but depending on different experimental conditions, we can observe change in the shape and the current of the voltammogram. The figure 3.6 shows a typical kinetic zone diagram which is adapted for an EC' mechanism describing different shapes of voltammograms observed for the reaction at different experimental conditions. The various zones in this diagram obtained on varying values of λ and γ are as follows:

- *Zone D (No catalysis)*: The cyclic voltammograms in *zone D* result from only the reversible curve of the redox species (i.e. $\mathrm{Fc(MeOH)_2}$ in our case). No catalysis of the analyte can be observed in this zone. Certain cases where this zone can be accessed include low concentration of the analyte, slow reaction kinetics (k_e) or high scan rate.
- *Zone KG/KG* (Analyte consumption)*: At smaller values of λ and γ, we can observe this zone, which describes the catalysis reaction at the electrode, limited by the diffusion of the analyte at the electrode.
- *Zone K (Pure Kinetic conditions, Analyte consumption)*: λ and γ are large so that a pure kinetic condition is reached while there is a mutual compensation between the analyte consumption and the diffusion of the analyte

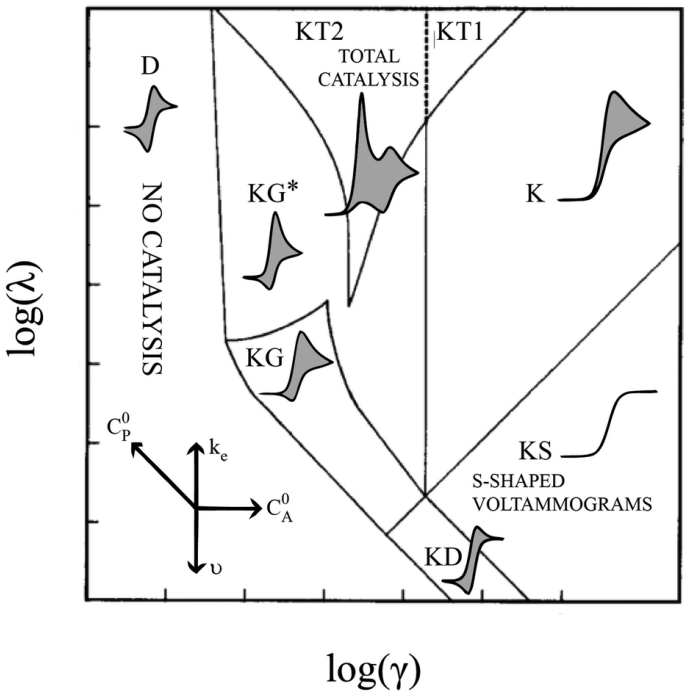

FIGURE 3.6: Schematic of a kinetic zone diagram showing different types of cyclic voltammograms for different values of excess ratio (γ) and kinetic factor (λ). Reprinted with permission from [281]. Copyright © 2014 American Chemical Society.

species from bulk. The consumption of analyte is controlled by the rate-determining step of the reactions.

- *Zone KS (Pure kinetic conditions, No apparent analyte consumption, Sigmoidal-shaped curve)*: This zone describes the particular case of Zone *K* in which the ratio γ/λ is so large that the concentration of the analyte at the electrode substrate is equal to the bulk concentration. In the reaction conditions leading to this zone, there is no apparent analyte depletion at the electrode surface and we are not limited by the diffusion of the molecular species. We observe a steady state electrochemical behaviour in this zone, which makes it simpler to be used for calculation of the reaction kinetics for the system (explained further in section 3.4).

- *Zone KD (No analyte consumption)*: The cyclic voltammograms in this zone is similar to zone *KS* as it is also under the conditions of no apparent analyte consumption, but with a lower value of λ. This zone is accessed at higher scan rate or with catalysts having slower rate constants.

- *Zone KT (Pure kinetic condition, total catalysis of analyte)*: In zone *KT*, a splitting of peaks can be observed due to the immediate complete consumption

of the analyte and is followed by a reversible peak of the catalyst. Depending on the concentrations of the catalyst and the analyte, two sub-zones are also defined:

- *Zone KT2*: In sub-zone *KT2*, the catalytic current is small and a larger reversible peak of the redox probe is seen along with it.
- *Zone KT1*: The sub-zone *KT1* is observed as we move from zone *KT2* towards zone *K* on increasing the value of γ, where the catalytic current starts increasing and the reversible behaviour of the redox probe gets buried under this wave. On further increase of γ, the distinction of the two peaks is lost and we push the CV response into zone *K*.

3.2 Chemical oxidation of cysteine electrochemically mediated by ferrocene derivatives

Cysteine was electrochemically oxidized using $1,1' - \mathrm{ferrocenedimethanol}$ following EC′ mechanism (figure 3.7a). The cyclic voltammogram for $\mathrm{Fc(MeOH)_2}$ (black curve) can be seen as the reversible curve with equal forward and reverse peak currents while the $\triangle E$ = 0.069 V [‡] and $E_{1/2}$ = 0.271 V [§].

We can observe that upon adding 1.25 mM cysteine (red curve), we have an increase in oxidation current and a decrease in the reduction current, moving our system from *Zone D* to *Zone KG* of the kinetic zone diagram (figure 3.6). This behaviour is consistent with the electrocatalytic activity of iron species towards cysteine as reported in earlier studies [283–285]. The schematic of the EC′ mechanism for oxidation of cysteine by ferrocene derivative(s) can be seen in figure 3.7b. From the forward scan, we can observe that the oxidation current increases with the addition of the cysteine molecules. As the potential increases, the ferrocene molecule oxidizes at the electrode, transferring an electron to the electrode. These oxidized molecules of ferrocene are reduced back to neutral form by reaction with cysteine (as explained earlier with reaction 3.3). Since, we are not limited by the electron transfer at the electrode but rather by diffusion of the molecules at the electrode, the ferrocene molecule can again oxidize at the electrode, transferring another electron to the electrode to increase the overall observed current. Due to this reaction phenomena at the electrode, we observe a higher oxidation current at the electrode upon addition of cysteine in the solution. The ferrocene molecule

[‡] $\triangle E$: potential difference between the forward and reverse peak
[§] $E_{1/2}$: half wave potential is the potential at the middle of forward and reverse peak currents

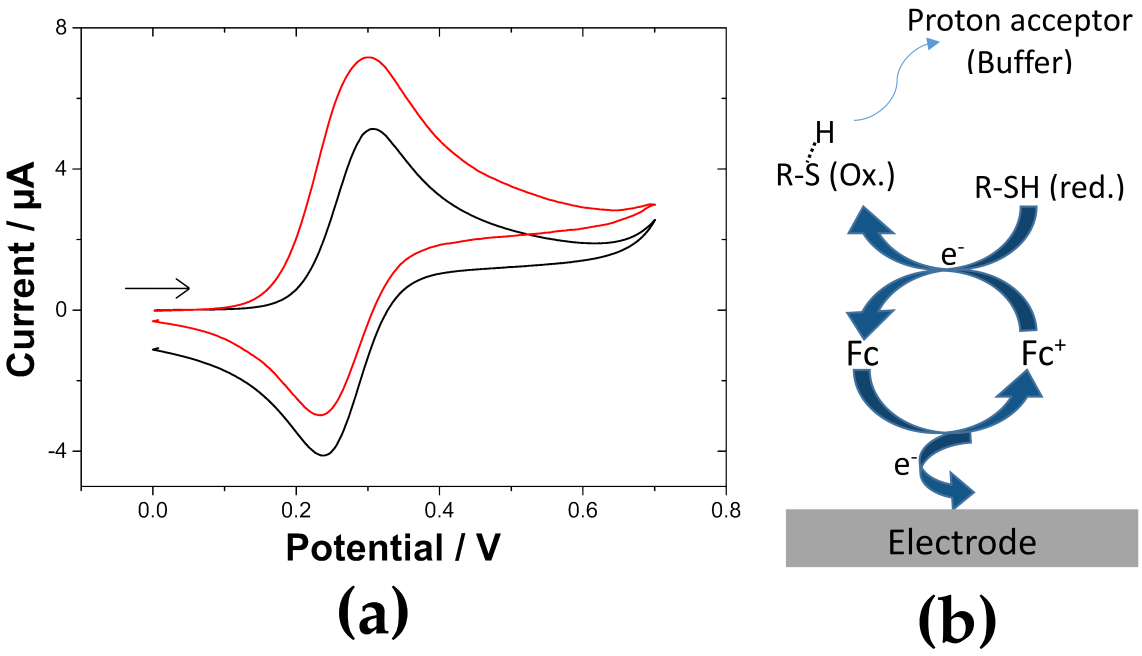

FIGURE 3.7: (a) Cyclic voltammogram at bare ITO with 0 mM (black curve) and 1.25 mM (red curve) cysteine in presence of 0.5 mM $Fc(MeOH)_2$ (γ=2.5); Electrolyte is 0.1 M $Bis-tris$ + 0.1 M $NaCl$ at pH 6.5; ν= 10 mV s^{-1}. (b) Schematic of the oxidation mechanism of thiols using ferrocene.

effectively oxidizes multiple times at the electrode, while oxidizing the cysteine molecules and passing the electrons generated to the electrode.
At reaching the vertex potential, we have a lower number of oxidized redox species, in comparison to the system in absence of cysteine. This decrease in the number of oxidized $Fc(MeOH)_2$ molecules directly impacts the reduction current as the number of oxidized species which can be reduced in the reverse scan of the CV are much lower resulting in a decrease of the cathodic current. This demonstrates that the cyclic voltammogram response after addition of cysteine in figure 3.7a is in good agreement with the underlying EC′ mechanism as depicted in figure 3.7b.

The results show a diffusion limited case at 10 mV s^{-1}, as can be observed at both systems in forward scan direction when the current starts to decrease after reaching a peak current value at 307 mV. At the peak current potential, all the electroactive species at the electrode interface are consumed and the system is dependent on the diffusion of electroactive species to the electrode.
This diffusion limitation of $Fc(MeOH)_2$ was overcome by using a very high excess ratio of cysteine, γ=100, so that we are always in a state where we have an

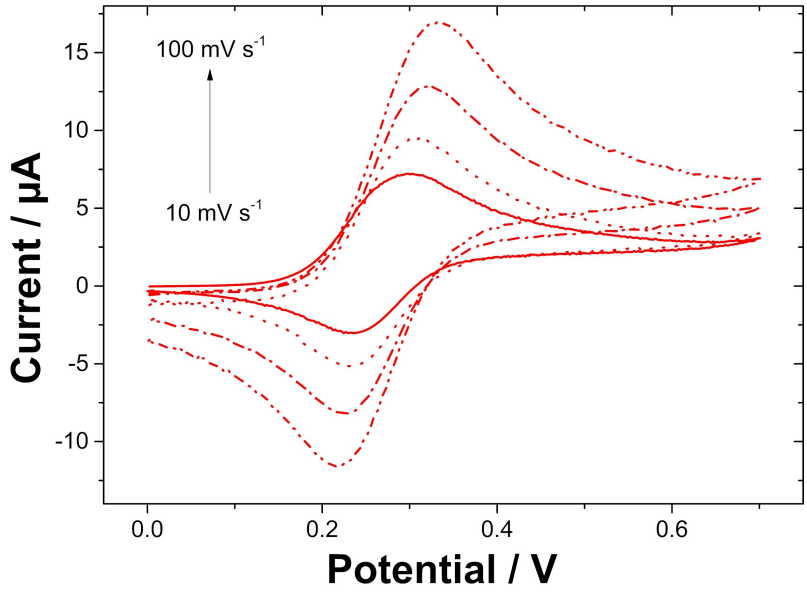

FIGURE 3.8: Cyclic voltammetry at an ITO electrode of 0.5 mM of $Fc(MeOH)_2$ in the presence of 1.25 mM cysteine (γ=2.5); ν= 10, 20, 50 and 100 mV s^{-1}

excess of cysteine at electrode interface and the electrochemical reaction immediately reduces the $Fc(MeOH)_2$ molecule back as soon as it is oxidized. As a result, we have a state where the diffusion of $Fc(MeOH)_2$ does not limit the reaction kinetics anymore as we have a constant availability of reduced $Fc(MeOH)_2$ at the electrode interface, which is the acting catalyst for the oxidation of cysteine. In this condition, we are in fact limited by the electrode efficiency and dimensions. This factor results in the development of steady state behaviour at the electrode (as shown later in figures 3.11 and 3.13) and brings the system to zone KS of the kinetic zone diagram.

The rate kinetics are also affected by the scan rate as it directly correlates to the time interval given for the reaction to proceed. We did a scan rate change study for the EC' mechanism at bare ITO (figure 3.8 and 3.9). In this study, the scan rate was varied from 10 mV s^{-1} to 1 V s^{-1} to understand the effect of time of reaction on the voltammetric response with a solution of 0.5 mM $Fc(MeOH)_2$ in the presence of 1.25 mM cysteine. On analysis, it was observed that at higher scan rates, we observe only the reversible curve corresponding to that of the $Fc(MeOH)_2$ without any indication of an electrocatalytic reaction. But, on the other hand at slower scan rate (when the time between each step is higher) we see the expected response from the EC' reaction (blue, pink and red curve in figure 3.9). Here, from the ratio of the forward and reverse scan peak currents, i_f/i_r, it can be observed that upon reaching higher scan rates, the ratio changes towards value closer to

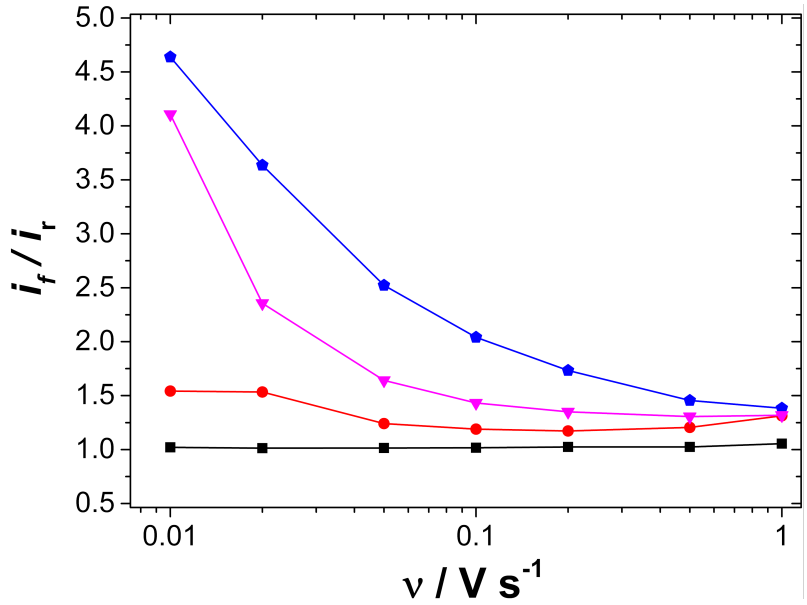

FIGURE 3.9: Ratio of the forward peak current / reverse peak current, i_f/i_r, as a function of the scan rate extracted from cyclic voltammograms obtained at bare ITO electrode with 0.5 mM $\mathrm{Fc(MeOH)_2}$. Cysteine concentration was 0 (black), 1.25 (red), 2.5 (pink) and 4.5 (blue) mM

a system without cysteine (i.e. 1), indicating that no electrochemical reaction between $\mathrm{Fc(MeOH)_2}$ and cysteine proceeds in this case. This was also shown earlier in a report from Nicholson et al. confirming the inverse relation of scan rate to the electrochemical response [286].
This effect also indicates that the rate of electron transfer between the molecules of cysteine and $1,1' - \mathrm{ferrocenedimethanol}$ is smaller than the outer sphere electron transfer of $1,1' - \mathrm{ferrocenedimethanol}$. Overall, this effect helps us to understand that the scan rate is an important factor when we do such experiments because if we observe this reaction at a higher scan rate (100 mV s^{-1} or higher upto γ = 2.5) in cyclic voltammograms, the effect of the reaction is much less pronounced. So, we also understand that the time given to the reaction to proceed is also a limiting factor and can be used to understand the reaction phenomena.

As discussed earlier in section 3.1.3 with kinetic zone diagram, the concentration of the analyte and the catalyst, and the scan rate of the reaction are the major factor deciding the shape of the cyclic voltammogram. As can be seen from figure 3.10, we can observe the different kinetic zones for the given EC' mechanism. Figure 3.10a shows the change in the cyclic voltammogram at a bare ITO electrode as a function of the cysteine (analyte) concentration. As we can see for the black curve at the absence of cysteine, the CV describes the reversible curve of

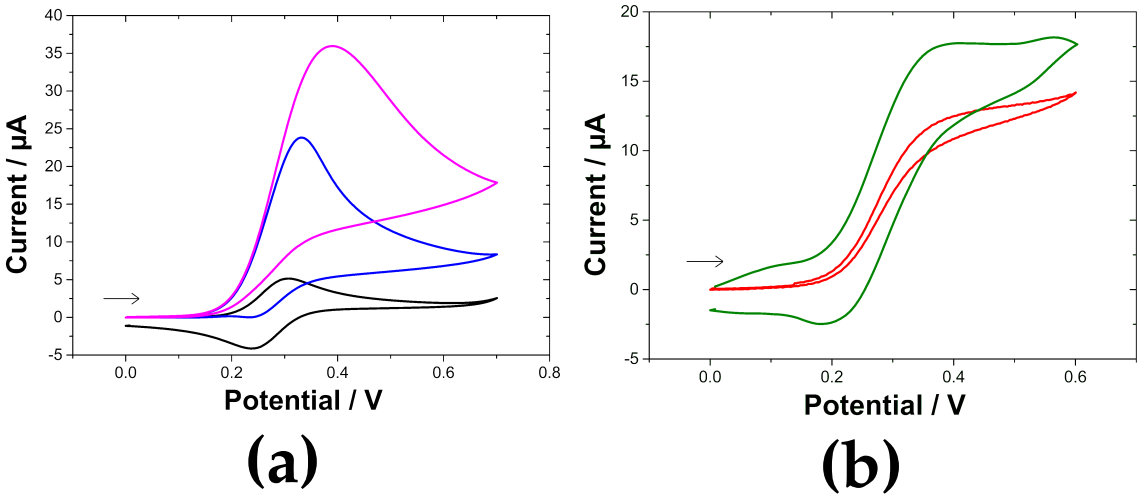

FIGURE 3.10: Cyclic voltammogram at bare ITO with (a) 0.5 mM $Fc(MeOH)_2$ and a γ value of (black) 0, (blue) 5 (pink) 9 with cysteine and ν= 10 mV s^{-1} , (b) 0.0833 mM $Fc(MeOH)_2$ and 8.33 mM cysteine (γ=100) with (red) ν= 10 mV s^{-1} (green) ν= 1000 mV s^{-1}; Electrolyte is 0.1 M $Bis-tris$ + 0.1 M NaCl; pH = 6.5

the $Fc(MeOH)_2$ probe. This region is assigned as the *D* region in the kinetic zone diagram (figure 3.6) for the no catalysis zone. On addition of cysteine, we increase the excess ratio, γ, and move from the *zone D* to *zone KG/KG** (blue curve) where we start to observe an increase in the anodic peak current due to the EC' mechanism while observing a smaller cathodic current. The reaction in this zone is limited by the diffusion of the analyte at the electrode. Upon further increase of the excess ratio, γ, we shift from the *KG/KG** region to *K* region (pink curve) which is a region of pure kinetic condition where the cysteine molecules are completely exhausted at the electrode surface, and the catalytic reaction is limited by the diffusion of the cysteine at the electrode, as can be observed from the shape of the cyclic voltammogram.

Figure 3.10b shows the effect of changing of the scan rate at the cyclic voltammogram. In the example with γ=100 of cysteine, we observe that for 10 mV s^{-1} (red curve), the cyclic voltammogram belongs to *KS* region. The electrochemical response describes the steady state current with no apparent cysteine consumption and limited by the electrode dimension and the kinetics of the reaction. On increasing the scan rate to 1000 mV s^{-1} (green curve), the shape of the cyclic voltammogram shifts to the one seen in region *KD* where we start observing a peak shaped curve as the time given to the reaction to proceed decreases below the rate at which the $Fc(MeOH)_2$ turns over. As discussed earlier, this effect arises at the condition at a high analyte concentration where the scan rate is high, or if the catalyst has a slower rate constant.

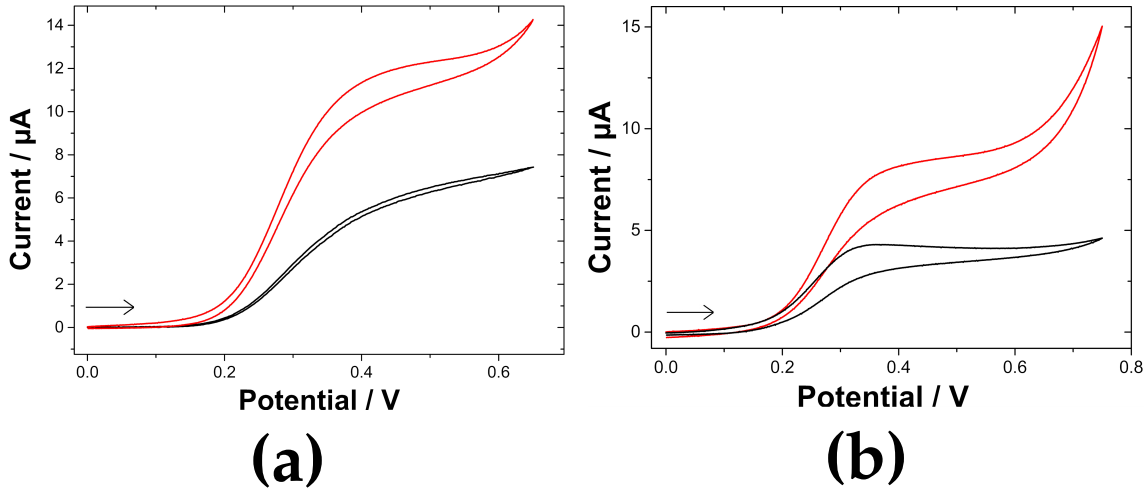

FIGURE 3.11: Cyclic voltammogram at bare ITO with 8.333 mM cysteine in presence of 0.0833 mM $Fc(MeOH)_2$ (γ=100). Electrolyte is (a) NaCl 0.1 M with (red) Bis − tris 0.1 M (black) phosphate 0.1 M; (b) NaCl 0.1 M with (black) 0 mM (red) 10 mM Bis − tris; ν= 10 mV s^{-1} ; pH = 6.5

A pH buffer carries an important task of taking away the proton generated after the oxidation of thiol group, R –(S -H). As shown from cyclic voltammogram of figure 3.11, we can observe that the current is very low ($\sim$ 4.25 µA) when no buffer is used. Since the reaction causes formation of a proton, the reaction causes local decrease of the pH at the electrode interface and thermodynamically the condition does not favour the reaction anymore. The lowering of the steady state current would also directly affect the observable reaction kinetics. On adding 10 mM Bis − tris to the electrolyte solution, we observe the plateau current to be approximately double ($\sim$ 8 µA) indicating that the reaction is favoured by the addition of pH buffer to avoid the decrease of the pH. This result shows that the underlying phenomena behind the cysteine oxidation is highly dependent on presence of an appropriate buffer. An earlier study by *Gagliardi et al.* on electrochemical oxidation of cysteine and N-acetyl-cysteine also describes the importance of buffer (buffers used were phosphate buffer, acetate, tris and histidine) and discusses in detail the concerted electron-proton transfer for this reaction [287].

Since the buffer carries an important role of removing the proton from the reaction, the type of the buffer is also very important in cysteine oxidation reaction. We have compared bis − tris and phosphate buffers to analyse the effect of the activity of buffers at the oxidation reaction (Figure 3.11a). As can be seen from the figure, we get a larger current upon use of bis − tris in comparison to phosphate, which is directly linked to the ability of the bis − tris to remove the proton from

the electrode surface and more effectively maintain 6.5 pH.
For all our studies, we chose to fix the pH at 6.5 and the buffer as $\mathrm{Bis-tris}$ with a concentration of 0.1 M along with 0.1 M NaCl as electrolyte. We use a large concentration of buffer in comparison to that of the reactants so as eliminate any limitation that may arise out of the pH variation at the electrode.

3.3 Electrochemical oxidation of different thiol containing groups using Ferrocene derivatives

3.3.1 Glutathione

Glutathione, as already discussed earlier (section 3.1.1.2) is a very important tripeptide in human body. We can find the cyclic voltammogram for mediated oxidation of glutathione from red curve in figure 3.12. From this figure, we can observe the EC′ mechanism by $1,1'-\mathrm{ferrocenedimethanol}$ at glutathione oxidation. This behaviour is similar to the one observed with cysteine in figure 3.1. In order

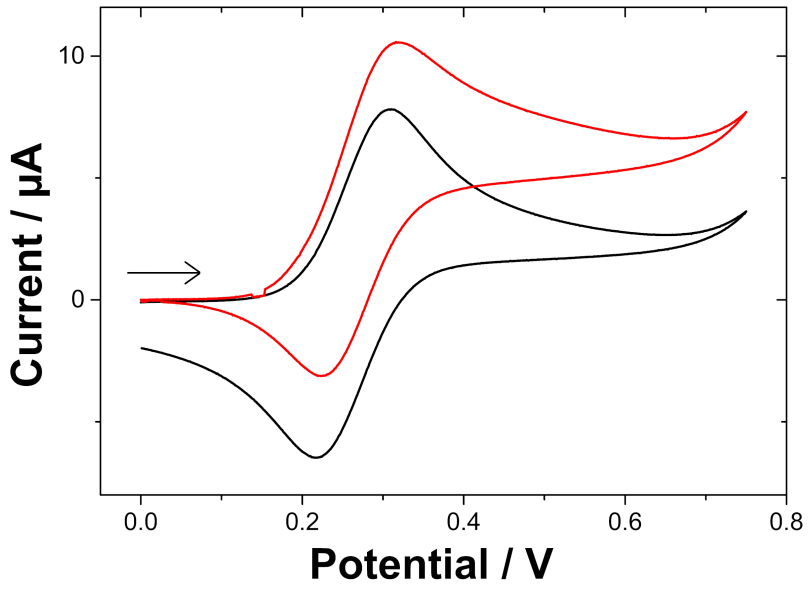

FIGURE 3.12: Cyclic voltammogram at bare ITO with 0 mM (black curve) and 1.11 mM (red curve) glutathione in presence of 0.5 mM $\mathrm{Fc(MeOH)_2}$ (γ = 2.22); Electrolyte is 0.1 M $\mathrm{Bis-tris}$ at pH 6.5; ν= 10 mV $\mathrm{s^{-1}}$

to compare different molecules, we choose to use the conditions discussed earlier with γ=100 (figure 3.13). The $1,1'-\mathrm{ferrocenedimethanol}$ concentration used is 0.0833 mM and cysteine concentration is 0.0833 mM. At this excess ratio, we are in region *KS* of the kinetic zone diagram (figure 3.6) as has already been discussed

in earlier sections. At this experimental condition, the reaction at the electrode is independent of the diffusion of the species and consequently is independent of the scan rate as well. This allows for a direct comparison of the oxidation reaction at the electrode using cyclic voltammograms.

As we can see from figure 3.13, steady state current for glutathione is very low in comparison to cysteine and homocysteine, owing to its low rate of electron transfer with ferrocene.

3.3.2 Homocysteine

Homocysteine has a very similar structure to cysteine but a slightly larger size, which is in fact, intermediate to cysteine and glutathione among the three aminothiols. As can be seen from the blue curve in figure 3.13a, the steady state current for homocysteine oxidation at γ=100 is higher than both cysteine and glutathione. In a previous work, homocysteine has been shown to have higher activity than glutathione and cysteine [288] while a few research have shown that homocysteine is a better reducing agent than the other two aminothiols [244, 289, 290]. It is also shown that the radical of homocysteine form faster in comparison to cysteine in a electrochemical reaction [291].
Thus, we assume that in our system as well, the reaction rate for oxidation of homocysteine through EC' mechanism with ferrocene is higher than that of cysteine or glutathione.

3.3.3 Methionine

As can be seen from figure 3.13b, the cyclic voltammogram for methionine does not exhibit any catalysis reaction at the electrode. We can observe that the dilution of the solution has resulted in a diminished peak current, but in contrast to the other molecules, we do not observe a steady state electrochemical behaviour on addition of the methionine molecule. This result is expected from methionine due to the absence of a thiol group for oxidation with the reaction with $\mathrm{Fc(MeOH)_2^+}$ molecule.

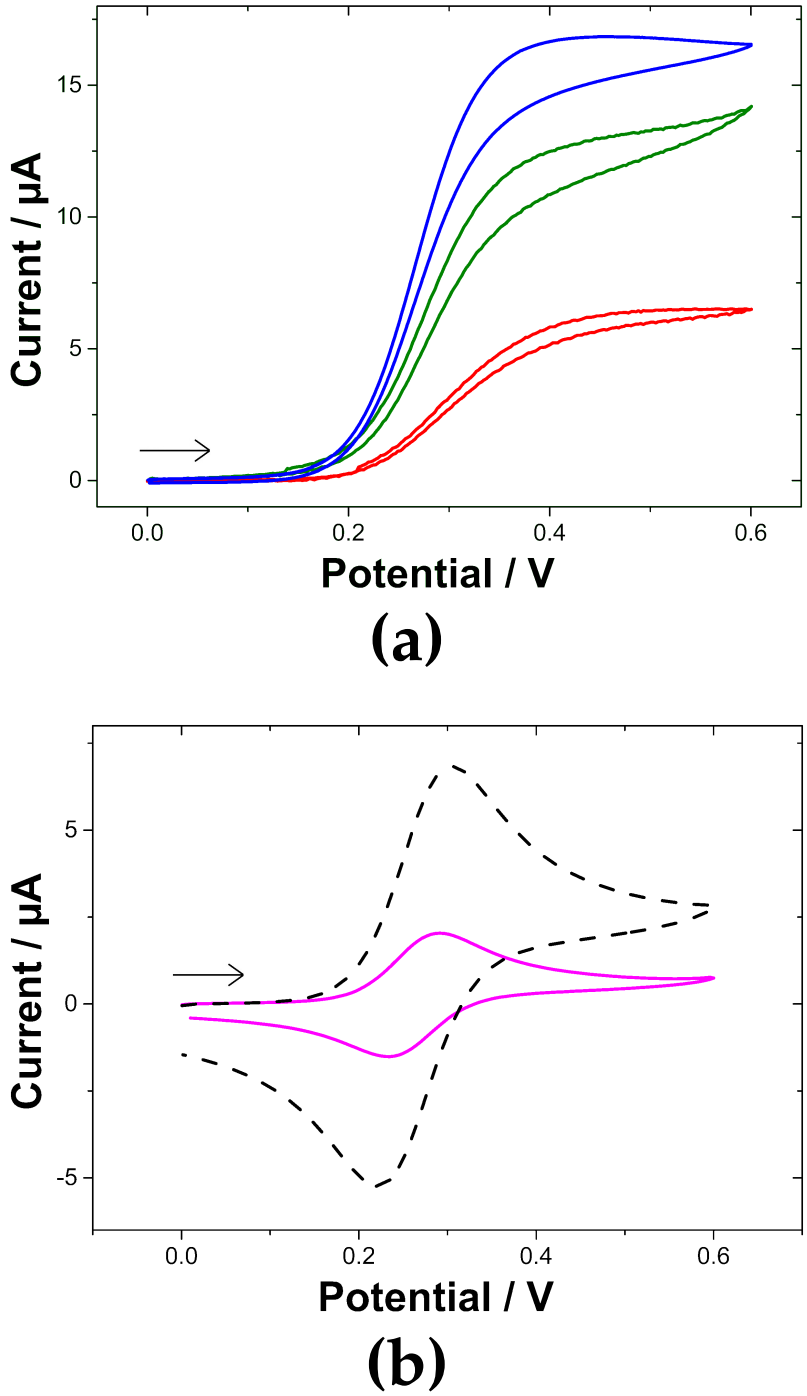

FIGURE 3.13: Cyclic voltammogram at bare ITO with (a) 0.0833 mM $Fc(MeOH)_2$ and 8.333 mM of (red curve) glutathione, (blue curve) homocysteine, (green curve) cysteine and (b) (pink curve) methionine and CV with (black dashed curve) 0.5 mM $Fc(MeOH)_2$ (before dilution with thiol groups); Electrolyte is 0.1 M $Bis - tris$ + 0.1 M $NaCl$ at pH 6.5; ν= 10 mV s^{-1}

3.4 Calculations of rate kinetics

In order to determine the rate constants for the oxidation of cysteine, glutathione and homocysteine, we chose to compare the cyclic voltammograms at a very large excess ratio (γ) of 100 (figure 3.13). At such a high excess ratio, it is in the *KS* region of the kinetic zone diagram as already discussed in figure 3.6. The advantage of having the system at this excess ratio is to allow it be in a diffusion-independent state where the apparent concentration of the analyte does not change with it's consumption at the electrode. The continuous appearance of the analyte at the electrode interface makes for a continued electrocatalysis cycle for the ferrocene (or it's derivative) molecule and this allows it to remain in a state where it is not limited by the diffusion of the redox species, but rather by the activity and dimension of the electrode surface, the rate of transfer of electron between the analyte and the catalyst (k_e), and the rate of transfer of electron between the catalyst and the electrode. In region *KS*, since the system is independent of diffusion of species at the electrode, the electrochemical response for the system is also independent of the scan rate for the cyclic voltammetry (discussed in detail later in chapter 4, figure 4.10). In this case, the observable rate of reaction can easily be calculated with cyclic voltammogram as the underlying equation for the steady-state current in this region is much simpler [280, 281, 286, 292].

$$i_{ss} = nFAC^{\circ}_{Fc(MeOH)_2}\sqrt{D_{Fc(MeOH)_2}k_{obs}} \tag{3.6}$$

$$k_e = \frac{k_{obs}}{C^{\circ}_{cys}} \tag{3.7}$$

where,

n	1	number of electron transferred,
F	$96\,485.33\,\mathrm{C\,mol^{-1}}$	faraday's constant,
A	$0.188\,\mathrm{cm^2}$	surface area of the electrode,
C°_{cys}	$8.333 \times 10^{-6}\,\mathrm{mol\,cm^{-3}}$	bulk cysteine concentration,
$C^{\circ}_{Fc(MeOH)_2}$	$8.333 \times 10^{-8}\,\mathrm{mol\,cm^{-3}}$	bulk $\mathrm{Fc(MeOH)_2}$ concentration,
$D_{Fc(MeOH)_2}$	$7 \times 10^{-6}\,\mathrm{cm^2\,s^{-1}}$	diffusion coefficient for $\mathrm{Fc(MeOH)_2}$,
i_{ss}	measured from CV	steady state current of the sigmoidal shaped cyclic voltammogram,
k_{obs}	calculated from eq. 3.6	observable rate constant for the reaction,

k_e	calculated from eq. 3.7	rate of transfer of electron between $Fc(MeOH)_2^+$ and cysteine (red.) molecule

Using these values in equation 3.6 and 3.7, we can calculate the values of k_{obs} and k_e as given in table 3.2. As we can observe from these values, the observable reaction rate for cysteine oxidation is approximately 3.6 times to that of glutathione.

Analyte	i_{ss} (µA) *	k_{obs} (s^{-1})	k_e ($L\,mol^{-1}\,s^{-1}$)
Cysteine	11.3 ± 0.2	7.9 ± 0.2	$(9.5 \pm 0.3) \times 10^5$
Glutathione	6.0 ± 0.1	2.2 ± 0.1	$(2.7 \pm 0.1) \times 10^5$
Homocysteine	16.4 ± 0.1	16.8 ± 0.1	$(2.0 \pm 0.1) \times 10^6$

* Value of i_{ss} measured at E = 0.45 V

TABLE 3.2: Calculated values of k_{obs} and k_e

3.5 Conclusion

The direct oxidation of cysteine on ITO or glassy carbon electrode is affected by poor charge transfer at the electrodes and a large overpotential of $\sim$1 V is observed. Oxidation at such a large potential can cause unwanted oxidation of other molecular species in the solution and passivation of the electrode surface.

We demonstrated electrochemically mediated oxidation of cysteine, glutathione and homocysteine on bare ITO electrode by a $\mathrm{ferrocenedimethanol}$ ($\mathrm{Fc(MeOH)_2}$) following the EC' mechanism. The EC' mechanism for the given electrochemical reaction was shown to depend on different experimental factors such as the scan rate of the CV and the concentration of the electrocatalyst and the analyte. On varying these parameters, the different regions of the kinetic zone diagram were accessed and a difference in the shape and current at the cyclic voltammograms was observed. The variation in scan rates from $10\,\mathrm{mV\,s^{-1}}$ to $1000\,\mathrm{mV\,s^{-1}}$ for different analyte concentrations at ITO electrode showed that the ratio i_f/i_r was higher at the slowest scan rate and decreased to a value close to 1 at the highest scan rate, indicating that the catalytic reaction for the cysteine oxidation is slower than the outer sphere electron transfer of $\mathrm{Fc(MeOH)_2}$ molecule and is limited by the time given for the reaction to proceed. The ratio for different analyte concentrations at the different scan rates was plotted and a dependency of the reaction on the analyte concentration and the scan rates was observed.

It was observed that since the reaction generates a proton at the electrode, it would result in the lowering of the pH at the electrode interface and a pH buffered solution was required along with the electrolyte to maintain the pH values. In the absence of such a buffer, the electrochemical response declined indicating that the reaction was not favourable. On comparison of buffer types, bis-tris buffer was found to have higher efficiency at the reaction than phosphate buffer saline.

The rate kinetics for the oxidation of the different aminothiols were calculated by bringing the excess ratio, γ, to 100. At this excess ratio the system was in *KS* region of the kinetic zone and is not limited by diffusion of the species at the electrode. The k_{obs} values for cysteine, glutathione and homocysteine were calculated to be $(7.9 \pm 0.2)\,\mathrm{s^{-1}}$, $(2.2 \pm 0.1)\,\mathrm{s^{-1}}$ and $(16.8 \pm 0.1)\,\mathrm{s^{-1}}$ respectively. As can be observed from these values, the rate kinetics for cysteine is $\sim$ 3.6 times higher than glutathione.

Chapter 4

Thiol oxidation at Silica modified Indium tin oxide (ITO)

Chapter Plan

4.1 Introduction

Mesoporous silica is a very versatile material imparting a variety of properties to the electrode [2–4, 22–26]. As discussed earlier in chapter 1, there are a lot of methods for deposition of mesoporous silica, but we have focused on electrochemically assisted self-assembly (EASA) method [160] to afford vertically-oriented, ordered mesoporous silica thin films. Using EASA method, ordered mesoporous silica can be deposited on different types of electrodes like ITO (Indium tin oxide) [160], FTO (fluorine tin oxide) [293], carbon [166], platinum [166], gold [294], etc. For the entirety of this chapter, we use Indium Tin Oxide (ITO) electrodes for the deposition of mesoporous silica thin films. These silica modified ITO electrode allow for a comparative study with bare ITO electrodes (discussed in chapter 3) and can help us to understand the effect of mesoporous silica thin film on an electrode and its effect in relation to the size and charge of the molecules which diffuses through the pores to access the electrode. As we will discuss in the following section (4.2), the pores in silica thin films are vertically oriented allowing for mass transport of molecules and can be used to harness sensing applications such as detection of cationic organic molecules [170], and inorganic anions [174]. Further, we will also discuss how we can use the various properties of a mesoporous film to study the oxidation of cysteine, glutathione, and homocysteine, and use of ferrocene-functionalized mesoporous silica thin film electrode for selective detection of cysteine over glutathione.

Vertically oriented mesoporous silica films were prepared by electrochemically assisted self-assembly (EASA) method as described previously [160] (the deposition process has been discussed in detail earlier in section 2.4.1). In EASA method, a suitable cathodic bias of the electrode caused an increase of pH in the vicinity of the electrode causing the condensation of the hydrolysed TEOS (which was set at pH 3). Simultaneously, this also favours the deposition of the hemispherical micelle structures of CTA^+ at the electrode, giving rise to the templated structure of the silica thin film. The ratio of TEOS:CTAB was kept at 0.32 which has proved to generate reproducible films of good ordered structure [161]. Mesoporous silica films were then characterized by various methods as described in the following section (section 4.2).

4.2 Characterization of Mesoporous Silica thin film (MSTF)

After the deposition of mesoporous silica on an electrode with EASA method discussed earlier in section 2.4.1, various different characterization were regularly performed in order to make sure that there was no structural defect in the silica deposits. Mesoporous silica thin films were characterized by electrochemistry (section 4.2.1), grazing-incidence small-angle x-ray scattering (GISAXS) (section 4.2.2), and transmission electron microscopy (TEM) (section 4.2.3) in the following sections.

4.2.1 Electrochemical characterization using redox probes

Electrochemistry has been employed to characterize the mesoporous silica thin films by exploiting the various known properties of these modified electrodes such as the negative charge of silica at neutral pH due to the presence of silanolate functions, and the small size of pores [169, 171, 174].
Cyclic voltammetry with three different redox probes (figure 4.1) was used to characterize the mesoporous silica films: (i) a cationic probe, $[Ru(NH_3)_6]^{3+}$; (ii) a neutral probe, $[Fc(MeOH)_2]$ and ; (iii) an anionic probe, $[Fe(CN)_6]^{3-}$. The electrochemical behaviour observed with different types of charged redox-active species allow for a different behaviour from the electrode. Since, silica is negatively charged at neutral pH, the electrostatic forces play an important role in the electrochemical behaviour of the redox probes at the modified electrode. Apart from that, when the CTA^+ molecules are present in the pores, the solubilization of the molecular species in its liquid crystal structure is necessary for diffusion through them.

Cyclic voltammograms were obtained before modification i.e. at a bare ITO electrode (black curves), and after mesoporous silica deposition through EASA method once before (blue curves) and once after (red curves) the (CTA^+) template removal. This electrochemical characterization procedure allows us to detect any defect in the mesoporous silica thin film deposits [160].
For the cationic and anionic probes, a normal peak shaped curve was observed at the bare electrode while the absence of signal after electrochemically assisted self-assembly of silica confirmed the defect-free deposition of silica film as the electrode could not be accessed from the solution through the silica film. The pores blocked with CTA^+ cause an electrostatic repulsion with the positive $[Ru(NH_3)_6]^{3+}$ probe making it inaccessible at the electrode surface. No signal was observed for

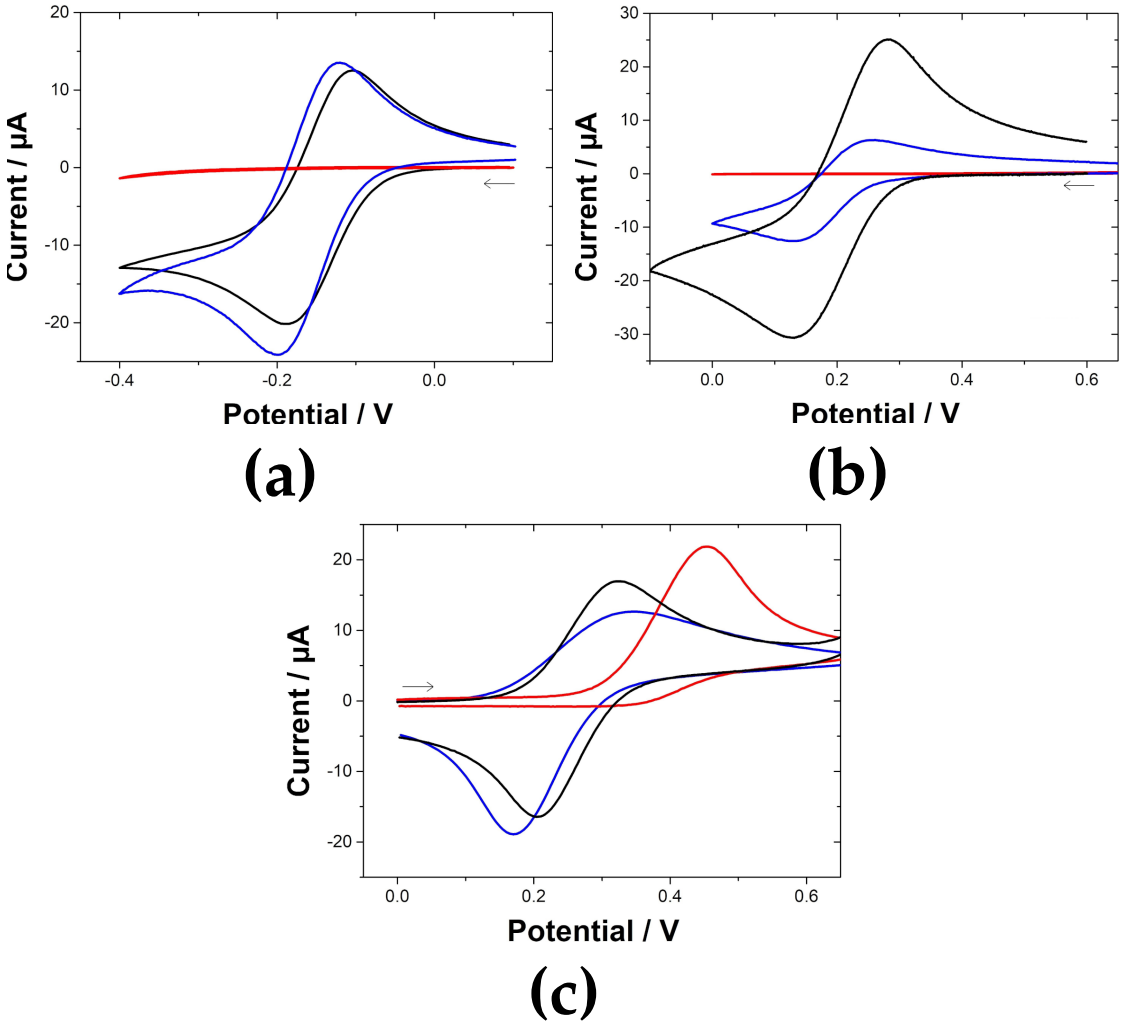

FIGURE 4.1: Cyclic voltammetry of 0.5 mM of the following redox probes: (a) $Ru(NH_3)_6^{3+}$,(b) $Fe(CN)_6^{3-}$, (c) $Fc(MeOH)_2$ on bare electrode (black curve), silica film before (red curve), and after template extraction (blue curve); Electrolyte used is 0.1 M $NaNO_3$; $\nu = 50\,mV\,s^{-1}$

the anionic probe as well which could not diffuse through the CTA^+ layer and transfer electrons at the electrode surface . For the neutral redox probe, the signal was obtained but at higher anodic potentials when mesochannels of the silica films were still blocked with the surfactant molecule, with a peak at 0.453 V. This was due to the lipophilic tail of the CTA^+, which allowed the solubilisation and permeation of $Fc(MeOH)_2$ probe but not the others. We can also observe that there is no reverse peak for $Fc(MeOH)_2$ as upon oxidation the ferrocene molecule gains a unit positive charge and is expelled from the CTA^+ filled mesopores due to electrostatic repulsion.

After removal of the surfactant, the orientation of the pores perpendicular to the electrode surface promoted the mass transport of cationic and neutral species and

the cyclic voltammetry response reached the one obtained at the bare electrode. However, for $[Fe(CN)_6]^{3-}$, the signal was dramatically decreased due to the electrostatic repulsion between the anionic probe and the negatively charged silica walls. Apart from this, we can also observe from the cyclic voltammograms with $Fc(MeOH)_2$, that the reverse peak current is larger than the forward peak current. This can be attributed to electrostatic accumulation of its cationic form at the negatively charged silica walls. This results in a larger concentration of the oxidised form of the probe available for reduction during the reverse scan producing a larger reverse current peak. These are the typical voltammograms observed for high quality and homogenous mesoporous silica deposits as has been shown in earlier studies [160, 161]

4.2.2 GISAXS characterization and calculation of d-spacing

Grazing-incidence small-angle x-ray scattering (GISAXS) measurements were done directly on the MSTF deposited electrode surface without any other pretreatment of the sample. This is a non-destructive technique and allows the possibility to use the electrodes later for other applications The GISAXS results are used to probe the surface structure of a sample, and if there are any particles or inhomogeneities on the surface, it scatters and diffuses the incoming x-ray beam.
The GISAXS pattern for the mesoporous silica thin film can be seen in figure 4.2.

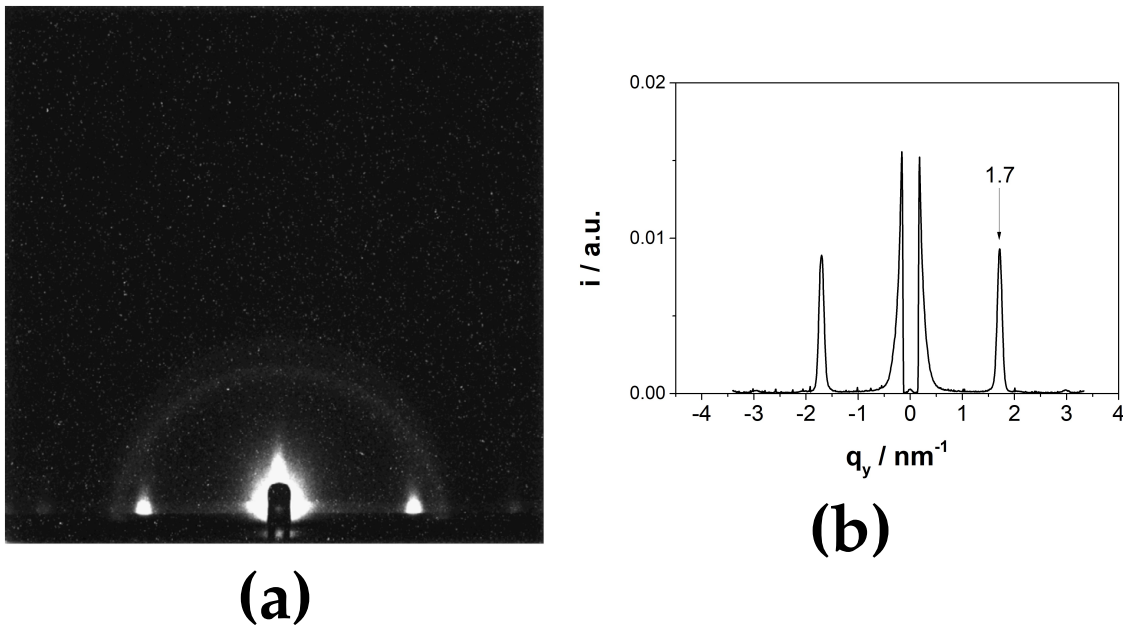

FIGURE 4.2: (a) GISAXS patterns and (b) integrated intensity profiles along q_y direction of a mesoporous silica film prepared according to the electrodeposition procedure described in 2.4.

There are two important interpretation which can be done from the GISAXS spectra.

- The first is the nature of the GISAXS spectra (figure 4.2a). As discussed in section 2.3.2.1 and seen earlier in figure 2.7, the scattering rods structure represent perpendicular lamellae over a long order. Thus, the scattering rods structure seen in figure 4.2a directly corresponds to long ordered perpendicular porous structure of the silica film. The presence of a faint powder ring also points towards the presence of some irregular silica structures on the electrode surface, but the intensity seems to be much less for this signal.
- The 'q' value of the peak of signal (figure 4.2b) can be used to calculate the d-spacing according to equation 2.5 as already discussed in section 2.3.2.1 and deduced earlier on page 38. This d-spacing can be used to understand the distance between two consecutive planes (the real space repeat-structure distance) in the ordered lattice structure [295].

$$d = \frac{2\pi}{q} \qquad \text{(from eq. 2.5)}$$

From the figure 4.2, we find that $q = 1.7$ nm, which gives us,

$$d = \frac{2\pi}{1.7}$$
$$\therefore \quad d = 3.69 \text{ nm} \qquad (4.1)$$

Thus, from the GISAXS spectra, a d-spacing of 3.69 nm can be calculated for the mesoporous silica thin films.

4.2.3 Transmission electron microscopy

The level of mesostructural order was evaluated by TEM using a Philips CM20 microscope at an acceleration voltage of 200 kV. The samples were prepared by removing some pieces of the silica thin films from the electrode and were supported on the carbon-coated copper grid.
From the TEM image (Figure 4.3), we can observe that the EASA method has led to the formation of about 100 nm thick films with mesopores of $\sim$2.4 nm in diameter. Those pores are organized in a hexagonal compact arrangement and are oriented perpendicular to the electrode surface, allowing efficient mass transport of molecules from the bulk of the solution to the electrode surface, through the mesoporous silica films [161]. The transmission electron micrographs also

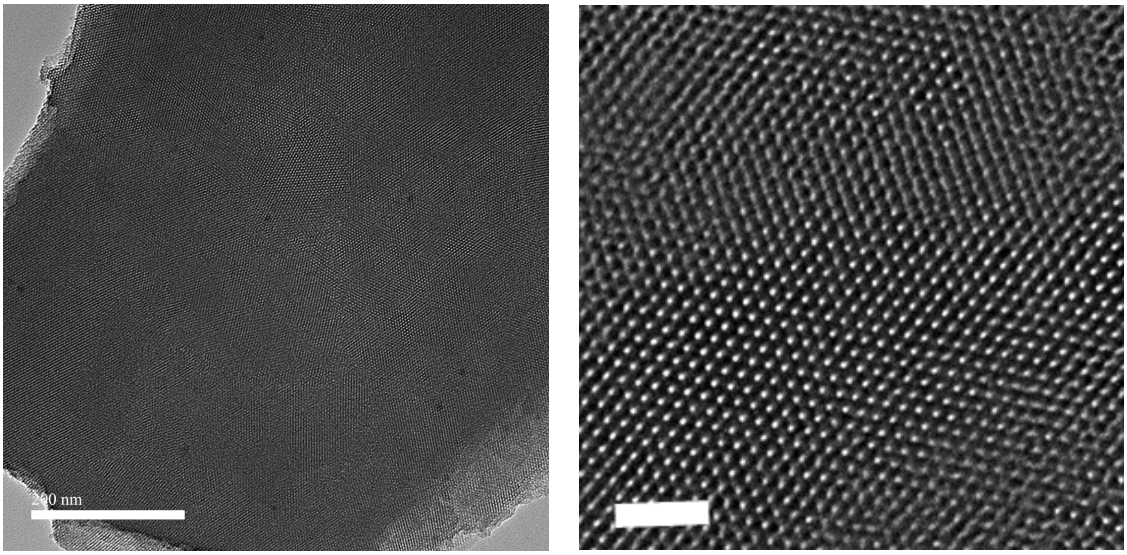

FIGURE 4.3: Transmission electron micrographs of a mesoporous silica thin film (top view) prepared according to the protocol described in 2.4.1. Scale bar: (a) 200 nm (b) 20 nm

show the highly ordered structure arising from the electrochemically assisted self-assembly (EASA) process.

4.3 Thiol oxidation at silica modified indium tin oxide electrode

4.3.1 Cysteine electrochemistry at modified ITO

As we have already observed cysteine oxidation mediated by ferrocene dimethanol at bare ITO earlier in section 3.2, a comparative study with ITO modified with mesoporous silica can help us to understand the effect of mesochannels and 1D confinement of molecules on such a reaction. Figure 4.4a shows the cyclic voltammetry of 0.5 mM of $Fc(MeOH)_2$ at an electrode modified with mesoporous silica film, which occurred at $E_{1/2}$ = 0.252 V .

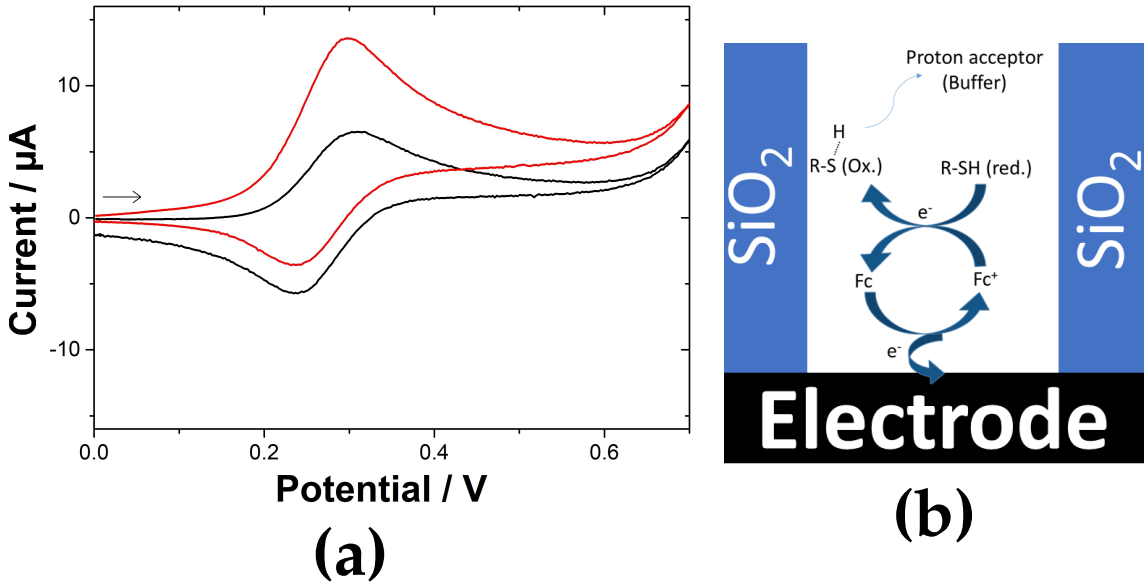

FIGURE 4.4: (a) Cyclic voltammetry at a mesoporous silica film electrode of 0.5 mM of $Fc(MeOH)_2$ in the absence (black curve) and in the presence (red curve) of 1.25 mM cysteine; Electrolyte: $Bis-tris$ 0.1 M + $NaCl$ 0.1 M; ν= 10 mV s^{-1}. (b) Scheme of thiol oxidation at MSTF mediated by ferrocene

The addition of 1.25 mM of cysteine to the solution led to the increase of the forward current and the decrease of the reverse peak current. As was observed in section 3.2 at a bare ITO electrode, $Fc(MeOH)_2^+$ formed at the electrode surface transferred an electron from cysteine, and was reduced back to $Fc(MeOH)_2$. The molecule of $Fc(MeoH)_2$ was then regenerated, causing the rise in forward peak current, in good agreement with an EC' mechanism (as explained earlier in section 3.1.3). A schematic of the reaction can be found in figure 4.4b. The mesochannels do not restrict the diffusion of neutral redox probes like $Fc(MeOH)_2$, as has been seen earlier from figure 4.1c. The effect of the mesochannels on the mass

transport of molecules has been previously studied and is dependent on various factors:

- Diffusion of various molecules into pores towards the electrode. The apparent diffusion coefficient, electrolyte, pH, solvent play a role in deciding the rate of diffusion.
- Size selection of molecules and molecular sieving properties as has already been reported earlier[26, 146, 169, 296, 297].
- Positively charged species tend to accumulate in the silica film due to electrostatic interaction with the negatively charged silica thin film at neutral pH [167].
- With the accumulation of cationic molecules, we need diffusion of counter anions to balance the increase of positive charge at the electrode [298]. This diffusion of anion can be affected by the charge of the silica film, pH of the electrolyte, applied potential, ionic strength, etc.

4.3.1.1 Changing of scan rate for electrochemical oxidation of cysteine at modified ITO

The scan rate was varied from $10\,\mathrm{mV\,s^{-1}}$ to $1000\,\mathrm{mV\,s^{-1}}$ to understand the effect of reaction time on the voltammetric response of a solution of 0.5 mM of $\mathrm{Fc(MeOH)_2}$ in the presence of 1.25 mM cysteine at a mesoporous silica electrode (Figure 4.5). At $10\,\mathrm{mV\,s^{-1}}$, the reverse peak is much smaller with a ratio of forward peak current over reverse peak current, $i_f/i_r = 1.9$.

The forward current increased with the scan rate along with the appearance of a larger current in the reverse scan, indicating that the overall reaction kinetics was limited by the rate of electron transfer between the thiol group and the redox mediator and not by the electron transfer between the redox mediator and the electrode. Figure 4.6 showed the i_f/i_r ratio for concentrations of cysteine of 1.25 mM, 2.5 mM and 4.5 mM, at scan rates varied between $10\,\mathrm{mV\,s^{-1}}$ to $1\,\mathrm{V\,s^{-1}}$. Those were compared to the reversible signal observed in the absence of cysteine (data shown as discs in Figure 4.6). For the three cysteine concentrations, the i_f/i_r ratio decreased as the scan rate increased, to reach unity at the fastest scan rate of $1\,\mathrm{V\,s^{-1}}$. At such a scan rate, only the reversible electrochemical response of $\mathrm{Fc(MeOH)_2}$ was observed and no apparent cysteine oxidation is observed.

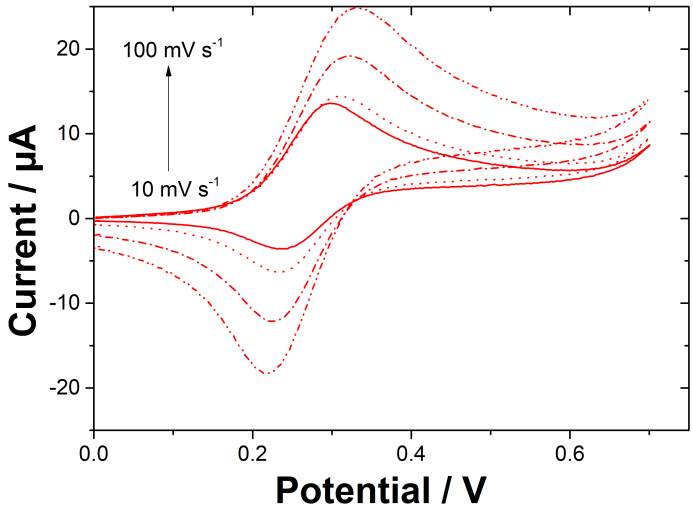

FIGURE 4.5: Cyclic voltammetry at a mesoporous silica film electrode of 0.5 mM of $Fc(MeOH)_2$ in the presence of 1.25 mM cysteine; ν= 10, 20, 50 and 100 mV s^{-1}; Electrolyte: $Bis-tris$ 0.1 M + $NaCl$ 0.1 M

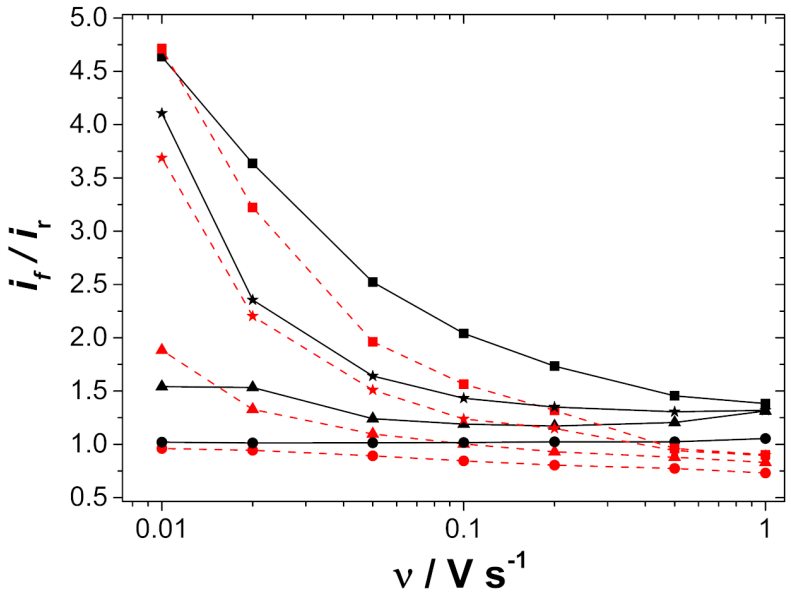

FIGURE 4.6: Ratio of the forward peak current / reverse peak current, i_f/i_r, as a function of the scan rate at bare ITO electrode (black solid lines) and at mesoporous silica film electrodes (red dashed electrodes) with 0.5 mM $Fc(MeOH)_2$. Cysteine concentration was 0 mM (discs), 1.25 mM (triangles), 2.5 mM (star) and 4.5 mM (squares); Electrolyte: $Bis-tris$ 0.1 M + $NaCl$ 0.1 M

The i_f/i_r ratio was also compared at both bare and modified electrode (Figure 4.6). The current ratio was slightly lower at the electrodes modified with mesoporous silica film than at bare ITO electrodes, suggesting that the presence of the film has impacted the overall kinetics of the reaction. The most likely reason for slower kinetics is the mass transport limitation of the molecular species ($\mathrm{Fc(MeOH)_2}$ and thiol) within the mesopores, despite the perpendicular orientation of the pores to the electrode surface (as discussed further in section 4.3.2). As discussed earlier in Chapter 3, the chemical reaction requires the presence of both $\mathrm{Fc(MeOH)_2}$ and $\mathrm{cysteine}$ along with the pH buffer and the absence of either of these affects the reaction kinetics.

4.3.2 Electrochemical Impedance Spectroscopy (EIS)

Electrochemical Impedance Spectroscopy was performed at both bare ITO electrode and mesoporous silica thin film modified ITO electrode using frequency from 0.1 Hz to 100 kHz (figure 4.7) at a high excess ratio of cysteine (γ=100). The applied potential was fixed at 0.3 V and the amplitude change was set at 0.03 V (10 % of the value of the applied potential). The potential of 0.3 V allowed us to be at higher anodic potential than the oxidation potential of the redox probe, $\mathrm{Fc(MeOH)_2}$ (as can be observed from the cyclic voltammograms), and would allow us to follow the ferrocene mediated cysteine oxidation reaction (as observed earlier from 3.7a and 4.4a). We used an excess ratio, γ, of 100 for cysteine in this EIS experiment.

It can be observed from the impedance behaviour at lower frequencies for bare ITO (black points in figure 4.7) that we can observe a semicircle from the solution resistance, R_S, and the charge transfer resistance, R_{CT} but do not see any diffusion component (or mass transfer impedance) for this case. This directly describes that, in this case, there is no apparent mass-transfer impedance associated with this system [299]. However, at mesoporous silica, the Nyquist plot reveals that at low frequency there is an appearance of a diffusion coefficient signifying infinite resistive behaviour at the mesoporous silica electrode due to the mass transport of the molecular ($\mathrm{Fc(MeOH)_2}$ and cysteine) species.

We can deduce from this result that the there is an impedance component associated with the MSTF deposited ITO electrode system and it can be contributed to the mass transport of $\mathrm{Fc(MeOH)_2}$ and cysteine in the film.
Further, we can observe from the semicircles formed in figure 4.7, which directly correspond to the charge transfer resistance, that a slightly smaller semicircle is formed at mesoporous silica coated ITO electrode in comparison to the bare ITO

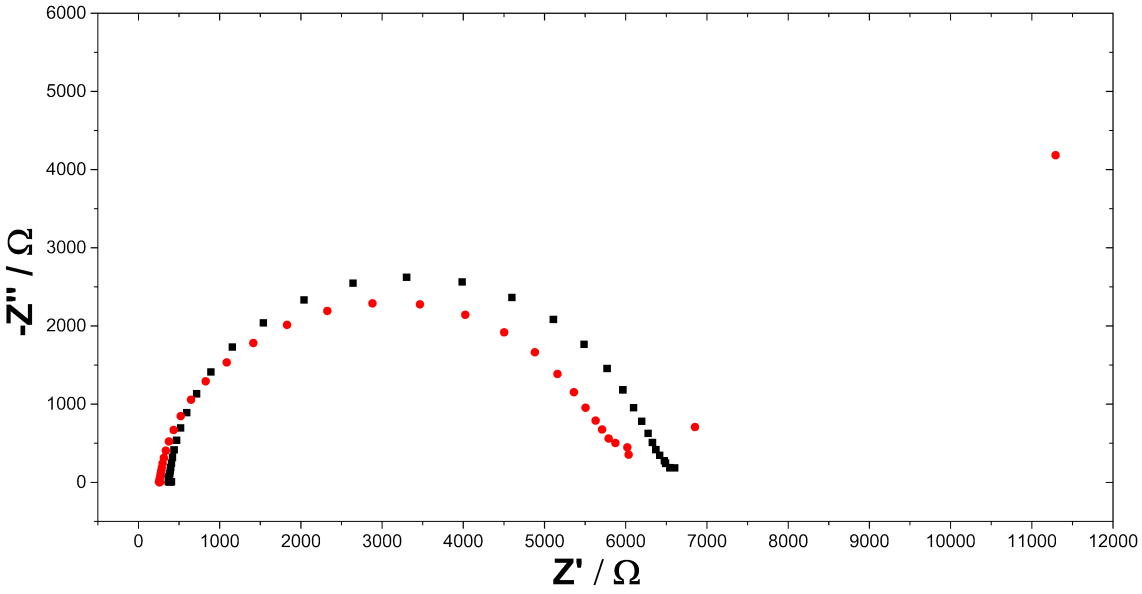

FIGURE 4.7: Electrochemical Impedance Spectroscopy result at (black) bare ITO electrode, and (red) ITO electrode coated with MSTF. The frequency is varied from 0.1 Hz - 100 kHz with the base potential at 0.3 V and a changing amplitude of 0.03 V. [Cysteine] = 8.33 mM; [$Fc(MeOH)_2$] = 0.0833 mM; Electrolyte: $Bis-tris$ 0.1 M + $NaCl$ 0.1 M

electrode. Since, we know that the cationic form of ferrocene gets accumulated in the pores, we have a higher catalyst density in the pores at the electrode vicinity, which can possibly increase the catalytic response of this system. This result is very interesting as it shows that the electrochemical reaction in the mesochannels of the silica is perhaps better (or atleast similar) than that at the bare electrode, but the observable rate of reaction is slower for this case, because we add a high diffusion resistance to this system. From the EIS results, we can say that the diffusion resistance of the species overcomes the slightly improved charge transfer efficiency, lowering the k_{obs} for mesoporous silica in comparison to that of bare ITO electrode. We assume here that the electron transfer rate between ferrocenium and cysteine, k_e, is same for both the cases and is unaffected by the presence of silica thin film. The diffusion of the molecular species ($Fc(MeOH)_2$, cysteine and the buffer) through the mesopores limit the catalytic response at the mesoporous silica modified electrode.

4.3.3 Glutathione electrochemistry at modified ITO

As already discussed in section 3.1.1.2, the glutathione molecule is a tri-peptide molecule containing cysteine as one of the amino acids. This imparts similar chemical properties to glutathione as cysteine, allowing them to undergo similar chemical reactions [300]. Thus, in order to be able to selectively detect one of these in presence of the other remains very challenging.

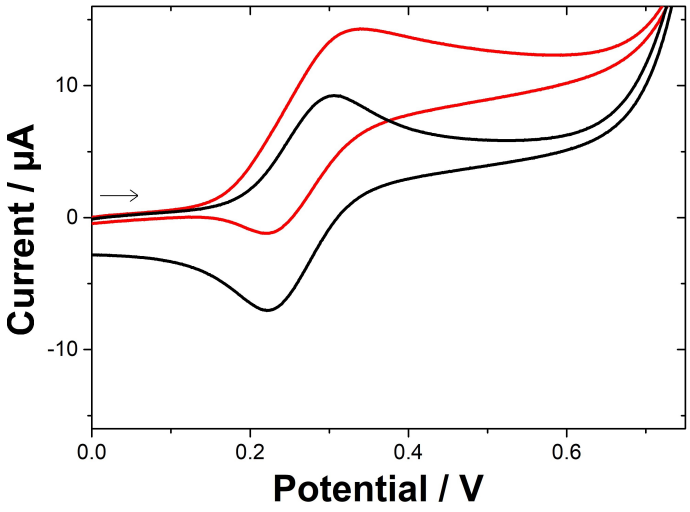

FIGURE 4.8: Cyclic voltammetry at a mesoporous silica film electrode of 0.5 mM of $Fc(MeOH)_2$ in the absence (black curve) and presence (red curve) of 1.49 mM glutathione; Electrolyte: $Bis-tris$ 0.1 M + NaCl 0.1 M; ν= 10 mV s^{-1}

In figure 4.8, we can find cyclic voltammogram for the mediated oxidation of glutathione with $Fc(MeOH)_2$. The mechanism of glutathione oxidation mediated by $Fc(MeOH)_2$ is similar to cysteine oxidation. When we compare the oxidation of cysteine to that of glutathione, similar results were observed when 1.49 mM of glutathione was added to 0.5 mM solution of $Fc(MeOH)_2$ (Figure 4.8), indicating that the thiol function of glutathione could be oxidised in the same way as the one of cysteine (as shown in section 4.3.1). We can observe that the forward peak current has increased while the reverse peak current has decreased at glutathione additions.

The cyclic voltammograms with lower analyte concentration discussed earlier in section 4.3.1 and 4.3.3 are limited by diffusion of various molecular species (as can be seen in figure 4.4a and 4.8). At this particular system, it is difficult to calculate the rate kinetics of the reaction processes at the electrode and does not allow for a direct comparison between different cyclic voltammograms at different systems. In order to be able to compare the systems, we use experimental

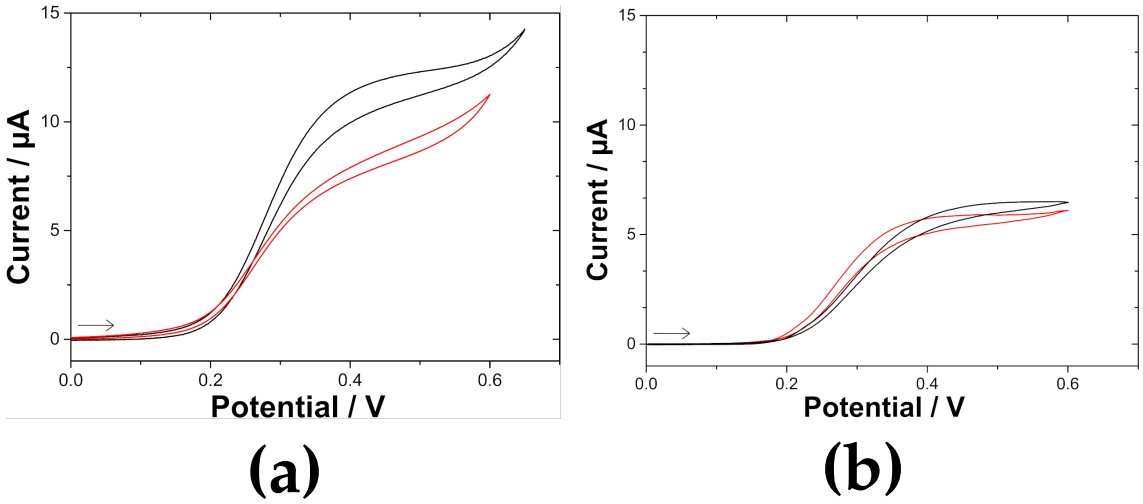

FIGURE 4.9: Cyclic voltammetry of 0.0833 mM of $Fc(MeOH)_2$ for a large excess (γ = 100) of (a) cysteine (b) glutathione at a bare electrode (black curve) and at a mesoporous silica film electrode (red curve); Electrolyte: $Bis-tris$ 0.1 M + $NaCl$ 0.1 M; ν = 10 mV s^{-1}

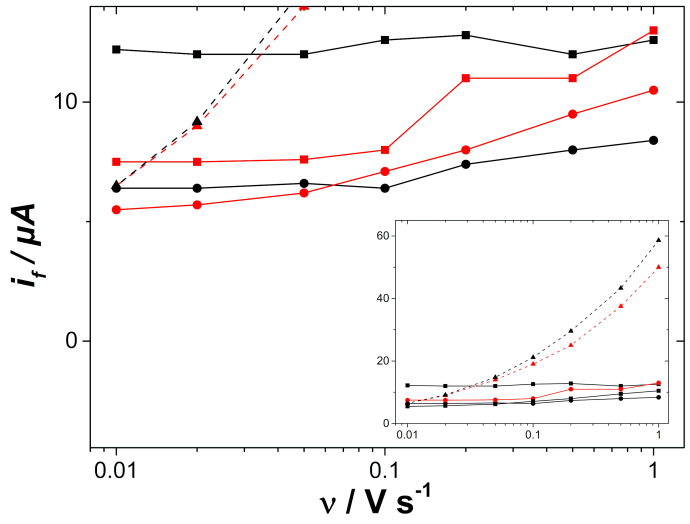

FIGURE 4.10: Forward peak current (i_f)/steady state current (i_{ss}) as a function of scan rate at (black) bare ITO, (red) mesoporous silica film with (solid lines) high analyte excess ratio (γ = 100) 0.0833 mM [$Fc(MeOH)_2$] and 8.33 mM of (square points) cysteine, (circular points) glutathione;
(dotted lines) 0 mM thiol and 0.5 mM [$Fc(MeOH)_2$];
Electrolyte: $Bis-tris$ 0.1 M + $NaCl$ 0.1 M; ν=10 mV s^{-1}
(Value of i_c measured at E = 0.45 V)

conditions which allow us to be in a steady state condition (Zone *KS* from figure 3.6). As discussed earlier in section 3.4, at the steady state condition, we eliminate the effect of diffusion of $\mathrm{Fc(MEOH)_2}$ and the analyte towards the electrode for the chemical reaction, making the calculation of rate kinetics simpler. In order to achieve a steady state behaviour for the system, it requires us to have a larger value of γ and a lower value of λ (but not too low as well, otherwise we enter zone *KD* and start observing diffusion effects).
Thus, for our experimental conditions, we choose γ = 100 with a final $\mathrm{Fc(MeOH)_2}$ concentration of 0.0833 mM and cysteine concentration of 8.33 mM. We have kept the scan rate at 10 mV s^{-1} which gives us $\lambda = 6.14 \times 10^{-2}$ ($\log \lambda$ = -1.212).
From figure 4.9, we can observe that the cyclic voltammogram for these experimental conditions shows a steady state behaviour for these systems and the plateau current (i_{ss}) can be used to directly compare the kinetics of the given systems. However, since we observe an accumulation of the cationic form of $\mathrm{Fc(MeOH)_2}$ inside the negatively charged silica mesochannels, it is difficult to calculate the exact value of the redox probe present at the electrode surface, hence making it difficult to calculate the rate constant for MSTF deposited electrodes.
The scan rate with this experimental condition was also varied from 10 mV s^{-1} to 1000 mV s^{-1} and is plotted against the steady state current in figure 4.10. As can be seen from the plot, the steady state current at this condition is independent of scan rate in this range. This, in turn, means that at these conditions, the electrochemical response is not limited by the diffusion of the species from the bulk to the electrode. The forward peak current of 0.5 mM $\mathrm{Fc(MeOH)_2}$ in absence of cysteine at the two electrodes has also been plotted as dashed lines for reference.

As can be observed from figure 4.9a, the steady state current for the system with cysteine has decreased by 29.2 %* on introduction of MSTF at the ITO electrodes, whereas the steady state current for the system with glutathione remains unchanged (or negligibly smaller). This can be contributed to the slower rate kinetics (k_{obs}) for the EC' mechanism with glutathione oxidation as was observed with bare ITO in section 3.4. The smaller rate kinetics result in the system being unaffected by the presence or absence of mesoporous silica thin films as any diffusion resulting from the mesochannels did not limit the chemical reaction. However, for the cysteine oxidation, the k_{obs} at bare ITO was 3.6 times higher than glutathione, and presence of mesochannels visibly affected the rate kinetics.

*current measured at 0.45 V

4.3.4 Homocysteine oxidation at mesoporous silica thin films

As already stated earlier, Homocysteine has a very similar structure to cysteine but a slightly larger size, which is intermediate to cysteine and glutathione. We can observe from the cyclic voltammogram at bare ITO and mesoporous silica thin film (figure 4.11) that homocysteine oxidizes in a similar way through EC′ mechanism as cysteine or glutathione. From the cyclic voltammogram at bare ITO and MSTF (figure 4.11), we can observe that the steady state current for bare ITO is higher than MSTF, as has been observed earlier for other aminothiols. However, we can also observe that the steady state current is higher for

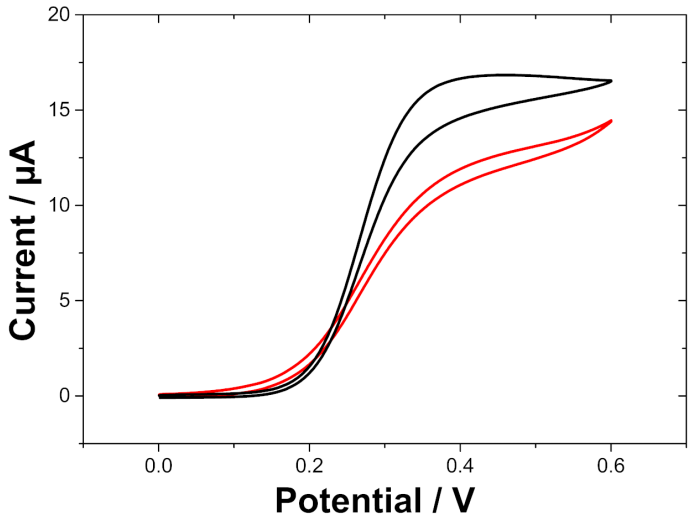

FIGURE 4.11: Cyclic voltammetry with 0.0833 mM $Fc(MeOH)_2$ and 8.333 mM homocysteine (γ=100) at (black) bare ITO electrode and (red) mesoporous silica thin film modified ITO electrode; Electrolyte = $Bis-tris$ 0.1 M + $NaCl$ 0.1 M; ν= 10 mV s^{-1}; pH = 6.5

homocysteine for both the types of electrodes in comparison to cysteine and glutathione, indicating a higher reaction rate with $Fc(MeOH)_2$, as has been already discussed earlier in section 3.3.2.

4.3.5 Mesoporous silica with pores blocked with CTA^+ molecules

The cyclic voltammogram at mesoporous silica thin film with blocked pores for a few redox probes has already been seen in figure 4.1. Out of these probes, $Fc(MeOH)_2$ (figure 4.1c) shows an interesting behaviour. Since, it has a neutral overall charge and is lipophilic, it is possible for $Fc(MeOH)_2$ to solubilize and permeate through the CTA^+ layer and react at the electrode while the other charged probes are not able to permeate through the film with the surfactant molecule present in the pores.

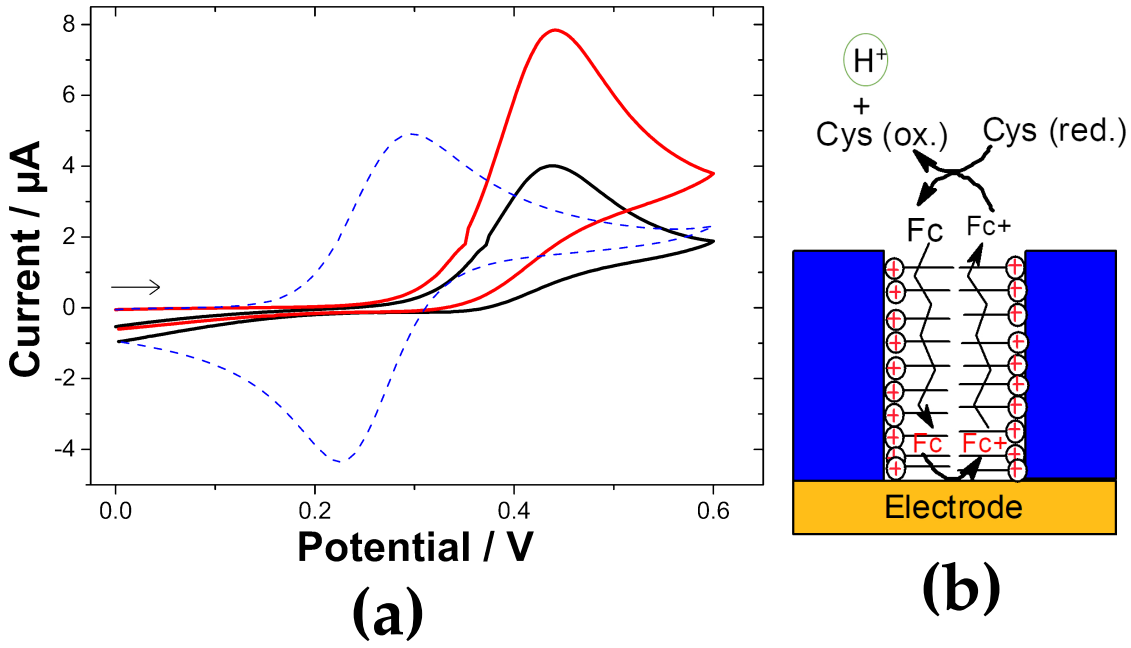

FIGURE 4.12: (a) Cyclic voltammetry at a mesoporous silica film modified ITO electrode with pores blocked by CTA^+. CV with 0.5 mM $Fc(MeOH)_2$ in the absence (black curve) and presence (red curve) of 0.1 mM cysteine; dashed blue line represents the CV with only 0.5 mM $Fc(MeOH)_2$ after extraction of CTA^+ from the meso-pores; Electrolyte: $Bis-tris$ 0.1 M + NaCl 0.1 M; ν= 10 mV s^{-1}. (b) Schematic of electrochemical oxidation of cysteine mediated by ferrocene at MSTF with pores blocked by CTA^+

The cysteine oxidation reaction with silica mesoporous film where the pores are blocked with the surfactant molecules give us a different perspective of the diffusion phenomena as well (figure 4.12a and figure 4.13).

In our experimental procedure, we used the films with the meso-pores blocked with CTA^+. We already know that the diffusion of $Fc(MeOH)_2$ is possible through its solubilization in the CTA^+ layer. Since, cysteine does not have any lipophilic chains and is negatively charged at pH 6.5 (pI = 5.14), we assume that cysteine cannot solubilize in the CTA^+ layer and diffuse through it.

The cyclic voltammogram at the films blocked with CTA^+ shown in figure 4.12a shows a behaviour which has been observed earlier with $Fc(MeOH)_2$ in section 4.2 at electrochemical characterization of MSTF. The oxidation peak current is observed at a higher anodic potential while we don't observe a reduction current peak. $Fc(MeOH)_2$ diffuses through the surfactant layer and oxidises at the electrode, but as soon as it is converted to its oxidised form, it gains a net positive charge and due to electrostatic repulsion experienced in the CTA^+ layer, it is expelled from the thin film layer. Thus, at the reverse scan, we don't have enough oxidized $Fc(MeOH)_2$ molecules available at the electrode surface to be

reduced and produce sufficient cathodic current. Now, since there is no availability of either the $Fc(MeOH)_2^+$ or cysteine inside the mesochannels, we are confident to assume that the chemical oxidation of cysteine takes place outside the mesochannels of the MSTF with the diffusion of $Fc(MeOH)_2$ taking place through the mesochannels to transfer electron at the electrode. A schematic of the system can be seen in figure 4.12b.

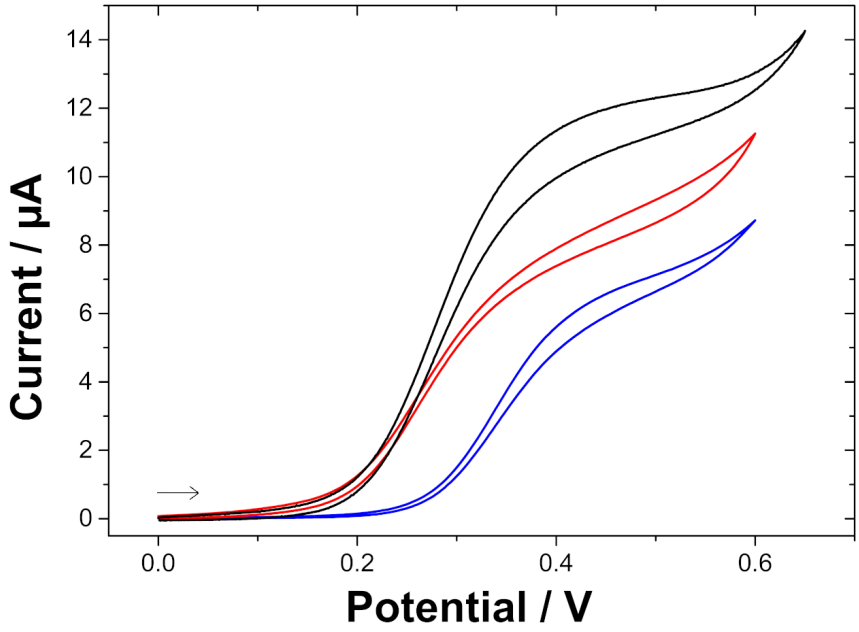

FIGURE 4.13: Comparison of electrodes at high excess ratio (γ = 100); [Cysteine]=8.333 mM, [$Fc(MeOH)_2$]= 0.0833 mM. (black) bare ITO, (red) mesoporous silica film, (blue) mesoporous silica film with CTAB in pores; Electrolyte: $Bis-tris$ 0.1 M + $NaCl$ 0.1 M; $\nu = 10\,mV\,s^{-1}$

Further, we can observe from the results in fig. 4.13, that even at higher excess ratio of cysteine (γ = 100), $Fc(MeOH)_2$ oxidizes at a higher anodic potential in case of MSTF with blocked pores (blue) in contrast to that with open pores (red curve) and at bare ITO (black curve), owing to the difficulty of the counter ions to diffuse into the film with CTA^+ molecules and maintain the charge neutrality [171]. The CV trend looks very similar to the others, but the current is smaller, indicating that the reaction is somehow limited. Since, in this case, the cysteine molecules can not diffuse through the CTA^+ layer, we have limited the diffusion to only $Fc(MeOH)_2$ molecules, and the chemical oxidation of cysteine is limited outside the mesochannels. We can interpret that the reaction limitations arise due to no diffusion of cysteine molecules towards the electrode, and the extra reaction time required for the diffusion of $Fc(MeOH)_2$ through the surfactant layer,

towards and away from the electrode, before it can react with cysteine at the MSTF-solution interface.

Another factor affecting the electrochemistry would be the absence of adsorbed ferrocenium molecules ($Fc(MeOH)_2^+$) at the silica walls. These adsorbed ferrocenium molecules influence the kinetics of the reaction inside the pores of the mesoporous film as it directly results in an increase in the concentration density of the catalyst in the vicinity of the electrode, and given there is no possibility at a surfactant blocked porous electrode to host adsorption of these molecules, we can expect a lower catalytic response and a lower resulting oxidation current. But, since the concentration of $Fc(MeOH)_2$ used in this system is very small (0.0833 mM), we can assume this effect to be smaller and of lesser consideration than the other.

Thus, it is apparent that cysteine diffusion also plays an important role in this reaction and due to its non-availability at the electrode inside the mesochannels, the chemical reaction takes place outside the mesochannels. This results in the decrease in the plateau current, i_{ss}, directly affecting the overall rate of reaction, k_{obs} as well. Thus, we can conclude for this result that, since the $Fc(MeOH)_2$ molecule diffusion in films is possible even in the presence of the surfactant molecule, the lack of diffusion of cysteine causes this change in the electrochemical behaviour.

4.4 Ferrocene-functionalized mesoporous silica thin films modified ITO electrode

In order to prepare ferrocene-functionalized mesoporous silica thin films, co-deposition of TEOS molecule was done with AzPTES (AzPTES : TEOS = 0.3:0.7) as mentioned in section 2.4.1. These electrodes were extracted of the surfactant molecule and then functionalized with ferrocene through azide-alkyne Huisgen cycloaddition reaction (section 2.4.3). These ferrocene-functionalized mesoporous silica thin films give response by transfer of electron with the electrode through electron hopping mechanism (figure 4.14) and are useful for reagent-free detection of molecules at the electrode [174, 298].

4.4.1 Thiol oxidation at ferrocene functionalized MSTF

Ferrocene functionalized mesoporous silica thin films are very interesting for sensing applications as the ferrocene molecule has been immobilized in the pores of the mesopores and since, the redox species are not mobile in this system, the

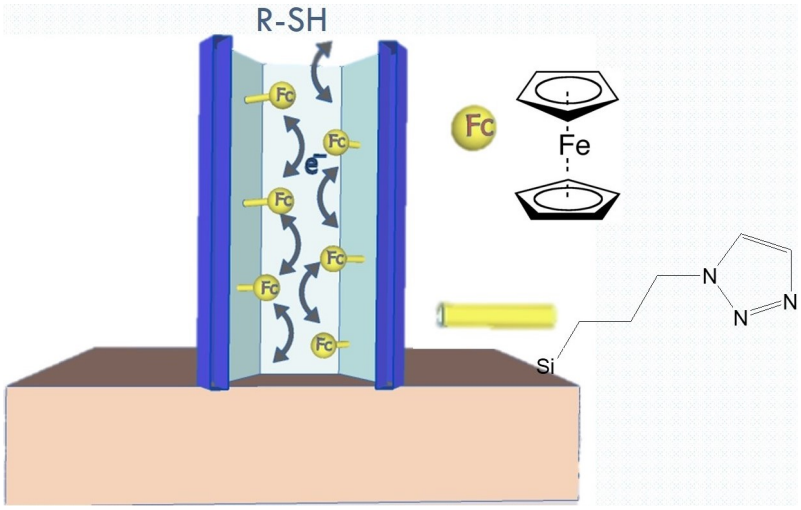

FIGURE 4.14: Mechanism of electron hopping at ferrocene functionalized MSTF

transfer of electrons from all the ferrocene molecules to the electrode is not direct but takes place through electron hopping mechanism where the electrons are transferred from one molecule to another so as to reach the electrode (or away from the electrode in the case of reduction) as shown in figure 4.14 [298].

The cyclic voltammogram at a ferrocene functionalized mesoporous silica thin film for the additions of cysteine and glutathione can be seen in figure 4.15a and figure 4.15b respectively. From the cyclic voltammograms, it can be clearly seen that the ferrocene functionalized mesoporous silica thin films are selective towards detection of cysteine and not glutathione. At addition of 196 µM and 281 µM of cysteine [†] in figure 4.15a, we see a increase in the peak current which is absent in case of glutathione in figure 4.15b. Since, all the conditions are the same for both the systems, we can interpret with this result that the electrode is selective towards oxidation of cysteine over glutathione.
We already know that due to the small pore size, electrodes modified with mesoporous silica can exhibit selectivity towards molecules of smaller size [169]. The concentration of AzPTES used for the deposition of the MSTF is 30 % and results in a good quality film with large number of sites available for ferrocene functionalization. At the AzPTES of 30 %, it was reported to provide resistance to mass diffusion to molecular species as a result of higher filling of the pores [165, 298]. The size constraint in a mesopore along with the high density of azide molecules and ferrocene moieties present inside the mesopores hinder the diffusion of larger molecule of glutathione while cysteine being a smaller molecule is easily able to

[†]final concentration is accounted for the dilution in the cell

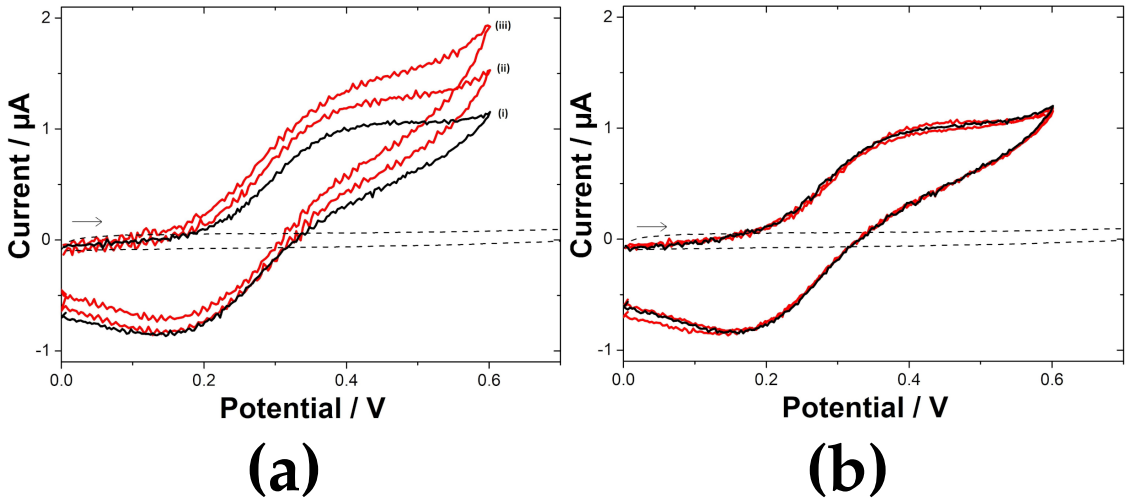

FIGURE 4.15: Cyclic Voltammetry at ferrocene functionalized MSTF with (i) 0 µM (ii) 196 µM (iii) 281 µM (a) **Cysteine** (b) **Glutathione**; Electrolyte = Bis − tris 0.1 M + NaCl 0.1 M; pH = 6.5; ν = 10 mV s^{-1}.

diffuse inside the pores to react with ferrocene. This further validates the size selective property of mesoporous silica.

4.4.1.1 Cyclic Voltammetry in a flow cell system

The flow cell system as discussed earlier in section 2.2.3 allows us to flow a solution over an electrode in a controlled manner. This type of convection cell pro-

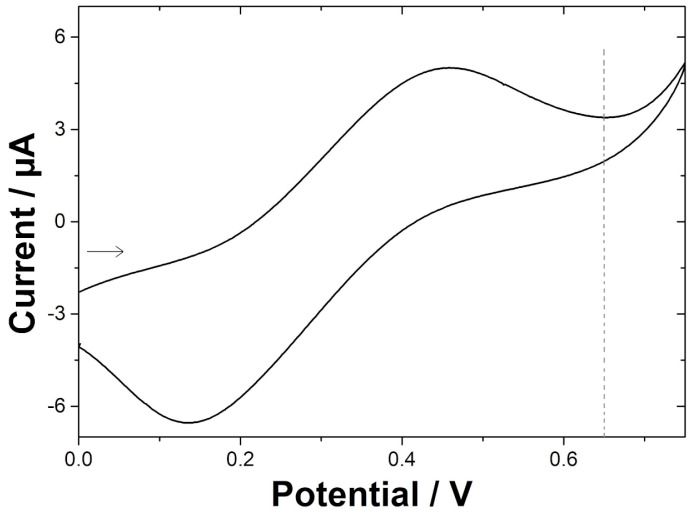

FIGURE 4.16: Cyclic voltammetry in flow cell at ferrocene functionalized MSTF electrode; Electrolyte = Bis − tris 0.1 M + NaCl 0.1 M; pH = 6.5; ν=10 mV s^{-1}. The dashed line represents the anodic potential of 0.65 V used for chronoamperometry experiments.

vides higher sensitivity while keeping the noise lower, in comparison to the conventional methods of convection like stirring. Along with this, the system allows the injection of a different solution at any required time interval during the experimentation phase.
In order to obtain the cyclic voltammogram at a ferrocene-functionalized mesoporous silica thin film electrode, we passed the electrolyte solution over the electrode and paused the flow to avoid the effects of convection. The cyclic voltammogram at the electrode can be seen in figure 4.16. From the cyclic voltammogram, the oxidation and reduction peaks characteristic of a ferrocene molecule can be clearly observed at 450 mV and 140 mV respectively. It should be noted that a higher peak separation is observed due to increased resistance to ionic transport due to presence of ferrocene molecules in the silica pores.

4.4.2 Chronoamperometry in a Flow Injection system

Chronoamperometry was done at a ferrocene functionalized mesoporous silica thin film in order to detect the thiol molecules. The flow of the electrolyte over the electrode was maintained at 1 mL min^{-1}. This flow rate had earlier been optimized in a previous work [174]. A potential of 0.65 V was applied to oxidise the ferrocene moieties immobilised in the mesopores. The applied potential was determined after recording the CV of the modified electrode in the flow cell as mentioned in the last section (figure 4.16). The system was flushed before the experimentation with DI water and then with the electrolyte solution for 2 to 3 min, so as to remove any impurity accumulated in the tubes or the flow-cell. During injection of a solution through the system, care was taken to make sure the injection sample was bubble-free.

4.4.2.1 Selective detection of Cysteine over Glutathione at ferrocene functionalized MSTF

Apart from cyclic voltammetry, we also see in figure 4.17 the chronoamperogram for the injection of 50 µM of glutathione (red arrows) and of cysteine (black arrows).

When the thiol analyte was injected in the flow cell, a rise in current was observed, which was the result of the electron transfer from the analyte to the ferrocenium and causing the re-oxidation of ferrocene. For glutathione, the current recorded by $\sim$ 10 nA for a noise around 14 nA. The signal to noise ratio calculated from figure 4.17 was lower than 1 while a species is considered to be statistically

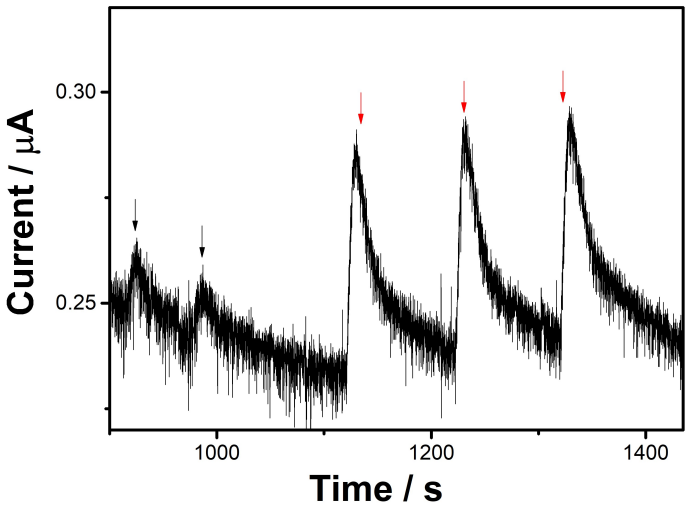

FIGURE 4.17: Chronoamperograms showing the flow injection analysis of 50 µM of glutathione(black arrows) and of cysteine(red arrows) at ferrocene functionalized MSTF. $E_{applied}$= 0.65 V; Flow rate = 1 mL min^{-1} ; Electrolyte = Bis − tris 0.1 M + NaCl 0.1 M; pH = 6.5

detectable if the signal to noise ratio is greater than 3. When the same concentration of cysteine (50 µM) was injected in the flow injection analysis system, the current measured rose to 53 nA, which gave a signal to noise ratio greater than 3, confirming the idea of a good selectivity for cysteine over glutathione as previously suggested from CV experiments (figure 4.15) as well.

Figure 4.18a shows the sensitivity of the electrode towards cysteine detection. The peak current increased linearly (i_{peak} = 1.28 × 10^{-3} [Cys] + 1.39 × 10^{-2}, R^2 = 0.988) with the concentration of cysteine injected, which ranged from 3 to 20 µM. Over the 20 to 100 µM concentration range, the slope of the calibration curve dropped to 0.68 × 10^{-3} A M^{-1}. Despite a large background noise originating from the flow cell, a good repeatability of the peak current was observed with a relative standard deviation for the measurements of 3-12%.

In the case of flow injection chronoamperograms in figure 4.19 at ferrocene functionalized mesoporous silica thin film, we observe that the current for homocysteine is very low in comparison to that of cysteine (but still higher than glutathione). Here, it should be noted that we have taken very high concentration of the analytes (10 mM). From the chronoamperograms we can observe, that, even with the higher reaction rate of homocysteine in comparison to that of cysteine and glutathione, as observed earlier in section 3.4, we are still limited by the size of the molecule which directly influences the diffusion of the molecule inside the pores. The size of the homocysteine being intermediate to cysteine

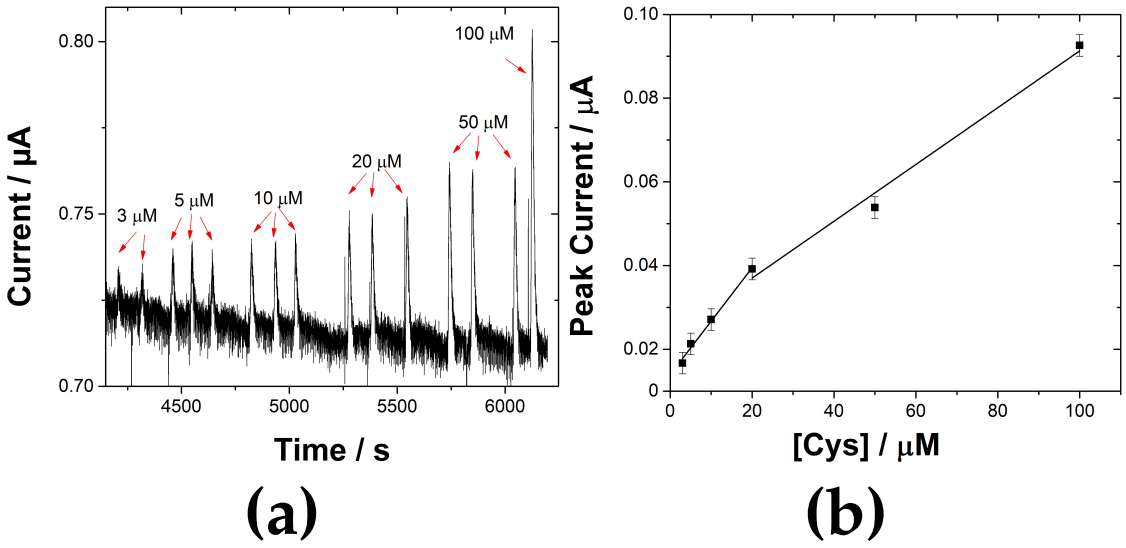

FIGURE 4.18: (A) Chronoamperograms obtained for increasing concentrations of cysteine (3 - 100 µM). $E_{applied}$ = 0.65 V; Electrolyte = Bis − tris 0.1 M + NaCl 0.1 M; flow rate = 1 mL min^{-1}. (B) Calibration curve with peak current as a function of cysteine concentration.

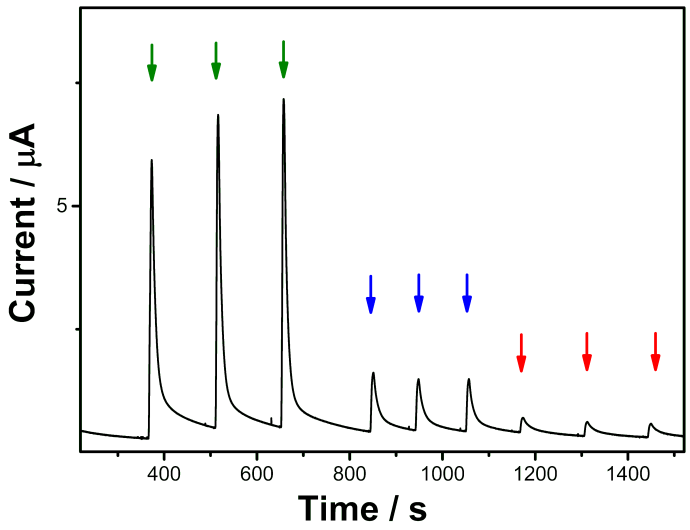

FIGURE 4.19: Chronoamperograms showing the flow injection analysis of 10 mM of cysteine(green arrows), homocysteine (blue arrows) and of glutathione (red arrows) at ferrocene functionalized MSTF. $E_{applied}$= 0.65 V; flow rate = 1 mL min^{-1} ; Electrolyte = Bis − tris 0.1 M + NaCl 0.1 M; pH = 6.5

and glutathione shows a current response, which is intermediate to these thiol groups. Thus, this result further validates the size selective behaviour of thiol oxidation at ferrocene functionalized mesoporous silica thin films. The analytical performances of the mesoporous silica film functionalized with ferrocene compared well with the modified electrodes already reported in the literature (discussed in Table 4.1 on page 90) [264–266, 268, 270, 271, 273–276]. The different methods given in this table give a summary of the reported methods for the thiol molecules using various electroanalytical methods like cyclic and square wave voltammetry, chronoamperometry and flow injection analysis. The sensitivity and the limit of detection is comparable to other methods. The method described with this work is repeatable and allows for reagent free detection of cysteine. The other prospects of the method lies in the different functionalization possibilities of mesoporous silica allowing for a prospective detection methodology for a variety of organic and inorganic species [161, 165, 166, 196–200].

TABLE 4.1: Analytical performances reported for cysteine concentration determination by electrochemical means

Electrode Material	**Redox Mediator**	**Electrochemical Method**	**Detection potential**	**pH**	**Sensitivity** ($A\,M^{-1}$)	**LOD** (µM)	**Reference**
Mesoporous silica film	Ferrocene	CA-FIA	+0.65 V (vs Ag/AgCl)	6.5	1.3×10^{-3}	3.0	This work
Graphite	Nitrosophenyl	SWV	−0.10 V (vs SCE)	7	3.7×10^{-2}	7.0	[264]
GC	Quinone	CV	+0.14 V (vs SCE)	7	7.5×10^{-3}	5.0	[265]
GC	Quinone	SWV	+0.12 V (vs SCE)	3	5.0×10^{-2}	4.0	[266]
CTC-GC	Catechol	CV	+0.10 V (vs SCE)	7	2.3×10^{-2}	0.6	[268]
SPE	PEDOT	CA-FIA	+0.65 V (vs Ag/AgCl)	6	5.3×10^{-2}	0.03	[270]
Au NP-SPE	PEDOT	CA-FIA	+0.55 V (vs Ag/AgCl)	2-8	1.1×10^{-1}	0.05	[271]
GC	Caffeic Acid	CV	+0.18 V (vs SCE)	7	4.9×10^{-3}	99.0	[273]
CNT-GC	P4VP- $Fe(CN)_5$	CA	+0.15 V (vs SCE)	7	1.0	0.006	[274]
Ormosil	Pyrroloquinoline quinone	CA	−0.20 V (vs Ag/AgCl)	8.5	1.1×10^{-2}	0.5	[276]
GC	Brilliant blue	CA	+0.90 V (vs Ag/AgCl)	1.5	1.1×10^{-1}	0.5	

LOD: Limit of detection; GC: *Glassy Carbon*; CNT-GC: *Carbon nanotube*-modified *glassy carbon*; SPE: Screen-printed electrode; Au NP-SPE: Screenprinted electrode modified with *Au* nanoparticles; PEDOT: *poly(3,4ethylenedioxythiophene)*; P4VP-$Fe(CN)_5$: *poly(4-vinylpyridine)* functionalised with

$Fe(CN)_5$; SWV: Square Wave Voltammetry; CV: Cyclic Voltammetry; CA-FIA: Chronoamperometry - Flow Injection Analysis; CA: Chronoamperometry; SCE: Saturated Calomel Electrode.

4.5 Conclusion

Vertically oriented mesoporous silica thin films were deposited on ITO electrode using electrochemically-assisted self method and were characterized using different types of electrochemical probes, TEM imaging, and GISAXS characterization. The oxidation of cysteine, glutathione and homocysteine at MSTF was mediated electrochemically using ferrocenedimethanol ($\mathrm{Fc(MeOH)_2}$) following the EC' mechanism. The EC' mechanism for oxidation of cysteine at MSTF showed a dependence on scan rate and the behaviour observed at changing the scan rate was similar to that observed at bare ITO. At lower scan rates, we observe the effect of the EC' mechanism, which gets limited upon increasing the scan rate as the kinetics are limited by the time given for the transfer of electron from cysteine to the $\mathrm{Fc(MeOH)_2^+}$ molecule.

However, at an excess ratio, γ, equal to 100, we observed that the steady state current was reached and for cysteine it was lowered from 11.11 µA[‡] at bare ITO to 7.97 µA[‡] at MSTF, while the steady state current for glutathione remained similar (or negligibly smaller). The lower electrochemical response for cysteine comes from the diffusion limitation of species through the mesochannels, but since the rate kinetics of glutathione oxidation were already very slow for bare electrode, the presence of mesochannels do not limit it's overall electrochemical response.

We studied the EC' mechanism for the electrochemical oxidation of cysteine at mesoporous silica with $\mathrm{CTA^+}$ in pores. Since, cysteine cannot diffuse through the positively charged $\mathrm{CTA^+}$ layer and there is no accumulation of $\mathrm{Fc(MeOH)_2^+}$ inside the mesochannels, we limit the reaction outside the MSTF with only the diffusion of $\mathrm{Fc(MeOH)_2}$ taking place through the mesochannels. These limitations effect the electrochemical response of the system and we observe a decrease in the steady state current at the cyclic voltammogram. This experiment brought us to the conclusion that the diffusion of both species is necessary for a higher catalytic response and any hindrance to this diffusion of species directly resulted in lowering of the apparent kinetics of the oxidation mechanism.

The effect of diffusion in mesochannels was further reinforced by the experiments with electrochemical impedance spectroscopy. The results from EIS at MSTF confirmed that the reaction rate for cysteine oxidation following EC' mechanism are similar to those at bare ITO and a diffusion resistance component for diffusion of species through mesochannels can be observed for MSTF results. This result

[‡]steady state current measured at 0.45 V

further explains the lowering of the k_{obs} for the oxidation of cysteine at MSTF deposited ITO electrodes.

The higher electron transfer rate kinetics for oxidation of cysteine in comparison to glutathione at ITO electrodes, along with the mass transfer limitation of glutathione through mesochannels, was used for introducing selectivity at MSTF electrodes. This was exploited at ferrocene functionalized MSTF on ITO electrodes for reagent-free detection of cysteine over glutathione. This was demonstrated by cyclic voltammetry in a 3-electrode cell, and then by amperometry in a flow injection analysis mode. Experimentally, the lowest concentration of cysteine detected was 3 µM and the sensitivity was measured to be 1.28 mA M^{-1} and 0.68 mA M^{-1} for 3 to 20 µM and 20 to 100 µM respectively, in flow injection analysis mode.

General Conclusions

In the course of this thesis, we have investigated the electrochemical oxidation of cysteine, glutathione and homocysteine at bare ITO and vertically oriented mesoporous silica thin films coated ITO using $\mathrm{Fc(MeOH)_2}$ following EC' mechanism. The EC' mechanism for the given electrochemical reaction shows dependence on the concentration of the catalyst and the analyte, and the scan rate of the CV measurement.

A general schematic of the kinetic zone diagram was introduced and the different regions of the kinetic zone depicting different levels of the electrochemical oxidation were accessed at the electrodes. Variation in scan rate from $10\,\mathrm{mV\,s^{-1}}$ to $1000\,\mathrm{mV\,s^{-1}}$ for the electrochemical oxidation of cysteine revealed that the catalytic oxidation reaction was directly dependent on the scan rate of the CV measurement. The ratio i_f/i_r was observed to be higher for the slowest scan rate and decreased to a value close to 1 at the highest scan rate indicating that the electrochemical oxidation of cysteine is limited by the slower electron transfer between cysteine and $\mathrm{Fc(MeOH)_2}$ molecules. A direct dependency of i_f/i_r ratio was observed on analyte concentration and the scan rates.

The effect of the presence and the type of buffer was observed and on comparison of two buffers, (viz. bis-tris and phosphate buffer), bis-tris was found to have better efficiency at the electrochemical reaction.

The observable rate kinetics at bare ITO for the oxidation of cysteine , glutathione and homocysteine using $\mathrm{Fc(MeOH)_2}$ following EC' mechanism were calculated to be $(7.9 \pm 0.2)\,\mathrm{s^{-1}}$, $(2.2 \pm 0.1)\,\mathrm{s^{-1}}$ and $(16.8 \pm 0.1)\,\mathrm{s^{-1}}$ respectively. However, at MSTF coated ITO electrodes, we observed a lowering of the steady state current for cysteine, directly affecting the k_{obs} of the electrochemical oxidation process, but was not lowered for glutathione. This was explained by the already low rate kinetics of glutathione oxidation which was indeed the rate limiting step, unaffected by the presence or absence of mesoporous silica thin films. The 3.6 times higher k_{obs} value of cysteine was harnessed at ferrocene functionalized MSTF on ITO electrodes for selective detection of cysteine over glutathione. Combined

with the mass diffusion limitations at ferrocene functionalized MSTF, we demonstrated the reagent-free detection of cysteine through cyclic voltammetry in a 3-electrode cell and then by amperometry in a flow injection analysis mode. Experimentally, the lowest concentration of cysteine detected was 3 µM and the sensitivity was measured to be 1.28 mA M^{-1} and 0.68 mA M^{-1} for concentrations of 3 to 20 µM and 20 to 100 µM respectively, in flow injection analysis mode.

At mesoporous silica thin films with CTA^+ present in the pores, we observed a lower electrochemical response. Since, only the lipophilic molecular species, i.e., $Fc(MeOH)_2$ can solubilize in the CTA^+ layer, and the other molecular species (i.e. the analyte and buffer) are excluded from diffusing through the CTA^+ filled mesochannels, we can predict that the chemical reaction happens outside the mesopores in this system with only the diffusion of $Fc(MeOH)_2$ taking place through the CTA^+ layer. Thus, the only reason for the observed lower electrochemical response from this system would be the absence of diffusion of cysteine through the CTA^+ layer. This brings us to conclusion that the diffusion of cysteine in mesochannels plays a role and that the absence of cysteine diffusion in the mesochannels limits the overall electrochemical reaction. This result was further supplemented by electrochemical impedance spectroscopy results which described that the electrochemical reaction rates at both bare ITO and MSTF electrodes were similar, but a diffusion resistance component was present for the latter. These two results confirmed the strong significance of the diffusion of both the catalyst and the analyte species at the electrode.

Next, we focussed on development of microelectrodes, and successfully fabricated ITO microelectrodes in-house using a novel approach, followed by MSTF deposition. However, crack-free and uniform ITO microelectrodes proved challenging to fabricate resulting in a non-uniform MSTF deposition, forcing us to shift our focus on carbon- based microelectrodes. Good quality and reproducible glass-encapsulated carbon fibre ultramicroelectrodes of radius (5.5 ± 2.4) µm were fabricated by careful monitoring of the process and they were characterized electrochemically and micrographed using an optical microscope.

In order to deposit MSTF on these carbon UMEs, $APTES$ modification proved to be imperative. The modification process of carbon UMEs with $APTES$ was optimised at 2 cyclic voltammetry cycles at 100 mV s^{-1} in 0.1 mM $APTES$. Mesoporous silica was then successfully deposited on these $APTES$ modified carbon UMEs through EASA method by an application of a constant potential of -2 V for a fixed duration of 20 s. Co-deposition of silica with $AzPTES$ was successfully performed for $AzPTES$ concentrations of 5 % and 10 % in the sol and the $AzPTES$

modified films were further functionalized with $\mathrm{ethynylferrocene}$ through $\mathrm{copper(I)}$ catalysed *Huisgen alkyne-azide cycloaddition reaction*. On electrochemical characterization of these ferrocene functionalized MSTF coated carbon UMEs with a blank electrolyte solution of 0.1 M KCl, we observe a diffusion-controlled, peak-shaped cyclic voltammogram with increasing forward and reverse current peaks for higher scan rates. These ferrocene-functionalized carbon UMEs can prove to be potential candidates for sensitive detection of molecular species as they combine.

This work explores further the possibility to employ mesoporous silica thin films for detection of molecules by the function of difference in sizes and reaction rates, and this methodology can be of prospect to detect other molecules of analytical interest at mesoporous silica modified electrodes. The different parameters for detection of cysteine at mesoporous silica thin films have been considered and the study describes the diffusion effect of species through mesochannels. This work can be used as an example for study of EC' mechanism at such modified electrodes. Further, the fabrication and characterization of ITO and carbon microelectrodes, and their modification with mesoporous silica holds high prospects in electroanalytical chemistry due to combination of their various established advantages. Microelectrodes are known for their small size, high sensitivity, high diffusion, faster response, low-electrolyte requirements, etc., while mesoporous silica provide advantages such as electrode protection, molecular sieving, cation accumulation resulting in enhanced electrochemical and electrochemiluminescence response, genosensor, etc. The combination of both the systems with mesoporous silica modified microelectrodes holds good potential in a variety of fields.

Conclusions Générales

Au cours de cette thèse, nous avons étudié l'oxydation électrochimique de la cystéine, du glutathion et de l'homocystéine au niveau de l'ITO nu et des films minces de silice mésoporeuse orientés verticalement déposés sur l'ITO en utilisant le $\mathrm{Fc(MeOH)_2}$ comme médiateur dans un mécanisme EC'. Le mécanisme EC' pour la réaction électrochimique concernée montre une dépendance de la concentration du catalyseur et de l'analyte, et de la vitesse de balayage sur la mesure CV.

Un schéma général du diagramme de la zone cinétique a été introduit et les différentes régions de la zone cinétique représentant les différents niveaux de l'oxydation électrochimique ont été observées aux électrodes. La variation de la vitesse de balayage de $10\,\mathrm{mV\,s^{-1}}$ à $1000\,\mathrm{mV\,s^{-1}}$ pour l'oxydation électrochimique de la cystéine a révélé que la réaction d'oxydation catalytique dépendait directement de la vitesse de balayage de la mesure CV. Le facteur i_f/i_r a été observé comme étant plus élevé pour la vitesse de balayage la plus lente et a diminué à une valeur proche de 1 à la vitesse de balayage la plus élevée, ce qui indique que l'oxydation électrochimique de la cystéine est limitée par le transfert d'électrons plus lent entre la cystéine et les molécules de $\mathrm{Fc(MeOH)_2}$. Une dépendance directe du facteur i_f/i_r a été observée par la concentration de l'analyte et les vitesses de balayage.

L'effet de la présence et du type de tampon a été observé et lors de la comparaison de deux tampons, le bis-tris et le buffer de phosphate, le bis-tris s'est trouvé avoir une meilleure efficacité à la réaction électrochimique.

Les cinétiques de taux observables à l'ITO nu pour l'oxydation de la cystéine, du glutathion et de l'homocystéine en utilisant le $\mathrm{Fc(MeOH)_2^+}$ par le mécanisme EC' ont été calculées comme étant $(7{,}9 \pm 0{,}2)\,\mathrm{s^{-1}}$, $(2{,}2 \pm 0{,}1)\,\mathrm{s^{-1}}$ et $(16{,}8 \pm 0{,}1)\,\mathrm{s^{-1}}$ respectivement. Cependant, aux électrodes ITO déposées par le MSTF, nous avons observé une diminution du courant limite pour la cystéine, affectant directement les valeurs de k_{obs} du processus d'oxydation électrochimique, mais n'a pas été diminué pour le glutathion. Ceci s'explique par la cinétique déjà faible de l'oxydation du glutathion qui était en effet l'étape limitante du taux, non affectée par

la présence ou l'absence de films minces de silice mésoporeuse. La valeur 3,6 fois plus élevée de la cystéine a été exploitée au MSTF fonctionnalisé au ferrocène sur des électrodes ITO pour la détection sélective de la cystéine par rapport au glutathion. En combinaison avec les limitations de la diffusion de masse au MSTF fonctionnalisé au ferrocène, nous avons démontré la détection sans réactif de la cystéine par voltampérométrie cyclique dans une cellule à 3 électrodes, puis par ampérométrie dans un mode d'analyse par injection de flux. Expérimentalement, la plus faible concentration de cystéine détectée était de 3 µM et la sensibilité a été mesurée à 1,28 mA M^{-1} et 0,68 mA M^{-1} pour des concentrations de 3 à 20 µM et de 20 à 100 µM respectivement, en mode d'analyse par injection de flux.

Dans le cas des films minces de silice mésoporeuse avec CTA^+ présents dans les pores, nous avons observé une réponse électrochimique plus faible. Étant donné que seules les espèces moléculaires lipohiliques, soit $Fc(MeOH)_2$, peuvent se solubiliser dans la phase CTA^+ et que les autres espèces moléculaires ne peuvent pas se diffuser à travers les mésocanaux remplis de CTA^+, nous pouvons prédire que la réaction chimique se passe en extérieur des mésopores dans ce système, seule la diffusion de $Fc(MeOH)_2$ ayant lieu à travers la phase CTA^+. Ainsi, la seule raison de la réponse électrochimique inférieure observée dans ce système serait l'absence de diffusion de la cystéine à travers la phase CTA^+. Ceci nous amène à la conclusion que la diffusion de la cystéine dans les mésocanaux joue un rôle et que l'absence de diffusion de la cystéine dans les mésocanaux limite la réaction électrochimique globale. Ce résultat a été complété par les résultats de la spectroscopie d'impédance électrochimique qui ont décrit que les vitesses de réaction électrochimique aux électrodes ITO nues et MSTF étaient similaires, mais qu'une composante de résistance à la diffusion était présente pour la seconde. Ces deux résultats ont confirmé la forte signification de la diffusion du catalyseur et des analytes au niveau de l'électrode.

Ensuite, nous avons concentré nos efforts sur le développement de microélectrodes, et nous avons réussi à fabriquer sur place des microélectrodes ITO en utilisant une méthode nouvelle, suivie d'un dépôt de MSTF. Cependant, la fabrication de microélectrodes ITO sans fissures et homogènes s'est montrée difficile, ce qui a entraîné un dépôt de MSTF non homogène, nous obligeant à nous concentrer sur les microélectrodes à base de carbone. Des ultramicroélectrodes reproductibles et de bonne qualité en fibre de carbone encapsulée dans du verre, de rayon (5,5 $\pm$ 2,4) µm, ont été fabriquées en contrôlant soigneusement le processus et elles ont été caractérisées électrochimiquement et micrographiées à l'aide d'un microscope optique.

Pour déposer des MSTF sur ces UME de carbone, la modification d'APTES s'est avérée impérative. Le processus de modification des UME de carbone avec APTES a été optimisé à 2 cycles de voltampérométrie cyclique à 100 mV s^{-1} dans 0,1 mM APTES. On a ensuite déposé avec succès la silice mésoporeuse sur ces UMEs de carbone modifiées par APTES par la méthode de l'EASA en appliquant un potentiel constant de -2 V pendant une durée fixe de 20 s. La co-déposition de la silice avec l'AzPTES a été réalisée avec succès pour des concentrations d'AzPTES de 5 % et 10 % dans le sol et les films modifiés par l'AzPTES ont été fonctionnalisés avec de l'éthynylferrocène par une *réaction de cycloaddition de Huisgen alkyne-azide* catalysée par le cuivre(I). La caractérisation électrochimique de ces MSTF fonctionnalisés au ferrocène a déposé des UME au carbone dans une solution électrolytique à blanc de 0,1 M de KCl. Nous observons un voltampérogramme cyclique en forme de pic, contrôlé par diffusion, avec des pics de courant croissants en avant et en retour pour des vitesses de balayage plus élevées. Ces UME au carbone fonctionnalisées au ferrocène peuvent s'avérer des candidats potentiels pour la détection sensible de molécules.

Ce travail explore davantage la possibilité d'utiliser des films minces de silice mésoporeuse pour la détection de molécules par la fonction de différence de taille et de taux de réaction, et cette méthodologie peut être intéressante pour détecter d'autres molécules d'intérêt analytique aux électrodes modifiées de silice mésoporeuse. Les différents paramètres de détection de la cystéine dans les films minces de silice mésoporeuse ont été pris en compte et l'étude décrit l'effet de diffusion des molécules à travers les mésocanaux. Ce travail peut être utilisé comme un exemple pour l'étude du mécanisme de la EC' à ces électrodes modifiées. Ensuite, la fabrication et la caractérisation des microélectrodes ITO et carbone, et leur modification avec de la silice mésoporeuse offrent de nombreuses perspectives en chimie électroanalytique en raison de la combinaison de leurs différents avantages établis. Les microélectrodes sont connues pour leur petite taille, leur haute sensibilité, leur diffusion élevée, leur réponse plus rapide, leur faible besoin en électrolytes, etc., tandis que la silice mésoporeuse offre des avantages tels que la protection des électrodes, le tamisage moléculaire, l'accumulation de cations qui permet d'améliorer la réponse électrochimique et l'électrochimiluminescence, le génosenseur, etc. La combinaison de ces deux systèmes avec des microélectrodes modifiées à la silice mésoporeuse offre un bon potentiel dans divers domaines.

Bibliography

[1] D. Zhao, Y. Wan, and W. Zhou. *Ordered mesoporous materials*. John Wiley & Sons, 2012.

[2] P. Van Der Voort, D. Esquivel, E. De Canck, F. Goethals, I. Van Driessche, and F. J. Romero-Salguero. "Periodic mesoporous organosilicas: from simple to complex bridges; a comprehensive overview of functions, morphologies and applications". In: *Chemical Society Reviews* 42.9 (2013), pp. 3913–3955.

[3] A. Walcarius. "Silica-based electrochemical sensors and biosensors: recent trends". In: *Current Opinion in Electrochemistry* 10 (2018), pp. 88–97.

[4] F. Hoffmann, M. Cornelius, J. Morell, and M. Fröba. "Silica-based mesoporous organic–inorganic hybrid materials". In: *Angewandte Chemie International Edition* 45.20 (2006), pp. 3216–3251.

[5] J. Weitkamp. "Zeolites and catalysis". In: *Solid state ionics* 131.1-2 (2000), pp. 175–188.

[6] P. Laszlo. *Preparative chemistry using supported reagents*. Elsevier, 2012.

[7] R. Murry. "Molecular design of electrode surfaces". In: *Techniques of chemistry* 22 (1992).

[8] A. Walcarius. "Zeolite-modified electrodes: Analytical applications and prospects". In: *Electroanalysis* 8.11 (1996), pp. 971–986.

[9] A. Alberti, T. Armbruster, G. Artioli, C. Colella, E. Galli, J. D. Grice, F. Liebau, H. Minato, E. H. Nickel, E. Passaglia, et al. "Recommended nomenclature for zeolite minerals: Report of the subcommittee on zeolites of the International Mineralogical Association, Commission on New Minerals and Mineral Names". In: *The Canadian Mineralogist* 35 (1997), pp. 1571–1606.

[10] S. Li, J. Li, M. Dong, S. Fan, T. Zhao, J. Wang, and W. Fan. "Strategies to control zeolite particle morphology". In: *Chemical Society Reviews* 48.3 (2019), pp. 885–907.

[11] A. Walcarius. "Electroanalytical applications of microporous zeolites and mesoporous (organo) silicas: recent trends". In: *Electroanalysis: An International Journal Devoted to Fundamental and Practical Aspects of Electroanalysis* 20.7 (2008), pp. 711–738.

[12] D. R. Rolison. "Zeolite-modified electrodes and electrode-modified zeolites". In: *Chemical Reviews* 90.5 (1990), pp. 867–878.

[13] J. B. Higgins. "Silica zeolites and clathrasils". In: *Reviews in Mineralogy and Geochemistry* 29.1 (1994), pp. 507–543.

[14] M. E. Davis. "Zeolites and molecular sieves: not just ordinary catalysts". In: *Industrial & engineering chemistry research* 30.8 (1991), pp. 1675–1683.

[15] D. Breck. *Structure, Chemistry and Use of Zeolite Molecular Sieves*. 1st ed. Wiley, New York, 1974.

[16] D. W. Breck. *Zeolite molecular sieves: structure, chemistry and use*. 2nd ed. Krieger, 1984.

[17] A. Walcarius. "Implication of zeolite chemistry in electrochemical science and applications of zeolite-modified electrodes". In: *surfaces* 3 (2003), p. 6.

[18] E. Briot and F. Bedioui. "Electrochemistry of chemically modified zeolites and molecular sieves: review, examples and discussion". In: *Current Topics in Electrochemistry* 4 (1997), pp. 87–99.

[19] A. Walcarius. "Zeolite-modified electrodes in electroanalytical chemistry". In: *Analytica Chimica Acta* 384.1 (1999), pp. 1–16.

[20] D. R. Rolison and C. A. Bessel. "Electrocatalysis and charge-transfer reactions at redox-modified zeolites". In: *Accounts of Chemical Research* 33.11 (2000), pp. 737–744.

[21] D. R. Rolison. "The intersection of electrochemistry with zeolite science". In: *Studies in Surface Science and Catalysis*. Vol. 85. Elsevier, 1994, pp. 543–586.

[22] W. Li, Q. Yue, Y. Deng, and D. Zhao. "Ordered mesoporous materials based on interfacial assembly and engineering". In: *Advanced Materials* 25.37 (2013), pp. 5129–5152.

[23] A. Walcarius. "Electroanalysis with Pure, Chemically Modified and Sol-Gel-Derived Silica-Based Materials". In: *Electroanalysis: An International Journal Devoted to Fundamental and Practical Aspects of Electroanalysis* 13.8-9 (2001), pp. 701–718.

[24] C. Mousty and A. Walcarius. "Electrochemically assisted deposition by local pH tuning: a versatile tool to generate ordered mesoporous silica thin films and layered double hydroxide materials". In: *Journal of Solid State Electrochemistry* 19.7 (2015), pp. 1905–1931.

[25] V. Urbanova and A. Walcarius. "Vertically-aligned Mesoporous Silica Films". In: *Zeitschrift für anorganische und allgemeine Chemie* 640.3-4 (2014), pp. 537–546.

[26] F. Yan, X. Lin, and B. Su. "Vertically ordered silica mesochannel films: electrochemistry and analytical applications". In: *Analyst* 141.12 (2016), pp. 3482–3495. ISSN: 13645528.

[27] D. Everett. "Manual of symbols and terminology for physicochemical quantities and units, appendix II: Definitions, terminology and symbols in colloid and surface chemistry". In: *Pure and Applied Chemistry* 31.4 (1972), pp. 577–638.

[28] L. McCusker, F Liebau, and G Engelhardt. "Nomenclature of structural and compositional characteristics of ordered microporous and mesoporous materials with inorganic hosts (IUPAC Recommendations 2001)". In: *Pure and Applied Chemistry* 73.2 (2001), pp. 381–394.

[29] A. F. Cronstedt. *Rön och beskrifning om en obekant bärg art, som kallas Zeolites*. 1756.

[30] P. Venuto and J. Habib. "Fluid catalytic cracking with zeolite catalysts. 156 Marcel Dekker". In: *Inc New York* (1979).

[31] A. Galarneau, D. Mehlhorn, F. Guenneau, B. Coasne, F. Villemot, D. Minoux, C. Aquino, and J.-P. Dath. "Specific surface area determination for microporous/mesoporous materials: the case of mesoporous FAU-Y zeolites". In: *Langmuir* 34.47 (2018), pp. 14134–14142.

[32] D. Yates. "Studies on the surface area of zeolites, as determined by physical adsorption and X-ray crystallography". In: *Canadian Journal of Chemistry* 46.10 (1968), pp. 1695–1701.

[33] C. J. Plank. "The invention of zeolite cracking catalysts—a personal viewpoint". In: ACS Publications, 1983.

[34] R von Ballmoos, D. Harris, and J. Magee. *Catalytic Cracking in Handbook of Heterogeneous Catalysis. Vol. 4.(1997)*.

[35] J. Naber, K. Jong, W. Stork, and H. Kuipers. "Zeolites and Related Microporous Materials: State of the Art 1994". In: *Studies in Surface Science and Catalysis* 84.1994 (1994), p. 2197.

[36] J. Scherzer and A. J. Gruia. *Hydrocracking science and technology*. Crc Press, 1996.

[37] C. Plank, E. Rosinski, and W. Hawthorne. "Acidic crystalline aluminosilicates. New superactive, superselective cracking catalysts". In: *Industrial & Engineering Chemistry Product Research and Development* 3.3 (1964), pp. 165–169.

[38] M. Clough, J. C. Pope, L. T. X. Lin, V. Komvokis, S. S. Pan, and B. Yilmaz. "Nanoporous materials forge a path forward to enable sustainable growth: Technology advancements in fluid catalytic cracking". In: *Microporous and Mesoporous Materials* 254 (2017), pp. 45–58.

[39] S. Sie. "Isomerization reactions". In: *Handbook of Heterogeneous Catalysis* 4 (1997), pp. 1998–2017.

[40] F. G. Dwyer. "Catalysis of Organic Reactions". In: *Chemical Industries* 5 (1981), p. 39.

[41] W. W. Kaeding, G. C. Barile, and M. M. Wu. "Mobil zeolite catalysts for monomers". In: *Catalysis Reviews Science and Engineering* 26.3-4 (1984), pp. 597–612.

[42] N.-Y. Chen. *Shape selective catalysis in industrial applications*. Vol. 65. CRC press, 1996.

[43] P. B. Venuto. "Organic catalysis over zeolites: a perspective on reaction paths within micropores". In: *Microporous Materials* 2.5 (1994), pp. 297–411.

[44] M. Davis. "Zeolite-based catalysts for chemicals synthesis". In: *Microporous and mesoporous materials* 21.4-6 (1998), pp. 173–182.

[45] J. D. Sherman. "Synthetic zeolites and other microporous oxide molecular sieves". In: *Proceedings of the National Academy of Sciences* 96.7 (1999), pp. 3471–3478.

[46] A. J. Schwanke, R. Balzer, and S. Pergher. "Microporous and mesoporous materials from natural and inexpensive sources". In: *Handbook of Ecomaterials; Martínez, LMT, Kharissova, OV, Kharisov, B., Eds* (2017), pp. 1–22.

[47] P. Lainé, R. Seifert, R. Giovanoli, and G. Calzaferri. "Convenient Preparation of Close-Packed Monograin Layers of Pure Zeolite A Microcrystals." In: *ChemInform* 28.35 (1997), no–no.

[48] T.-W. Hui and M. D. Baker. "Ion exchange and electron transport at methyl viologen Y modified electrodes". In: *The Journal of Physical Chemistry B* 105.16 (2001), pp. 3204–3210.

[49] B. R. Shaw, K. E. Creasy, C. J. Lanczycki, J. A. Sargeant, and M. Tirhado. "Voltammetric response of zeolite-modified electrodes". In: *Journal of the Electrochemical Society* 135.4 (1988), p. 869.

[50] V Ganesan and R Ramaraj. "Mediated reduction of oxygen at poly (phenosafranine) modified electrodes". In: *Journal of applied electrochemistry* 30.6 (2000), pp. 757–760.

[51] A. Walcarius, L Lamberts, and E. Derouane. "The methyl viologen incorporated zeolite modified carbon paste electrode—part 1. Electrochemical behaviour in aqueous media. Effects of supporting electrolyte and immersion time". In: *Electrochimica acta* 38.15 (1993), pp. 2257–2266.

[52] Y. Jiang, M. Zou, K. Yuan, and H. Xu. "The electrochemical behavior of iron (III) incorporated in zeolite Y-modified electrode and the catalytic oxidation of ascorbic acid". In: *Electroanalysis: An International Journal Devoted*

to Fundamental and Practical Aspects of Electroanalysis 11.4 (1999), pp. 254–259.

[53] B. R. Shaw and K. E. Creasy. "Polishable modified electrodes made from cross-linked electroactive composites containing particulate carbon". In: *Analytical Chemistry* 60.11 (1988), pp. 1241–1244.

[54] A. Walcarius, S. Rozanska, J. Bessière, and J. Wang. "Screen-printed zeolite-modified carbon electrodes". In: *Analyst* 124.8 (1999), pp. 1185–1190.

[55] Z. Li, C. M. Wang, L. Persaud, and T. E. Mallouk. "Electrochemistry of metalloporphyrins and viologens at zeolite Y-modified electrodes: evidence for electron trapping by monomolecular porphyrin layers". In: *The Journal of Physical Chemistry* 92.9 (1988), pp. 2592–2597.

[56] Z. Li and T. E. Mallouk. "Vectorial electron transport at ion-exchanged zeolite-Y-modified electrodes". In: *Journal of Physical Chemistry* 91.3 (1987), pp. 643–648.

[57] M. M. Ardakani, Z Akrami, H Kazemian, and H. Zare. "Electrocatalytic characteristics of uric acid oxidation at graphite–zeolite-modified electrode doped with iron (III)". In: *Journal of Electroanalytical Chemistry* 586.1 (2006), pp. 31–38.

[58] K. E. Creasy and B. R. Shaw. "Electrochemistry of Oxygen, Isopropanol Vapor, and Uranyl, Cobalt (II), Nickel (II), and Copper (II) Ions in Dry Zeolites at Elevated Temperatures". In: *Journal of The Electrochemical Society* 137.7 (1990), p. 2353.

[59] N. Evmiridis, M. Demertzis, and A. Vlessidis. "Effect of treatment of synthetic zeolite-polymer membranes on their electrochemical-potential response characteristics". In: *Fresenius' journal of analytical chemistry* 340.3 (1991), pp. 145–152.

[60] J. Wang and A. Walcarius. "Zeolite containing oxidase-based carbon paste biosensors". In: *Journal of Electroanalytical Chemistry* 404.2 (1996), pp. 237–242.

[61] G. Marko-Varga, E. Burestedt, C. J. Svensson, J. Emnéus, L. Gorton, T. Ruzgas, M. Lutz, and K. K. Unger. "Effect of HY-zeolites on the performance of tyrosinase-modified carbon paste electrodes". In: *Electroanalysis* 8.12 (1996), pp. 1121–1126.

[62] J. Wang and A. Walcarius. "Zeolite-modified carbon paste electrode for selective monitoring of dopamine". In: *Journal of Electroanalytical Chemistry* 407.1-2 (1996), pp. 183–187.

[63] B. Li, H.-M. Wen, Y. Cui, W. Zhou, G. Qian, and B. Chen. "Emerging multifunctional metal–organic framework materials". In: *Advanced Materials* 28.40 (2016), pp. 8819–8860.

[64] S. M. Moosavi, A. Nandy, K. M. Jablonka, D. Ongari, J. P. Janet, P. G. Boyd, Y. Lee, B. Smit, and H. J. Kulik. "Understanding the diversity of the metal-organic framework ecosystem". In: *Nature communications* 11.1 (2020), pp. 1–10.

[65] T. F. Willems, C. H. Rycroft, M. Kazi, J. C. Meza, and M. Haranczyk. "Algorithms and tools for high-throughput geometry-based analysis of crystalline porous materials". In: *Microporous and Mesoporous Materials* 149.1 (2012), pp. 134–141.

[66] Y. G. Chung, J. Camp, M. Haranczyk, B. J. Sikora, W. Bury, V. Krungleviciute, T. Yildirim, O. K. Farha, D. S. Sholl, and R. Q. Snurr. "Computation-ready, experimental metal–organic frameworks: A tool to enable high-throughput screening of nanoporous crystals". In: *Chemistry of Materials* 26.21 (2014), pp. 6185–6192.

[67] O. K. Farha, A. Ö. Yazaydın, I. Eryazici, C. D. Malliakas, B. G. Hauser, M. G. Kanatzidis, S. T. Nguyen, R. Q. Snurr, and J. T. Hupp. "De novo synthesis of a metal–organic framework material featuring ultrahigh surface area and gas storage capacities". In: *Nature chemistry* 2.11 (2010), pp. 944–948.

[68] L. J. Murray, M. Dincă, and J. R. Long. "Hydrogen storage in metal–organic frameworks". In: *Chemical Society Reviews* 38.5 (2009), pp. 1294–1314.

[69] A Corma, H. García, and F. Llabrés i Xamena. "Engineering metal organic frameworks for heterogeneous catalysis". In: *Chemical reviews* 110.8 (2010), pp. 4606–4655.

[70] L. Ma, J. M. Falkowski, C. Abney, and W. Lin. "A series of isoreticular chiral metal–organic frameworks as a tunable platform for asymmetric catalysis". In: *Nature chemistry* 2.10 (2010), pp. 838–846.

[71] J.-R. Li, R. J. Kuppler, and H.-C. Zhou. "Selective gas adsorption and separation in metal–organic frameworks". In: *Chemical Society Reviews* 38.5 (2009), pp. 1477–1504.

[72] S. Shimomura, M. Higuchi, R. Matsuda, K. Yoneda, Y. Hijikata, Y. Kubota, Y. Mita, J. Kim, M. Takata, and S. Kitagawa. "Selective sorption of oxygen and nitric oxide by an electron-donating flexible porous coordination polymer". In: *Nature Chemistry* 2.8 (2010), pp. 633–637.

[73] J. Gascon and F. Kapteijn. "Metal-Organic Framework Membranes— High Potential, Bright Future?" In: *Angewandte Chemie International Edition* 49.9 (2010), pp. 1530–1532.

[74] H. M. Lin, C. X. Qing, Q. Miao, and X. H. Ping. "Hydrothermal Synthesis and Crystal Structure of a Europium (III) Coordination Polymer with 5-Sulfoisophthalate Trivalent Anions and Free 4, 4'-Bipyridine Molecules". In: *Russian Journal of Coordination Chemistry* 31.5 (2005), pp. 368–374.

[75] A. J. Blake, N. R. Champness, M. Crew, and S. Parsons. "Sawhorse connections in a Ag (I)-nitrite coordination network:{[Ag (pyrazine)] NO 2}". In: *New Journal of Chemistry* 23.1 (1999), pp. 13–15.

[76] N. Masciocchi, F. Castelli, P. M. Forster, M. M. Tafoya, and A. K. Cheetham. "Synthesis and characterization of two polymorphic crystalline phases and an amorphous powder of nickel (II) bisimidazolate". In: *Inorganic chemistry* 42.19 (2003), pp. 6147–6152.

[77] A. de Bettencourt-Dias. "Isophthalato-based 2D coordination polymers of Eu (III), Gd (III), and Tb (III): Enhancement of the terbium-centered luminescence through thiophene derivatization". In: *Inorganic chemistry* 44.8 (2005), pp. 2734–2741.

[78] L. Carlucci, G. Ciani, D. M. Proserpio, and A. Sironi. "Novel Networks of Unusually Coordinated Silver (i) Cations: The Wafer-Like Structure of [Ag (pyz) 2][Ag2 (pyz) 5](PF6) 3· 2G and the Simple Cubic Frame of [Ag (pyz) 3](SbF6)". In: *Angewandte Chemie International Edition in English* 34.17 (1995), pp. 1895–1898.

[79] H. Li, M. Eddaoudi, M. O'Keeffe, and O. M. Yaghi. "Design and synthesis of an exceptionally stable and highly porous metal-organic framework". In: *nature* 402.6759 (1999), pp. 276–279.

[80] Z. Dou, J. Yu, H. Xu, Y. Cui, Y. Yang, and G. Qian. "Preparation and thiols sensing of luminescent metal–organic framework films functionalized with lanthanide ions". In: *Microporous and mesoporous materials* 179 (2013), pp. 198–204.

[81] J. Zhuang, J. Friedel, and A. Terfort. "The oriented and patterned growth of fluorescent metal–organic frameworks onto functionalized surfaces". In: *Beilstein Journal of Nanotechnology* 3.1 (2012), pp. 570–578.

[82] Y.-M. Zhu, C.-H. Zeng, T.-S. Chu, H.-M. Wang, Y.-Y. Yang, Y.-X. Tong, C.-Y. Su, and W.-T. Wong. "A novel highly luminescent LnMOF film: a convenient sensor for Hg 2+ detecting". In: *Journal of Materials Chemistry A* 1.37 (2013), pp. 11312–11319.

[83] H. Furukawa, N. Ko, Y. B. Go, N. Aratani, S. B. Choi, E. Choi, A. Ö. Yazaydin, R. Q. Snurr, M. O'Keeffe, J. Kim, et al. "Ultrahigh porosity in metal-organic frameworks". In: *Science* 329.5990 (2010), pp. 424–428.

[84] O. K. Farha, I. Eryazici, N. C. Jeong, B. G. Hauser, C. E. Wilmer, A. A. Sarjeant, R. Q. Snurr, S. T. Nguyen, A. O. Yazaydın, and J. T. Hupp. "Metal–organic framework materials with ultrahigh surface areas: is the sky the limit?" In: *Journal of the American Chemical Society* 134.36 (2012), pp. 15016–15021.

[85] J. A. Hurd, R. Vaidhyanathan, V. Thangadurai, C. I. Ratcliffe, I. L. Moudrakovski, and G. K. Shimizu. "Anhydrous proton conduction at 150 C in a crystalline metal–organic framework". In: *Nature chemistry* 1.9 (2009), pp. 705–710.

[86] G. Férey, F. Millange, M. Morcrette, C. Serre, M.-L. Doublet, J.-M. Grenèche, and J.-M. Tarascon. "Mixed-valence Li/Fe-based metal–organic frameworks with both reversible redox and sorption properties". In: *Angewandte Chemie International Edition* 46.18 (2007), pp. 3259–3263.

[87] Z. Zhang, H. Yoshikawa, and K. Awaga. "Monitoring the solid-state electrochemistry of Cu (2, 7-AQDC)(AQDC= anthraquinone dicarboxylate) in a lithium battery: Coexistence of metal and ligand redox activities in a metal–organic framework". In: *Journal of the American Chemical Society* 136.46 (2014), pp. 16112–16115.

[88] H. B. Wu and X. W. D. Lou. "Metal-organic frameworks and their derived materials for electrochemical energy storage and conversion: Promises and challenges". In: *Science Advances* 3.12 (2017), eaap9252.

[89] A. P. Cote, A. I. Benin, N. W. Ockwig, M. O'Keeffe, A. J. Matzger, and O. M. Yaghi. "Porous, crystalline, covalent organic frameworks". In: *science* 310.5751 (2005), pp. 1166–1170.

[90] H. M. El-Kaderi, J. R. Hunt, J. L. Mendoza-Cortés, A. P. Côté, R. E. Taylor, M. O'Keeffe, and O. M. Yaghi. "Designed synthesis of 3D covalent organic frameworks". In: *Science* 316.5822 (2007), pp. 268–272.

[91] C. S. Diercks and O. M. Yaghi. "The atom, the molecule, and the covalent organic framework". In: *Science* 355.6328 (2017).

[92] Y. Jin, Y. Hu, and W. Zhang. "Tessellated multiporous two-dimensional covalent organic frameworks". In: *Nature Reviews Chemistry* 1.7 (2017), pp. 1–11.

[93] S.-Y. Ding, J. Gao, Q. Wang, Y. Zhang, W.-G. Song, C.-Y. Su, and W. Wang. "Construction of covalent organic framework for catalysis: Pd/COF-LZU1 in Suzuki–Miyaura coupling reaction". In: *Journal of the American Chemical Society* 133.49 (2011), pp. 19816–19822.

[94] E. L. Spitler and W. R. Dichtel. "Lewis acid-catalysed formation of two-dimensional phthalocyanine covalent organic frameworks". In: *Nature chemistry* 2.8 (2010), p. 672.

[95] J. W. Colson, A. R. Woll, A. Mukherjee, M. P. Levendorf, E. L. Spitler, V. B. Shields, M. G. Spencer, J. Park, and W. R. Dichtel. "Oriented 2D covalent organic framework thin films on single-layer graphene". In: *Science* 332.6026 (2011), pp. 228–231.

[96] P. Kuhn, M. Antonietti, and A. Thomas. "Porous, covalent triazine-based frameworks prepared by ionothermal synthesis". In: *Angewandte Chemie International Edition* 47.18 (2008), pp. 3450–3453.

[97] H. Ren, T. Ben, E. Wang, X. Jing, M. Xue, B. Liu, Y. Cui, S. Qiu, and G. Zhu. "Targeted synthesis of a 3D porous aromatic framework for selective sorption of benzene". In: *Chemical communications* 46.2 (2010), pp. 291–293.

[98] N. L. Campbell, R. Clowes, L. K. Ritchie, and A. I. Cooper. "Rapid microwave synthesis and purification of porous covalent organic frameworks". In: *Chemistry of Materials* 21.2 (2009), pp. 204–206.

[99] L. K. Ritchie, A. Trewin, A. Reguera-Galan, T. Hasell, and A. I. Cooper. "Synthesis of COF-5 using microwave irradiation and conventional solvothermal routes". In: *Microporous and mesoporous materials* 132.1-2 (2010), pp. 132–136.

[100] S.-Y. Ding and W. Wang. "Covalent organic frameworks (COFs): from design to applications". In: *Chemical Society Reviews* 42.2 (2013), pp. 548–568.

[101] R. K. Sharma, P. Yadav, M. Yadav, R. Gupta, P. Rana, A. Srivastava, R. Zbořil, R. S. Varma, M. Antonietti, and M. B. Gawande. "Recent development of covalent organic frameworks (COFs): synthesis and catalytic (organic-electro-photo) applications". In: *Materials Horizons* 7.2 (2020), pp. 411–454.

[102] V. Nguyen and M. Gru´nwald. "Microscopic origins of poor crystallinity in the synthesis of covalent organic framework COF-5". In: *Journal of the American Chemical Society* 140.9 (2018), pp. 3306–3311.

[103] S.-T. Yang, J. Kim, H.-Y. Cho, S. Kim, and W.-S. Ahn. "Facile synthesis of covalent organic frameworks COF-1 and COF-5 by sonochemical method". In: *RSC advances* 2.27 (2012), pp. 10179–10181.

[104] B. P. Biswal, S. Chandra, S. Kandambeth, B. Lukose, T. Heine, and R. Banerjee. "Mechanochemical synthesis of chemically stable isoreticular covalent organic frameworks". In: *Journal of the American Chemical Society* 135.14 (2013), pp. 5328–5331.

[105] S. Kim and H. C. Choi. "Light-promoted synthesis of highly-conjugated crystalline covalent organic framework". In: *Communications Chemistry* 2.1 (2019), pp. 1–8.

[106] B. M. Rambo and J. J. Lavigne. "Defining self-assembling linear oligo (dioxaborole) s". In: *Chemistry of materials* 19.15 (2007), pp. 3732–3739.

[107] F. J. Uribe-Romo, J. R. Hunt, H. Furukawa, C. Klock, M. O'Keeffe, and O. M. Yaghi. "A crystalline imine-linked 3-D porous covalent organic framework". In: *Journal of the American Chemical Society* 131.13 (2009), pp. 4570–4571.

[108] X. Feng, X. Ding, and D. Jiang. "Covalent organic frameworks". In: *Chemical Society Reviews* 41.18 (2012), pp. 6010–6022.

[109] A. P. Cote, H. M. El-Kaderi, H. Furukawa, J. R. Hunt, and O. M. Yaghi. "Reticular synthesis of microporous and mesoporous 2D covalent organic frameworks". In: *Journal of the American Chemical Society* 129.43 (2007), pp. 12914–12915.

[110] N. A. Zwaneveld, R. Pawlak, M. Abel, D. Catalin, D. Gigmes, D. Bertin, and L. Porte. "Organized formation of 2D extended covalent organic frameworks at surfaces". In: *Journal of the American Chemical Society* 130.21 (2008), pp. 6678–6679.

[111] P. Pachfule, A. Acharjya, J. Roeser, T. Langenhahn, M. Schwarze, R. Schoma´cker, A. Thomas, and J. Schmidt. "Diacetylene functionalized covalent organic framework (COF) for photocatalytic hydrogen generation". In: *Journal of the American Chemical Society* 140.4 (2018), pp. 1423–1427.

[112] X. Li, C. Zhang, S. Cai, X. Lei, V. Altoe, F. Hong, J. J. Urban, J. Ciston, E. M. Chan, and Y. Liu. "Facile transformation of imine covalent organic frameworks into ultrastable crystalline porous aromatic frameworks". In: *Nature communications* 9.1 (2018), pp. 1–8.

[113] H. Furukawa and O. M. Yaghi. "Storage of hydrogen, methane, and carbon dioxide in highly porous covalent organic frameworks for clean energy applications". In: *Journal of the American Chemical Society* 131.25 (2009), pp. 8875–8883.

[114] N. Huang, X. Chen, R. Krishna, and D. Jiang. "Two-dimensional covalent organic frameworks for carbon dioxide capture through channel-wall functionalization". In: *Angewandte Chemie* 127.10 (2015), pp. 3029–3033.

[115] M. G. Rabbani, A. K. Sekizkardes, Z. Kahveci, T. E. Reich, R. Ding, and H. M. El-Kaderi. "A 2D mesoporous imine-linked covalent organic framework for high pressure gas storage applications". In: *Chem. Eur. J* 19.10 (2013), pp. 3324–3328.

[116] H. Oh, S. B. Kalidindi, Y. Um, S. Bureekaew, R. Schmid, R. A. Fischer, and M. Hirscher. "A cryogenically flexible covalent organic framework for efficient hydrogen isotope separation by quantum sieving". In: *Angewandte Chemie International Edition* 52.50 (2013), pp. 13219–13222.

[117] Z. Li, Y. Zhang, H. Xia, Y. Mu, and X. Liu. "A robust and luminescent covalent organic framework as a highly sensitive and selective sensor for

the detection of Cu 2+ ions". In: *Chemical Communications* 52.39 (2016), pp. 6613–6616.

[118] G. Das, B. P. Biswal, S. Kandambeth, V Venkatesh, G. Kaur, M. Addicoat, T. Heine, S. Verma, and R. Banerjee. "Chemical sensing in two dimensional porous covalent organic nanosheets". In: *Chemical science* 6.7 (2015), pp. 3931–3939.

[119] S.-Y. Ding, M. Dong, Y.-W. Wang, Y.-T. Chen, H.-Z. Wang, C.-Y. Su, and W. Wang. "Thioether-based fluorescent covalent organic framework for selective detection and facile removal of mercury (II)". In: *Journal of the American Chemical Society* 138.9 (2016), pp. 3031–3037.

[120] S. Lu, Y. Hu, S. Wan, R. McCaffrey, Y. Jin, H. Gu, and W. Zhang. "Synthesis of ultrafine and highly dispersed metal nanoparticles confined in a thioether-containing covalent organic framework and their catalytic applications". In: *Journal of the American Chemical Society* 139.47 (2017), pp. 17082–17088.

[121] D. Ma, Y. Wang, A. Liu, S. Li, C. Lu, and C. Chen. "Covalent organic frameworks: Promising materials as heterogeneous catalysts for CC bond formations". In: *Catalysts* 8.9 (2018), p. 404.

[122] S. Wan, J. Guo, J. Kim, H. Ihee, and D. Jiang. "A belt-shaped, blue luminescent, and semiconducting covalent organic framework". In: *Angewandte Chemie International Edition* 47.46 (2008), pp. 8826–8830.

[123] X. Ding, J. Guo, X. Feng, Y. Honsho, J. Guo, S. Seki, P. Maitarad, A. Saeki, S. Nagase, and D. Jiang. "Synthesis of metallophthalocyanine covalent organic frameworks that exhibit high carrier mobility and photoconductivity". In: *Angewandte Chemie International Edition* 50.6 (2011), pp. 1289–1293.

[124] M. Dogru, M. Handloser, F. Auras, T. Kunz, D. Medina, A. Hartschuh, P. Knochel, and T. Bein. "A photoconductive thienothiophene-based covalent organic framework showing charge transfer towards included fullerene". In: *Angewandte Chemie* 125.10 (2013), pp. 2992–2996.

[125] C. R. DeBlase, K. E. Silberstein, T.-T. Truong, H. D. Abrunã, and W. R. Dichtel. "β-Ketoenamine-linked covalent organic frameworks capable of pseudocapacitive energy storage". In: *Journal of the American Chemical Society* 135.45 (2013), pp. 16821–16824.

[126] U. Díaz and A. Corma. "Ordered covalent organic frameworks, COFs and PAFs. From preparation to application". In: *Coordination Chemistry Reviews* 311 (2016), pp. 85–124.

[127] J. Wang and S. Zhuang. "Covalent organic frameworks (COFs) for environmental applications". In: *Coordination Chemistry Reviews* 400 (2019), p. 213046.

[128] N. Huang, P. Wang, and D. Jiang. "Covalent organic frameworks: a materials platform for structural and functional designs". In: *Nature Reviews Materials* 1.10 (2016), pp. 1–19.

[129] H.-L. Qian, C.-X. Yang, W.-L. Wang, C. Yang, and X.-P. Yan. "Advances in covalent organic frameworks in separation science". In: *Journal of Chromatography A* 1542 (2018), pp. 1–18.

[130] S. S. Han, J. L. Mendoza-Cortés, and W. A. Goddard Iii. "Recent advances on simulation and theory of hydrogen storage in metal–organic frameworks and covalent organic frameworks". In: *Chemical Society Reviews* 38.5 (2009), pp. 1460–1476.

[131] C. Kresge, M. Leonowicz, W. J. Roth, J. Vartuli, and J. Beck. "Ordered mesoporous molecular sieves synthesized by a liquid-crystal template mechanism". In: *nature* 359.6397 (1992), pp. 710–712.

[132] J. S. Beck, J. Vartuli, W. J. Roth, M. Leonowicz, C. Kresge, K. Schmitt, C. Chu, D. H. Olson, E. Sheppard, S. McCullen, et al. "A new family of mesoporous molecular sieves prepared with liquid crystal templates". In: *Journal of the American Chemical Society* 114.27 (1992), pp. 10834–10843.

[133] C. T. Kresge and W. J. Roth. "The discovery of mesoporous molecular sieves from the twenty year perspective". In: *Chemical Society Reviews* 42.9 (2013), pp. 3663–3670.

[134] A. Walcarius, M. Etienne, S. Sayen, and B. Lebeau. "Grafted silicas in electroanalysis: amorphous versus ordered mesoporous materials". In: *Electroanalysis: An International Journal Devoted to Fundamental and Practical Aspects of Electroanalysis* 15.5-6 (2003), pp. 414–421.

[135] T. Yanagisawa, T. Shimizu, K. Kuroda, and C. Kato. "The preparation of alkyltriinethylaininonium–kaneinite complexes and their conversion to microporous materials". In: *Bulletin of the Chemical Society of Japan* 63.4 (1990), pp. 988–992.

[136] V. Meynen, P. Cool, and E. Vansant. "Verified syntheses of mesoporous materials". In: *Microporous and mesoporous materials* 125.3 (2009), pp. 170–223.

[137] D. Zhao, J. Feng, Q. Huo, N. Melosh, G. H. Fredrickson, B. F. Chmelka, and G. D. Stucky. "Triblock copolymer syntheses of mesoporous silica with periodic 50 to 300 angstrom pores". In: *science* 279.5350 (1998), pp. 548–552.

[138] P. T. Tanev and T. J. Pinnavaia. "A neutral templating route to mesoporous molecular sieves". In: *science* 267.5199 (1995), pp. 865–867.

[139] S. A. Bagshaw, E. Prouzet, and T. J. Pinnavaia. "Templating of mesoporous molecular sieves by nonionic polyethylene oxide surfactants". In: *Science* 269.5228 (1995), pp. 1242–1244.

[140] C. J. Brinker and G. W. Scherer. "Hydrolysis and condensation of silicates: effects on structure". In: *Sol-gel science: the physics and chemistry of sol-gel processing*. Vol. 100. Academic Press, 1990. ISBN: 978-0-08-057103-4.

[141] A. Buckley and M. Greenblatt. "The sol-gel preparation of silica gels". In: *Journal of chemical education* 71.7 (1994), p. 599.

[142] T. Montheil, C. Echalier, J. Martinez, G. Subra, and A. Mehdi. "Inorganic polymerization: an attractive route to biocompatible hybrid hydrogels". In: *Journal of Materials Chemistry B* 6.21 (2018), pp. 3434–3448.

[143] L. Nam, C. Coll, L. Erthal, C. De la Torre, D. Serrano, R. Martínez-Máñez, M. Santos-Martínez, and E. Ruiz-Hernández. "Drug delivery nanosystems for the localized treatment of glioblastoma multiforme". In: *Materials* 11.5 (2018), p. 779.

[144] Z. Teng, G. Zheng, Y. Dou, W. Li, C.-Y. Mou, X. Zhang, A. M. Asiri, and D. Zhao. "Highly ordered mesoporous silica films with perpendicular mesochannels by a simple stöber-solution growth approach". In: *Angewandte Chemie International Edition* 51.9 (2012), pp. 2173–2177.

[145] P Chatterjee, S Hazra, and H Amenitsch. "Substrate and drying effect in shape and ordering of micelles inside CTAB–silica mesostructured films". In: *Soft Matter* 8.10 (2012), pp. 2956–2964.

[146] M. Etienne, A. Quach, D. Grosso, L. Nicole, C. Sanchez, and A. Walcarius. "Molecular transport into mesostructured silica thin films: Electrochemical monitoring and comparison between p6m, P63//WWIC, and Pm3n structures". In: *Chemistry of Materials* 19.4 (2007), pp. 844–856. ISSN: 08974756.

[147] A. J. Bard and L. R. Faulkner. "Fundamentals and applications". In: *Electrochemical Methods* 2.482 (2001), pp. 580–632.

[148] R. G. Compton and C. E. Banks. *Understanding Voltammetry*. 3rd Editio. WORLD SCIENTIFIC (EUROPE), 2018. ISBN: 978-1-78634-526-4.

[149] E. Gergely-Fülöp, N. Nagy, and A. Deák. "Langmuir-Blodgett films of gold nanorods with different silica shell thicknesses". In: *Periodica Polytechnica-chemical Engineering* (2014), in–press.

[150] Y. Z. Falk, J. Schmitt, and V. Alfredsson. "Langmuir–Blodgett monolayers of SBA-15 particles with different morphologies". In: *Microporous and Mesoporous Materials* 256 (2018), pp. 32–38.

[151] C. A. Koval and F. C. Anson. "Electrochemistry of the ruthenium (3+, 2+) couple attached to graphite electrodes". In: *Analytical Chemistry* 50.2 (1978), pp. 223–229.

[152] C. Daniel, T. Kuwana, and G. P. Royer. "Stable attachment of redox groups for modified electrodes via cyanuric chloride". In: *Journal of Electroanalytical Chemistry and Interfacial Electrochemistry* 98.2 (1979), pp. 345–353.

[153] J. R. Lenhard and R. W. Murray. "Chemically modified electrodes. 13. Monolayer/multilayer coverage, decay kinetics, and solvent and interaction effects for ferrocenes covalently linked to platinum electrodes". In: *Journal of the American Chemical Society* 100.25 (1978), pp. 7870–7875.

[154] T. Nasir, L. Zhang, N. Vilà, G. Herzog, and A. Walcarius. "Electrografting of 3-aminopropyltriethoxysilane on a glassy carbon electrode for the improved adhesion of vertically oriented mesoporous silica thin films". In: *Langmuir* 32.17 (2016), pp. 4323–4332.

[155] I. Svancara, K. Kalcher, A. Walcarius, and K. Vytras. *Electroanalysis with carbon paste electrodes*. Crc Press, 2012.

[156] S. Wu, H. Ju, and Y. Liu. "Conductive mesocellular silica–carbon nanocomposite foams for immobilization, direct electrochemistry, and biosensing of proteins". In: *Advanced Functional Materials* 17.4 (2007), pp. 585–592.

[157] M. Zhou, L.-p. Guo, F.-y. Lin, and H.-x. Liu. "Electrochemistry and electrocatalysis of polyoxometalate-ordered mesoporous carbon modified electrode". In: *Analytica chimica acta* 587.1 (2007), pp. 124–131.

[158] A.-H. Lu and F. Schüth. "Nanocasting: a versatile strategy for creating nanostructured porous materials". In: *Advanced Materials* 18.14 (2006), pp. 1793–1805.

[159] E. K. Richman, T. Brezesinski, and S. H. Tolbert. "Vertically oriented hexagonal mesoporous films formed through nanometre-scale epitaxy". In: *Nature materials* 7.9 (2008), pp. 712–717.

[160] A. Walcarius, E. Sibottier, M. Etienne, and J. Ghanbaja. "Electrochemically assisted self-assembly of mesoporous silica thin films". In: *Nature Materials* 6.8 (2007), pp. 602–608. ISSN: 1476-1122.

[161] A. Goux, M. Etienne, E. Aubert, C. Lecomte, J. Ghanbaja, and A. Walcarius. "Oriented mesoporous silica films obtained by electro-assisted self-assembly (EASA)". In: *Chemistry of Materials* 21.4 (2009), pp. 731–741.

[162] C. Ma, L. Han, Z. Jiang, Z. Huang, J. Feng, Y. Yao, and S. Che. "Growth of mesoporous silica film with vertical channels on substrate using gemini surfactants". In: *Chemistry of Materials* 23.16 (2011), pp. 3583–3586.

[163] C. Robertson, R. Beanland, S. A. Boden, A. L. Hector, R. J. Kashtiban, J. Sloan, D. C. Smith, and A. Walcarius. "Ordered mesoporous silica films

with pores oriented perpendicular to a titanium nitride substrate". In: *Physical Chemistry Chemical Physics* 17.6 (2015), pp. 4763–4770.

[164] K.-C. C. Kao, C.-H. H. Lin, T.-y. Y. Chen, Y.-h. H. Liu, and C.-y. Y. Mou. "A General Method for Growing Large Area Mesoporous Silica Thin Films on Flat Substrates with Perpendicular Nanochannels". In: *Journal of the American Chemical Society* 137.11 (2015), pp. 3779–3782. ISSN: 15205126.

[165] N. Vilà, J. Ghanbaja, E. Aubert, and A. Walcarius. "Electrochemically Assisted Generation of Highly Ordered Azide-Functionalized Mesoporous Silica for Oriented Hybrid Films". In: *Angewandte Chemie* 126.11 (2014), pp. 2989–2994.

[166] G. Herzog, E. Sibottier, M. Etienne, and A. Walcarius. "Electrochemically assisted self-assembly of ordered and functionalized mesoporous silica films: impact of the electrode geometry and size on film formation and properties". In: *Faraday Discussions* 164 (2013), p. 259. ISSN: 1359-6640.

[167] D. Basnig, N. Vilá, G. Herzog, and A. Walcarius. "Voltammetric behaviour of cationic redox probes at mesoporous silica film electrodes". In: *Journal of Electroanalytical Chemistry* (2020), p. 113993.

[168] G. Giordano, N. Vilà, E. Aubert, J. Ghanbaja, and A. Walcarius. "Multilayered, vertically-aligned and functionalized mesoporous silica films generated by sequential electrochemically assisted self-assembly". In: *Electrochimica Acta* 237 (2017), pp. 227–236.

[169] N. Vila`, E. Andre´, R. Ciganda, J. Ruiz, D. Astruc, and A. Walcarius. "Molecular sieving with vertically aligned mesoporous silica films and electronic wiring through isolating nanochannels". In: *Chemistry of Materials* 28.8 (2016), pp. 2511–2514. ISSN: 0897-4756.

[170] T. Nasir, G. Herzog, M. Hébrant, C. Despas, L. Liu, and A. Walcarius. "Mesoporous silica thin films for improved electrochemical detection of paraquat". In: *ACS sensors* 3.2 (2018), pp. 484–493.

[171] C. Karman, N. Vilà, and A. Walcarius. "Amplified charge transfer for anionic redox probes through oriented mesoporous silica thin films". In: *ChemElectroChem* 3.12 (2016), pp. 2130–2137. ISSN: 21960216.

[172] Z. Zhou, W. Guo, L. Xu, Q. Yang, and B. Su. "Two orders-of-magnitude enhancement in the electrochemiluminescence of Ru (bpy) 32+ by vertically ordered silica mesochannels". In: *Analytica chimica acta* 886 (2015), pp. 48–55.

[173] Q. Sun, F. Yan, L. Yao, and B. Su. "Anti-biofouling isoporous silica-micelle membrane enabling drug detection in human whole blood". In: *Analytical Chemistry* 88.17 (2016), pp. 8364–8368. ISSN: 15206882.

[174] C. Karman, N. Vilà, C. Despas, and A. Walcarius. "Indirect amperometric detection of non-redox ions using a ferrocene-functionalized and oriented mesoporous silica thin film electrode". In: *Electrochimica Acta* 228 (2017), pp. 659–666. ISSN: 00134686.

[175] L. Ding, W. Li, Q. Wang, Q. Sun, Y. He, and B. Su. "Vertically oriented silica mesochannels as the template for electrodeposition of polyaniline nanostructures and their electrocatalytic and electroanalytical applications". In: *Chemistry–A European Journal* 20.7 (2014), pp. 1829–1833.

[176] M. Saadaoui, I. Fernández, G. Luna, P. Díez, S. Campuzano, N. Raouafi, A. Sánchez, J. M. Pingarrón, and R. Villalonga. "Label-free electrochemical genosensor based on mesoporous silica thin film". In: *Analytical and bioanalytical chemistry* 408.26 (2016), pp. 7321–7327.

[177] X. Huang, L. Xie, X. Lin, and B. Su. "Detection of metoprolol in human biofluids and pharmaceuticals via ion-transfer voltammetry at the nanoscopic liquid/liquid interface array". In: *Analytical chemistry* 89.1 (2017), pp. 945–951.

[178] X. Yang, Z. Li, J. Zhi, J. Ma, and A. Hu. "Synthesis of ultrathin mesoporous carbon through Bergman cyclization of enediyne self-assembled monolayers in SBA-15". In: *Langmuir* 26.13 (2010), pp. 11244–11248.

[179] J. Zhi, D. Song, Z. Li, X. Lei, and A. Hu. "Palladium nanoparticles in carbon thin film-lined SBA-15 nanoreactors: Efficient heterogeneous catalysts for Suzuki–Miyaura cross coupling reaction in aqueous media". In: *Chemical Communications* 47.38 (2011), pp. 10707–10709.

[180] Ł. Laskowski, M. Laskowska, N. Vila, M. Schabikowski, and A. Walcarius. "Mesoporous silica-based materials for electronics-oriented applications". In: *Molecules* 24.13 (2019), p. 2395.

[181] M. Javed, S. M. Abbas, M. Siddiq, D. Han, and L. Niu. "Mesoporous silica wrapped with graphene oxide-conducting PANI nanowires as a novel hybrid electrode for supercapacitor". In: *Journal of Physics and Chemistry of Solids* 113 (2018), pp. 220–228.

[182] Y. Kanno, T. Suzuki, Y. Yamauchi, and K. Kuroda. "Preparation of Au nanowire films by electrodeposition using mesoporous silica films as a template: vital effect of vertically oriented mesopores on a substrate". In: *The Journal of Physical Chemistry C* 116.46 (2012), pp. 24672–24680.

[183] M. H. Huang, A. Choudrey, and P. Yang. "Ag nanowire formation within mesoporous silica". In: *Chemical Communications* 12 (2000), pp. 1063–1064.

[184] Y. Ai, H. Smida, J. Ghilane, N. Vilà, J. Ghanbaja, A. Walcarius, and J. C. Lacroix. "Copper Nanowires through Oriented Mesoporous Silica: A Step

towards Protected and Parallel Atomic Switches". In: *Scientific reports* 7.1 (2017), pp. 1–9.

[185] A. Keilbach, J. Moses, R. Köhn, M. Döblinger, and T. Bein. "Electrodeposition of copper and silver nanowires in hierarchical mesoporous silica/anodic alumina nanostructures". In: *Chemistry of materials* 22.19 (2010), pp. 5430–5436.

[186] A. Gamero-Quijano, C. Karman, N. Vilà, G. Herzog, and A. Walcarius. "Vertically aligned and ordered one-dimensional mesoscale polyaniline". In: *Langmuir* 33.17 (2017), pp. 4224–4234.

[187] Z. Hu, L. Zu, Y. Jiang, H. Lian, Y. Liu, X. Wang, and X. Cui. "High performance nanocomposite electrodes of mesoporous silica platelet-polyaniline synthesized via impregnation polymerization". In: *Polymer Composites* 38.8 (2017), pp. 1616–1623.

[188] M Sasidharan, N. Mal, and A Bhaumik. "In-situ polymerization of grafted aniline in the channels of mesoporous silica SBA-15". In: *Journal of Materials Chemistry* 17.3 (2007), pp. 278–283.

[189] N. Li, X. Li, W. Geng, T. Zhang, Y. Zuo, and S. Qiu. "Synthesis and humidity sensitivity of conducting polyaniline in SBA-15". In: *Journal of applied polymer science* 93.4 (2004), pp. 1597–1601.

[190] M. A. del Valle, M. Gacitúa, F. R. Díaz, F. Armijo, and R. del Río. "Electrosynthesis of polythiophene nanowires via mesoporous silica thin film templates". In: *Electrochemistry communications* 11.11 (2009), pp. 2117–2120.

[191] S. M. Fonseca, T. Moreira, A. J. Parola, C. Pinheiro, and C. A. Laia. "PEDOT electrodeposition on oriented mesoporous silica templates for electrochromic devices". In: *Solar Energy Materials and Solar Cells* 159 (2017), pp. 94–101.

[192] Q. Cheng, V. Pavlinek, A. Lengalova, C. Li, Y. He, and P. Saha. "Conducting polypyrrole confined in ordered mesoporous silica SBA-15 channels: preparation and its electrorheology". In: *Microporous and mesoporous materials* 93.1-3 (2006), pp. 263–269.

[193] Q. Cheng, V. Pavlinek, C. Li, A. Lengalova, Y. He, and P. Saha. "Synthesis and characterization of new mesoporous material with conducting polypyrrole confined in mesoporous silica". In: *Materials Chemistry and Physics* 98.2-3 (2006), pp. 504–508.

[194] S. A. Johnson, P. J. Ollivier, and T. E. Mallouk. "Ordered mesoporous polymers of tunable pore size from colloidal silica templates". In: *Science* 283.5404 (1999), pp. 963–965.

[195] M. Kong, J. Tang, Q. Qiao, T. Wu, Y. Qi, S. Tan, X. Gao, and Z. Zhang. "Biodegradable hollow mesoporous silica nanoparticles for regulating tumor microenvironment and enhancing antitumor efficiency". In: *Theranostics* 7.13 (2017), p. 3276.

[196] Y. Guillemin, M. Etienne, E. Aubert, and A. Walcarius. "Electrogeneration of highly methylated mesoporous silica thin films with vertically-aligned mesochannels and electrochemical monitoring of mass transport issues". In: *Journal of Materials Chemistry* 20.32 (2010), pp. 6799–6807.

[197] N. Vilà, J. Ghanbaja, and A. Walcarius. "Clickable Bifunctional and Vertically Aligned Mesoporous Silica Films". In: *Advanced Materials Interfaces* 3.2 (2016), pp. 1–11. ISSN: 21967350.

[198] V. S.-Y. Lin, C.-Y. Lai, J. Huang, S.-A. Song, and S. Xu. "Molecular recognition inside of multifunctionalized mesoporous silicas: toward selective fluorescence detection of dopamine and glucosamine". In: *Journal of the American Chemical Society* 123.46 (2001), pp. 11510–11511.

[199] D. Fattakhova Rohlfing, J. Rathouskỳ, Y. Rohlfing, O. Bartels, and M. Wark. "Functionalized mesoporous silica films as a matrix for anchoring electrochemically active guests". In: *Langmuir* 21.24 (2005), pp. 11320–11329.

[200] X. Zhang, S. Duan, X. Xu, S. Xu, and C. Zhou. "Electrochemical behavior and simultaneous determination of dihydroxybenzene isomers at a functionalized SBA-15 mesoporous silica modified carbon paste electrode". In: *Electrochimica acta* 56.5 (2011), pp. 1981–1987.

[201] T. J. Smith and K. J. Stevenson. "Reference electrodes". In: (2007), pp. 73–110.

[202] D. D. Zhou. "CHAPTER 10 - Microelectrodes for in-vivo determination of pH". In: (2008). Ed. by X. Zhang, H. Ju, and J. Wang, pp. 261 –305.

[203] B. Akbari-adergani, P. Norouzi, M. R. Ganjali, and R. Dinarvand. "Ultrasensitive flow-injection electrochemical method for determination of histamine in tuna fish samples". In: *Food research international* 43.4 (2010), pp. 1116–1122.

[204] A. M. Leach, A. R. Wheeler, and R. N. Zare. "Flow injection analysis in a microfluidic format". In: *Analytical Chemistry* 75.4 (2003), pp. 967–972.

[205] D. Agustini, M. F. Bergamini, and L. H. Marcolino-Junior. "Characterization and optimization of low cost microfluidic thread based electroanalytical device for micro flow injection analysis". In: *Analytica chimica acta* 951 (2017), pp. 108–115.

[206] M. Granica, M. Fiedoruk-Pogrebniak, R. Koncki, and Ł. Tymecki. "Flow injection analysis in lab-on-paper format". In: *Sensors and Actuators B: Chemical* 257 (2018), pp. 16–22.

[207] S. Kurbanoglu, M. A. Unal, and S. A. Ozkan. "Recent developments on electrochemical flow injection in pharmaceuticals and biologically important compounds". In: *Electrochimica Acta* 287 (2018), pp. 135–148.

[208] A Di Gianfrancesco. "Technologies for chemical analyses, microstructural and inspection investigations". In: *Materials for ultra-supercritical and advanced ultra-supercritical power plants*. Elsevier, 2017, pp. 197–245.

[209] *SEM vs TEM*. Feb. 25, 2020. URL: https://www.technologynetworks.com/analysis/articles/sem-vs-tem-331262.

[210] J. R. Levine, J. Cohen, Y. Chung, and P Georgopoulos. "Grazing-incidence small-angle X-ray scattering: new tool for studying thin film growth". In: *Journal of Applied Crystallography* 22.6 (1989), pp. 528–532.

[211] D.-M. Smilgies. "Grazing-Incidence Small-Angle Scattering (GISAXS)". In: *Heimo Schnabelegger and Yashveer Sing:"The SAXS Guide, 4th Edition" (Anton Paar GmbH, 2017, ISBN 18012013) Chapter* 6 ().

[212] P. Müller-Buschbaum. "A basic introduction to grazing incidence small-angle X-ray scattering". In: *Applications of synchrotron light to scattering and diffraction in materials and life sciences*. Ed. by M. Gomez, A. Nogales, M. C. Garcia-Gutierrez, and T. Ezquerra. Springer, 2009, pp. 61–89. ISBN: 978-3-540-95968-7.

[213] W. H. Bragg and W. L. Bragg. "The reflection of X-rays by crystals". In: *Proceedings of the Royal Society of London. Series A, Containing Papers of a Mathematical and Physical Character* 88.605 (1913), pp. 428–438.

[214] B. Stuart. "Infrared spectroscopy". In: *Kirk-Othmer encyclopedia of chemical technology* (2015).

[215] W. Li, M. Zhang, J. Zhang, and Y. Han. "Self-assembly of cetyl trimethylammonium bromide in ethanol-water mixtures". In: *Frontiers of Chemistry in China* 1.4 (2006), pp. 438–442.

[216] R Huisgen. "Proceedings of the Chemical Society. October 1961". In: *Proc. Chem. Soc*. Vol. 357. 1961.

[217] N. H. Cnubben, I. M. Rietjens, H. Wortelboer, J. van Zanden, and P. J. van Bladeren. "The interplay of glutathione-related processes in antioxidant defense". In: *Environmental Toxicology and Pharmacology* 10.4 (2001), pp. 141–152. ISSN: 13826689.

[218] K. K. Dennis, Y.-M. Go, and D. P. Jones. "Redox systems biology of nutrition and oxidative stress". In: *The Journal of Nutrition* 149.4 (2019), pp. 553–565.

[219] M. H. Stipanuk, J. E. Dominy Jr, J.-I. Lee, and R. M. Coloso. "Mammalian cysteine metabolism: new insights into regulation of cysteine metabolism". In: *The Journal of nutrition* 136.6 (2006), 1652S–1659S.

[220] H. LIU, H. WANG, S. SHENVI, T. M. HAGEN, and R.-M. LIU. "Glutathione metabolism during aging and in Alzheimer disease". In: *Annals of the New York Academy of Sciences* 1019.1 (2004), pp. 346–349.

[221] S. Whillier, J. E. Raftos, and P. W. Kuchel. "Glutathione synthesis by red blood cells in type 2 diabetes mellitus". In: *Redox Report* 13.6 (2008), pp. 277–282.

[222] A. E. Lang. "The progression of Parkinson disease". In: *Neurology* 68.12 (2007), pp. 948–952. ISSN: 0028-3878.

[223] D. Long, H. Wu, A. W. Tsang, L. B. Poole, B. K. Yoza, X. Wang, V. Vacharajani, C. M. Furdui, and C. E. McCall. "The oxidative state of cysteine thiol 144 regulates the SIRT6 glucose homeostat". In: *Scientific reports* 7.1 (2017), pp. 1–8.

[224] K. Lertratanangkoon, C. J. Wu, N. Savaraj, and M. L. Thomas. "Alterations of DNA methylation by glutathione depletion". In: *Cancer letters* 120.2 (1997), pp. 149–156.

[225] L. Pendyala, S. Velagapudi, K. Toth, J. Zdanowicz, D. Glaves, H. Slocum, R. Perez, R. Huben, P. J. Creaven, and D. Raghavan. "Translational studies of glutathione in bladder cancer cell lines and human specimens." In: *Clinical cancer research* 3.5 (1997), pp. 793–798.

[226] I. Kolthoff and C. Barnum. "The Anodic Reaction and Waves of Cysteine at the Dropping Mercury Electrode and at the Platinum Micro Wire Electrode". In: *Journal of the American Chemical Society* 62.11 (1940), pp. 3061–3065.

[227] I. Kolthoff, W Stricks, and N. Tanaka. "Polarographic Reduction of Cystine and of Dithiodiglycolic Acid in the Presence of Iron". In: *Journal of the American Chemical Society* 77.20 (1955), pp. 5215–5218.

[228] N. Spătaru, B. V. Sarada, E. Popa, D. A. Tryk, and A. Fujishima. "Voltammetric determination of L-cysteine at conductive diamond electrodes". In: *Analytical Chemistry* 73.3 (2001), pp. 514–519.

[229] M. T. Stankovich and A. J. Bard. "The electrochemistry of proteins and related substances: I. Cystine and cysteine at the mercury electrode". In: *Journal of Electroanalytical Chemistry and Interfacial Electrochemistry* 75.2 (1977), pp. 487–505.

[230] F. G. Banica, J. C. Moreira, and A. G. Fogg. "Application of catalytic stripping voltammetry for the determination of organic sulfur compounds at a hanging mercury drop electrode: behaviour of cysteine, cystine and N-acetylcysteine in the presence of nickel ion". In: *Analyst* 119.2 (1994), pp. 309–318.

[231] D. G. Davis and E. Blanco. "An electrochemical study of the oxidation of L-cysteine". In: *Journal of Electroanalytical Chemistry (1959)* 12.3 (1966), pp. 254–260.

[232] J. Koryta and J. Pradáč. "Electrode processes of the sulfhydryl-disulfide system: III. Cysteine at platinum and gold electrodes". In: *Journal of Electroanalytical Chemistry and Interfacial Electrochemistry* 17.1-2 (1968), pp. 185–189.

[233] M. E. Johll, D. G. Williams, and D. C. Johnson. "Activated pulsed amperometric detection of cysteine at platinum electrodes in acidic media". In: *Electroanalysis* 9.18 (1997), pp. 1397–1402.

[234] J. Reynaud, B Malfoy, and P Canesson. "Electrochemical investigations of amino acids at solid electrodes: part I. Sulfur components: cystine, cysteine, methionine". In: *Journal of Electroanalytical Chemistry and Interfacial Electrochemistry* 114.2 (1980), pp. 195–211.

[235] R Eggli and R Asper. "Electrochemical flow-through detector for the determination of cystine and related compounds". In: *Analytica Chimica Acta* 101.2 (1978), pp. 253–259.

[236] R. Masella and G. Mazza. *Glutathione and sulfur amino acids in human health and disease*. John Wiley & Sons, 2009.

[237] A. Meister. "Glutathione metabolism and its selective modification." In: *Journal of biological chemistry* 263.33 (1988), pp. 17205–17208.

[238] A. Meister and M. E. Anderson. "Glutathione". In: *Annual review of biochemistry* 52.1 (1983), pp. 711–760.

[239] D. Ziegler. "Role of reversible oxidation-reduction of enzyme thiols- disulfides in metabolic regulation". In: *Annual review of biochemistry* 54.1 (1985), pp. 305–329.

[240] S. Chakravarthi, C. E. Jessop, and N. J. Bulleid. "The role of glutathione in disulphide bond formation and endoplasmic-reticulum-generated oxidative stress". In: *EMBO reports* 7.3 (2006), pp. 271–275.

[241] H. F. Gilbert. "Molecular and cellular aspects of thiol-disulfide exchange". In: *Advances in enzymology and related areas of molecular biology* 63 (1993), pp. 69–69.

[242] F. Q. Schafer and G. R. Buettner. "Redox environment of the cell as viewed through the redox state of the glutathione disulfide/glutathione couple". In: *Free radical biology and medicine* 30.11 (2001), pp. 1191–1212.

[243] G. J. Hankey and J. W. Eikelboom. "Homocysteine and vascular disease". In: *The lancet* 354.9176 (1999), pp. 407–413.

[244] M. Á. Medina, J. L. Urdiales, and M. I. Amores-Sánchez. "Roles of homocysteine in cell metabolism". In: *European journal of biochemistry* 268.14 (2001), pp. 3871–3882.

[245] M. Medina and M. Amores-Sanchez. "Homocysteine: an emergent cardiovascular risk factor?" In: *European journal of clinical investigation* 30.9 (2000), pp. 754–762.

[246] Y. Martínez, X. Li, G. Liu, P. Bin, W. Yan, D. Más, M. Valdivié, C.-A. A. Hu, W. Ren, and Y. Yin. "The role of methionine on metabolism, oxidative stress, and diseases". In: *Amino acids* 49.12 (2017), pp. 2091–2098.

[247] V. C. Diculescu and T. A. Enache. "Voltammetric and mass spectrometry investigation of methionine oxidation". In: *Journal of Electroanalytical Chemistry* 834 (2019), pp. 124–129.

[248] R. Jackson and T. Hunter. "Role of methionine in the initiation of haemoglobin synthesis". In: *Nature* 227.5259 (1970), pp. 672–676.

[249] D. A. Butterfield and D. Boyd-Kimball. "The critical role of methionine 35 in Alzheimer's amyloid β-peptide (1–42)-induced oxidative stress and neurotoxicity". In: *Biochimica et Biophysica Acta (BBA)-Proteins and Proteomics* 1703.2 (2005), pp. 149–156.

[250] W. Arber. "Host specificity of DNA produced by Escherichia coli: V. The role of methionine in the production of host specificity". In: *Journal of molecular biology* 11.2 (1965), pp. 247–256.

[251] D. J. Reed and S. Orrenius. "The role of methionine in glutathione biosynthesis by isolated hepatocytes". In: *Biochemical and biophysical research communications* 77.4 (1977), pp. 1257–1264.

[252] D. E. Wilcken, B. Wilcken, et al. "The pathogenesis of coronary artery disease. A possible role for methionine metabolism." In: *The Journal of clinical investigation* 57.4 (1976), pp. 1079–1082.

[253] "Drug Information Express, Drug R&D, Chemical Database, Patent Search". In: *Drug Future* (Copyright ©2006-2020).

[254] H. Borsook, E. L. Ellis, and H. M. Huffman. "Sulfhydryl oxidation-reduction potentials derived from thermal data". In: *Journal of Biological Chemistry* 117.1 (1937), pp. 281–308.

[255] I. Kolthoff, W. Stricks, and N. Tanaka. "The polarographic prewaves of cystine (RSSR) and dithiodiglycolic acid (TSST) and the oxidation potentials of the systems RSSR-RSH and TSST-TSH". In: *Journal of the American Chemical Society* 77.18 (1955), pp. 4739–4742.

[256] J. C. Ghosh and S. C. Ganguli. "A note on the reduction potential of cysteine-cystine mixtures". In: *Biochemical Journal* 28.2 (1934), pp. 381–383.

[257] J. S. Fruton and H. Clarke. "Chemical reactivity of cystine and its derivatives". In: *Journal of Biological Chemistry* 106.2 (1934), pp. 667–691.

[258] P. C. Jocelyn. "The Standard Redox Potential of Cysteine-Cystine from the Thiol-Disulphide Exchange Reaction with Glutathione and Lipoic Acid". In: *European Journal of Biochemistry* 2.3 (1967), pp. 327–331. ISSN: 0014-2956.

[259] M. Dixon and J. H. Quastel. "CCCXLVIII.—A new type of reduction–oxidation system. Part I. Cysteine and glutathione". In: *Journal of the Chemical Society, Transactions* 123 (1923), pp. 2943–2953.

[260] W. R. Fawcett, M. Fedurco, Z. Kováčová, and Z. Borkowska. "Oxidation of cysteine, cysteinesulfinic acid and cysteic acid on a polycrystalline gold electrode". In: *Journal of Electroanalytical Chemistry* 368.1-2 (1994), pp. 265–274. ISSN: 00220728.

[261] T. Ralph, M. Hitchman, J. Millington, and F. Walsh. "The electrochemistry of l-cystine and l-cysteine: Part 1: Thermodynamic and kinetic studies". In: *Journal of Electroanalytical Chemistry* 375.1-2 (1994), pp. 1–15.

[262] P. C. White, N. S. Lawrence, J. Davis, and R. G. Compton. "Electrochemical determination of thiols: a perspective". In: *Electroanalysis: An International Journal Devoted to Fundamental and Practical Aspects of Electroanalysis* 14.2 (2002), pp. 89–98.

[263] L. Rojas, L. Molero, R. A. Tapia, R. Del Rio, M. A. del Valle, M. Antilén, and F. Armijo. "Electrochemistry behavior of endogenous thiols on fluorine doped tin oxide electrodes". In: *Electrochimica acta* 56.24 (2011), pp. 8711–8717.

[264] P. Abiman, G. G. Wildgoose, and R. G. Compton. "Electroanalytical Exploitation of Nitroso Phenyl Modified Carbon-Thiol Interactions: Application to the Low Voltage Determination of Thiols". In: *Electroanalysis: An International Journal Devoted to Fundamental and Practical Aspects of Electroanalysis* 19.4 (2007), pp. 437–444.

[265] P. Lee, D Lowinsohn, and R. Compton. "Simultaneous detection of homocysteine and cysteine in the presence of ascorbic acid and glutathione using a nanocarbon modified electrode". In: *Electroanalysis* 26.7 (2014), pp. 1488–1496.

[266] G. Hignett, S. Threlfell, A. J. Wain, N. S. Lawrence, S. J. Wilkins, J. Davis, R. G. Compton, and M. F. Cardosi. "Electroanalytical exploitation of quinone–thiol interactions: application to the selective determination of cysteine". In: *Analyst* 126.3 (2001), pp. 353 –357.

[267] P. Song, A. C. Fisher, J. D. Wadhawan, J. J. Cooper, H. J. Ward, and N. S. Lawrence. "A mechanistic study of the EC′ mechanism–the split wave in

cyclic voltammetry and square wave voltammetry". In: *RSC advances* 6.74 (2016), pp. 70237–70242.

[268] P. T. Lee, J. E. Thomson, A. Karina, C. Salter, C. Johnston, S. G. Davies, and R. G. Compton. "Selective electrochemical determination of cysteine with a cyclotricatechylene modified carbon electrode". In: *Analyst* 140.1 (2015), pp. 236–242.

[269] F. Ricci, F. Arduini, A. Amine, D. Moscone, and G. Palleschi. "Characterisation of Prussian blue modified screen-printed electrodes for thiol detection". In: *Journal of Electroanalytical Chemistry* 563.2 (2004), pp. 229–237.

[270] W.-Y. Su and S.-H. Cheng. "Electrocatalysis and sensitive determination of cysteine at poly (3, 4-ethylenedioxythiophene)-modified screen-printed electrodes". In: *Electrochemistry Communications* 10.6 (2008), pp. 899–902.

[271] Y.-P. Hsiao, W.-Y. Su, J.-R. Cheng, and S.-H. Cheng. "Electrochemical determination of cysteine based on conducting polymers/gold nanoparticles hybrid nanocomposites". In: *Electrochimica acta* 56.20 (2011), pp. 6887–6895.

[272] L. L. Okumura, N. R. Stradiotto, N. V. Rees, and R. G. Compton. "Modifying Glassy Carbon (GC) Electrodes to Confer Selectivity for the Voltammetric Detection of l-Cysteine in the Presence of dl-Homocysteine and Glutathione". In: *Electroanalysis: An International Journal Devoted to Fundamental and Practical Aspects of Electroanalysis* 20.8 (2008), pp. 916–918.

[273] P. Lee and R. Compton. "Electrochemical detection of NADH, cysteine, or glutathione using a caffeic acid modified glassy carbon electrode". In: *Electroanalysis* 25.7 (2013), pp. 1613–1620.

[274] C. C. Corrêa, S. A. V. Jannuzzi, M. Santhiago, R. A. Timm, A. L. B. Formiga, and L. T. Kubota. "Modified electrode using multi-walled carbon nanotubes and a metallopolymer for amperometric detection of l-cysteine". In: *Electrochimica Acta* 113 (2013), pp. 332–339.

[275] S.-M. Chen, J.-Y. Chen, and R Thangamuthu. "Electrochemical preparation of brilliant-blue-modified Poly (diallyldimethylammonium Chloride) and nafion-coated glassy carbon electrodes and their electrocatalytic behavior towards oxygen and l-cysteine". In: *Electroanalysis: An International Journal Devoted to Fundamental and Practical Aspects of Electroanalysis* 20.14 (2008), pp. 1565–1573.

[276] K. A. Joshi, P. C. Pandey, W. Chen, and A. Mulchandani. "Ormosil Encapsulated Pyrroloquinoline Quinone-Modified Electrochemical Sensor for Thiols". In: *Electroanalysis: An International Journal Devoted to Fundamental and Practical Aspects of Electroanalysis* 16.23 (2004), pp. 1938–1943.

[277] A. E. Cass, G. Davis, G. D. Francis, H. A. O. Hill, W. J. Aston, I. J. Higgins, E. V. Plotkin, L. D. Scott, and A. P. Turner. "Ferrocene-mediated enzyme electrode for amperometric determination of glucose". In: *Analytical chemistry* 56.4 (1984), pp. 667–671.

[278] R. Dehdari Vais, H. Yadegari, N. Sattarahmady, and H. Heli. "An anodized nanostructure of Ni/Cu alloy synthesized in ethaline for electrocatalytic oxidation and amperometric determination of L-carnitine". In: *Journal of Electroanalytical Chemistry* 815.March (2018), pp. 134–142. ISSN: 15726657.

[279] O. Nekrassova, G. D. Allen, N. S. Lawrence, L. Jiang, T. G. J. Jones, and R. G. Compton. "The Oxidation of Cysteine by Aqueous Ferricyanide: A Kinetic Study Using Boron Doped Diamond Electrode Voltammetry". In: *Electroanalysis* 14.21 (2002), pp. 1464–1469. ISSN: 10400397.

[280] J. Savéant and K. Su. "Homogeneous redox catalysis of electrochemical reaction. Part VI: Zone diagram representation of the kinetic regimes". In: *Journal of electroanalytical chemistry and interfacial electrochemistry* 171.1-2 (1984), pp. 341–349. ISSN: 00220728.

[281] E. S. Rountree, B. D. McCarthy, T. T. Eisenhart, and J. L. Dempsey. "Evaluation of homogeneous electrocatalysts by cyclic voltammetry". In: *Inorganic Chemistry* 53.19 (2014), pp. 9983–10002. ISSN: 0020-1669.

[282] D. J. Martin, B. D. McCarthy, E. S. Rountree, and J. L. Dempsey. "Qualitative extension of the EC′ Zone Diagram to a molecular catalyst for a multi-electron, multi-substrate electrochemical reaction". In: *Dalton Transactions* 45.24 (2016), pp. 9970–9976.

[283] J. E. Taylor, J. F. Yan, and J.-l. Wang. "The Iron(III)-Catalyzed Oxidation of Cysteine by Molecular Oxygen in the Aqueous Phase. An Example of a Two-Thirds-Order Reaction". In: *Journal of the American Chemical Society* 88.8 (1966), pp. 1663–1667. ISSN: 0002-7863.

[284] N. Tanaka, I. M. Kolthoff, and W. Stricks. "Oxidation of Ferrous-Cysteinate Complex by Cystine. Oxidation Potential of the Cystine-Cysteine System". In: *Journal of the American Chemical Society* 77.7 (1955), pp. 2004–2006. ISSN: 0002-7863.

[285] S. Yin, P. Song, H. Wang, H. Ma, Z. Wang, and Y. Yu. "An investigation of homogeneous electrocatalytic mechanism between ferrocene derivatives and l-cysteine/N-Acetyl-l-cysteine". In: *Electrochimica Acta* 346 (2020), p. 136126.

[286] R. S. Nicholson and I. Shain. "Theory of stationary electrode polarography. Single scan and cyclic methods applied to reversible, irreversible, and kinetic systems." In: *Analytical chemistry* 36.4 (1964), pp. 706–723.

[287] C. J. Gagliardi, C. F. Murphy, R. A. Binstead, H. H. Thorp, and T. J. Meyer. "Concerted electron proton transfer (EPT) in the oxidation of cysteine". In: *Journal of Physical Chemistry C* 119.13 (2015), pp. 7028–7038. ISSN: 19327455.

[288] E. J. Pacsial-Ong, R. L. McCarley, W. Wang, and R. M. Strongin. "Electrochemical detection of glutathione using redox indicators". In: *Analytical chemistry* 78.21 (2006), pp. 7577–7581.

[289] B. Zappacosta, A. Mordente, S. Persichilli, A. Minucci, P. Carlino, G. E. Martorana, B. Giardina, and P. de Sole. "Is homocysteine a pro-oxidant?" In: *Free Radical Research* 35.5 (2001), pp. 499–505.

[290] J. B. Park. "Reduction of dehydroascorbic acid by homocysteine". In: *Biochimica et Biophysica Acta (BBA)-General Subjects* 1525.1-2 (2001), pp. 173–179.

[291] H. Salehzadeh, B. Mokhtari, and D. Nematollahi. "Selective electrochemical determination of homocysteine in the presence of cysteine and glutathione". In: *Electrochimica Acta* 123 (2014), pp. 353–361.

[292] J. SAVÉANT and E. VIANELLO. "RECHERCHES SUR LES COURANTS CATALYTIQUES EN POLAROGRAPHIE—OSCILLOGRAPHIQUE À BALAYAGE LINÉAIRE DE TENSION. ETUDE THÉORIQUE". In: *Advances in Polarography*. Elsevier, 1960, pp. 367–374.

[293] Ł. Laskowski, M. Laskowska, M. Dulski, M. Zubko, J. Jelonkiewicz, M. Perzanowski, N. Vila, and A. Walcarius. "Multi-step functionalization procedure for fabrication of vertically aligned mesoporous silica thin films with metal-containing molecules localized at the pores bottom". In: *Microporous and Mesoporous Materials* 274 (2019), pp. 356–362. ISSN: 13871811.

[294] N. M. Said, V. I. Ogurtsov, K. Twomey, L. C. Nagle, and G Herzog. "Chemically modified electrodes for recessed microelectrode array". In: *Procedia Chemistry* 20 (2016), pp. 12–24.

[295] H. Schnablegger and Y. Singh. "The SAXS Guide- Getting Acquainted with the Principles". In: (2013), pp. 0–126.

[296] W. Li, L. Ding, Q. Wang, and B. Su. "Differential pulse voltammetry detection of dopamine and ascorbic acid by permselective silica mesochannels vertically attached to the electrode surface". In: *Analyst* 139.16 (2014), pp. 3926–3931.

[297] M. B. Serrano, C. Despas, G. Herzog, and A. Walcarius. "Mesoporous silica thin films for molecular sieving and electrode surface protection against biofouling". In: *Electrochemistry Communications* 52 (2015), pp. 34–36.

[298] N. Vilà and A. Walcarius. "Electrochemical response of vertically-aligned, ferrocene- functionalized mesoporous silica films: effect of the supporting electrolyte". In: *Electrochimica Acta* 179 (2015), pp. 304–314.

[299] A. Lasia. "Electrochemical impedance spectroscopy and its applications". In: *Modern aspects of electrochemistry*. Springer, 2002, pp. 143–248.

[300] J. C. Harfield, C. Batchelor-McAuley, and R. G. Compton. "Electrochemical determination of glutathione: a review". In: *Analyst* 137.10 (2012), pp. 2285–2296. ISSN: 0003-2654.

[301] J. Heinze. "Ultramicroelectrodes in electrochemistry". In: *Angewandte Chemie International Edition in English* 32.9 (1993), pp. 1268–1288.

[302] D Mac Gillavry and E. Rideal. "On the theory of limiting currents. I. Polarographic limiting currents". In: *Recueil des Travaux Chimiques des Pays-Bas* 56.10 (1937), pp. 1013–1021.

[303] I. Shain and K. J. Martin. "Electrolysis with constant potential: Reversible processes at a hanging mercury drop electrode". In: *The Journal of Physical Chemistry* 65.2 (1961), pp. 254–258.

[304] I. Shain, K. J. Martin, and J. W. Ross. "Electrolysis with constant potential: Irreversible reactions at a hanging mercury drop electrode". In: *The Journal of Physical Chemistry* 65.2 (1961), pp. 259–261.

[305] R. M. Wightman. "Microvoltammetric electrodes". In: *Analytical Chemistry* 53.9 (1981), 1125A–1134A.

[306] R. Brina, S. Pons, and M. Fleischmann. "Ultramicroelectrode sensors and detectors. Considerations of the stability, sensitivity, reproducibility, and mechanism of ion transport in gas phase chromatography and in high performance liquid phase chromatography". In: (1988).

[307] A. Szabo, D. K. Cope, D. E. Tallman, P. M. Kovach, and R. M. Wightman. "Chronoamperometric current at hemicylinder and band microelectrodes: Theory and experiment". In: *Journal of electroanalytical chemistry and interfacial electrochemistry* 217.2 (1987), pp. 417–423.

[308] B. Fan, C. A. Rusinek, C. H. Thompson, M. Setien, Y. Guo, R. Rechenberg, Y. Gong, A. J. Weber, M. F. Becker, E. Purcell, et al. "Flexible, diamond-based microelectrodes fabricated using the diamond growth side for neural sensing". In: *Microsystems & nanoengineering* 6.1 (2020), pp. 1–12.

[309] I. Streeter, N. Fietkau, J. del Campo, R. Mas, F. X. Mũnoz, and R. G. Compton. "Voltammetry at regular microband electrode arrays: Theory and experiment". In: *The Journal of Physical Chemistry C* 111.32 (2007), pp. 12058–12066.

[310] B. Zhang, Y. Zhang, and H. S. White. "The nanopore electrode". In: *Analytical chemistry* 76.21 (2004), pp. 6229–6238.

[311] B. Zhang, Y. Zhang, and H. S. White. "Steady-state voltammetric response of the nanopore electrode". In: *Analytical chemistry* 78.2 (2006), pp. 477–483.

[312] S. Lee, Y. Zhang, H. S. White, C. C. Harrell, and C. R. Martin. "Electrophoretic capture and detection of nanoparticles at the opening of a membrane pore using scanning electrochemical microscopy". In: *Analytical chemistry* 76.20 (2004), pp. 6108–6115.

[313] E. A. Heins, Z. S. Siwy, L. A. Baker, and C. R. Martin. "Detecting single porphyrin molecules in a conically shaped synthetic nanopore". In: *Nano Letters* 5.9 (2005), pp. 1824–1829.

[314] Y. Zhang, B. Zhang, and H. S. White. "Electrochemistry of nanopore electrodes in low ionic strength solutions". In: *The Journal of Physical Chemistry B* 110.4 (2006), pp. 1768–1774.

[315] A. J. Bard, L. R. Faulkner, et al. "Fundamentals and applications". In: *Electrochemical Methods* 2.482 (2001), p. 168.

[316] J. A. Alden, R. G. Compton, and R. A. Dryfe. "Theory of ECE processes at hemicylinder and band microelectrodes". In: *Journal of Electroanalytical Chemistry* 397.1-2 (1995), pp. 11–17.

[317] R Greef, R Peat, L. Peter, D Pletcher, and J Robinson. "Southampton Electrochemistry Group". In: *Instrumental Methods in Electrochemistry*. Ellis Horwood Chichester, 1985.

[318] K. B. Oldham. "Theory of microelectrode voltammetry with little electrolyte". In: *Journal of electroanalytical chemistry and interfacial electrochemistry* 250.1 (1988), pp. 1–21.

[319] A. M. Bond, M Fleischmann, and J Robinson. "Electrochemistry in organic solvents without supporting electrolyte using platinum microelectrodes". In: *Journal of Electroanalytical Chemistry and Interfacial Electrochemistry* 168.1-2 (1984), pp. 299–312.

[320] A. M. Bond, M Fleischmann, and J Robinson. "Voltammetric measurements using microelectrodes in highly dilute solutions: theoretical considerations". In: *Journal of electroanalytical chemistry and interfacial electrochemistry* 172.1-2 (1984), pp. 11–25.

[321] C Amatore, M. R. Deakin, and R. M. Wightman. "Electrochemical kinetics at microelectrodes: Part IV. Electrochemistry in media of low ionic strength". In: *Journal of electroanalytical chemistry and interfacial electrochemistry* 225.1-2 (1987), pp. 49–63.

[322] J. O. Howell and R. M. Wightman. "Ultrafast voltammetry and voltammetry in highly resistive solutions with microvoltammetric electrodes". In: *Analytical Chemistry* 56.3 (1984), pp. 524–529.

[323] J. E. Baur, E. W. Kristensen, L. J. May, D. J. Wiedemann, and R. M. Wightman. "Fast-scan voltammetry of biogenic amines". In: *Analytical chemistry* 60.13 (1988), pp. 1268–1272.

[324] A. J. Bard, F. R. F. Fan, J. Kwak, and O. Lev. "Scanning electrochemical microscopy. Introduction and principles". In: *Analytical Chemistry* 61.2 (1989), pp. 132–138.

[325] N. Xiao and B. J. Venton. "Rapid, sensitive detection of neurotransmitters at microelectrodes modified with self-assembled SWCNT forests". In: *Analytical chemistry* 84.18 (2012), pp. 7816–7822.

[326] S. Y. Ly, H. J. Heo, and M. J. Kim. "Real time analysis of neurotransmitters in the brain using a micro-electrode system". In: *Current neurovascular research* 7.1 (2010), pp. 32–38.

[327] D. K. Wong and L. Y. Xu. "Voltammetric studies of carbon disk electrodes with submicrometer-sized structural diameters". In: *Analytical Chemistry* 67.22 (1995), pp. 4086–4090.

[328] Y. H. Lee and G. T. Tsao. "Dissolved oxygen electrodes". In: (1979). Ed. by T. K. Ghose, N. Blakebrough, and A. Fiechter, pp. 35–86.

[329] H Baumgärtl and D. Lübbers. "Microcoaxial needle sensor for polarographic measurement of local O 2 pressure in the cellular range of living tissue. Its construction and properties". In: *Polarographic oxygen sensors*. Springer, 1983, pp. 37–65.

[330] B. Y. Ahn, D. J. Lorang, E. B. Duoss, and J. A. Lewis. "Direct-write assembly of microperiodic planar and spanning ITO microelectrodes". In: *Chemical communications* 46.38 (2010), pp. 7118–7120.

[331] L. Danis, D. Polcari, A. Kwan, S. M. Gateman, and J. Mauzeroll. "Fabrication of carbon, gold, platinum, silver, and mercury ultramicroelectrodes with controlled geometry". In: *Analytical Chemistry* 87.5 (2015), pp. 2565–2569. ISSN: 15206882.

[332] Z. Chen, W. Li, R. Li, Y. Zhang, G. Xu, and H. Cheng. "Fabrication of highly transparent and conductive indium–tin oxide thin films with a high figure of merit via solution processing". In: *Langmuir* 29.45 (2013), pp. 13836–13842.

[333] R. Wang, C. Beling, S Fung, A. Djurišić, C. Ling, and S Li. "Influence of gaseous annealing environment on the properties of indium-tin-oxide thin films". In: *Journal of applied physics* 97.3 (2005), p. 033504.

[334] P. Wilde, T. Quast, H. B. Aiyappa, Y.-T. Chen, A. Botz, T. Tarnev, M. Marquitan, S. Feldhege, A. Lindner, C. Andronescu, et al. "Towards Reproducible Fabrication of Nanometre-Sized Carbon Electrodes: Optimisation of Automated Nanoelectrode Fabrication by Means of Transmission Electron Microscopy". In: *ChemElectroChem* 5.20 (2018), pp. 3083–3088.

[335] M. Armstrong-James and J. Millar. "Carbon fibre microelectrodes". In: *Journal of neuroscience methods* 1.3 (1979), pp. 279–287.

[336] P. Actis, S. Tokar, J. Clausmeyer, B. Babakinejad, S. Mikhaleva, R. Cornut, Y. Takahashi, A. Lopez Cordoba, P. Novak, A. I. Shevchuck, et al. "Electrochemical nanoprobes for single-cell analysis". In: *ACS nano* 8.1 (2014), pp. 875–884.

[337] R. M. Wightman, E. Strope, P. M. Plotsky, and R. N. Adams. "Monitoring of transmitter metabolites by voltammetry in cerebrospinal fluid following neural pathway stimulation". In: *Nature* 262.5564 (1976), pp. 145–146.

[338] H.-Y. Cheng, J Schenk, R Huff, and R. Adams. "In vivo electrochemistry: behavior of micro electrodes in brain tissue". In: *Journal of Electroanalytical Chemistry and Interfacial Electrochemistry* 100.1-2 (1979), pp. 23–31.

[339] G. Zhao, D. M. Giolando, and J. R. Kirchhoff. "Chemical vapor deposition fabrication and characterization of silica-coated carbon fiber ultramicroelectrodes". In: *Analytical chemistry* 67.15 (1995), pp. 2592–2598.

[340] Y. Fang and J. Leddy. "Cyclic voltammetric responses for in-laid microdisks with shields of thickness comparable to the electrode radius: a simulation of reversible electrode kinetics". In: *Analytical Chemistry* 67.7 (1995), pp. 1259–1270.

[341] G. Herzog and V. Beni. "Stripping voltammetry at micro-interface arrays: A review". In: *Analytica Chimica Acta* 769 (2013), pp. 10–21. ISSN: 00032670.

[342] A. Adenier, M. M. Chehimi, I. Gallardo, J. Pinson, and N. Vilà. "Electrochemical Oxidation of Aliphatic Amines and Their Attachment to Carbon and Metal Surfaces". In: *Langmuir* 20.19 (2004), pp. 8243–8253. ISSN: 0743-7463.

[343] E Laviron. "The use of linear potential sweep voltammetry and of ac voltammetry for the study of the surface electrochemical reaction of strongly adsorbed systems and of redox modified electrodes". In: *Journal of Electroanalytical Chemistry and Interfacial Electrochemistry* 100.1-2 (1979), pp. 263–270.